Technische Universität München
Fachgebiet für Supramolekulare Chemie

Designing and Controlling Dissipative Self-Assembly of Nanoparticles

Raphael Kurt Grötsch

Vollständiger Abdruck der von der Fakultät für Chemie der Technischen Universität München zur Erlangung des akademischen Grades eines

Doktors der Naturwissenschaften (Dr. rer. nat.)

genehmigten Dissertation.

Vorsitzender:		Prof. Dr. Matthias J. Feige
Prüfer der Dissertation:	1.	Prof. Dr. Job Boekhoven
	2.	Prof. Dr. Dr. h.c. Bernhard Rieger
	3.	Prof. Dr. Jonathan G. C. Veinot

Die Dissertation wurde am 19. August 2019 bei der Technischen Universität München eingereicht und durch die Fakultät für Chemie am 08. Oktober 2019 angenommen.

„Albert Einstein hat einmal gesagt, dass sich in der Naturgesetzlichkeit “eine so überlegene Vernunft offenbart, dass alles Sinnvolle menschlichen Denkens und Anordnens dagegen ein gänzlich nichtiger Abglanz ist”. Wir erkennen, wie im Allergrößten, in der Welt der Gestirne sich eine machtvolle Vernunft offenbart, die das All zusammenhält. Immer mehr lernen wir aber auch, in das Allerkleinste, in die Zelle, in die Ureinheiten des Lebendigen hineinzuschauen; auch hier entdecken wir eine Vernünftigkeit, die uns staunen läßt, so dass wir mit dem heiligen Bonaventura sagen müssen: Wer hier nicht sieht, ist blind. Wer hier nicht hört, ist taub, und wer hier nicht anfängt anzubeten und den Schöpfergeist zu lobpreisen, der ist stumm.”

Joseph Ratzinger
Im Anfang schuf Gott. Fastenpredigt; Donauwörth 1986

"Albert Einstein once said that in the laws of nature, "such superior reason is revealed against which all rationality of human thinking and ordering is only a pale reflection." We recognize how, in the utmost, in the world of the stars, a great reason is revealed that holds the universe together. More and more we also learn to look into the very smallest, into the cell, into the primal unit of the living; here, too, we discover reasonableness that amazes us, so that we have to say with Saint Bonaventure: He who does not see here is blind. Whoever does not hear is deaf, and whoever does not begin to worship and praise the creative spirit is dumb."

Joseph Ratzinger
Im Anfang schuf Gott. Fastenpredigt; Donauwörth 1986

Abstract

The aim of the thesis is to design and study chemical reaction cycles that can drive the dissipative self-assembly of nanoparticles. The thesis starts with an introduction to the field of supramolecular chemistry, followed by an explanation of important non-covalent interactions. After the description of a molecular machine, I elucidate the energy landscape of self-assembly in the next chapter. I will discuss in detail three different types of self-assembly, in-equilibrium self-assembly, non-equilibrium self-assembly, and dissipative self-assembly.

The fuel-driven dissipative self-assembly, which this thesis aims to achieve is clarified with an example from biology, *i.e.*, the microtubule network. This biological system shows the power of supramolecular chemistry and especially dissipative self-assembly to yield materials with unique properties. The final section of the introduction gives examples of man-made fuel-driven assemblies, specifically those that use nanoparticles as building blocks to form supramolecular materials.

In the first experimental chapter, *i.e.*, Chapter 4, I describe the design of a chemical reaction cycle that can drive the dissipative assembly of gold and iron oxide nanoparticles. With this system, we found surprising new behavior that could be rationalized once we understood the boundary conditions of the energy landscape. Three different assembly modes upon fuel addition are examined and described in detail from the macroscopic to the molecular level.

In Chapter 5, I describe the use of the newly developed chemical reaction cycle to drive the self-assembly of silicon nanoparticles. The focus of this work is the spatio-temporal control of the material and its properties, which can yield a potential application as a drug delivery platform. Another application of the silicon nanocrystals is described in Chapter 6. Here, the intrinsic photoluminescent nanoparticles detect aromatic compounds. After a concluding chapter, a list of publications and a reprint of a book chapter on supramolecular biomaterials is given, which completes this thesis.

Zusammenfassung

Das Ziel der Arbeit ist es, chemische Reaktionszyklen zu entwerfen und zu untersuchen, die die dissipative Selbstassemblierung von Nanopartikeln anstoßen können. Die Arbeit beginnt mit einer Einführung in das Gebiet der supramolekularen Chemie, gefolgt von einer Erklärung wichtiger nicht-kovalenter Wechselwirkungen. Nach der Beschreibung einer molekularen Maschine erkläre ich im nächsten Kapitel die Energielandschaft der Selbstassemblierung. Ich werde im Detail auf drei verschiedene Arten der Selbstassemblierung, Gleichgewichts-, nicht Gleichgewichts- und dissipative Selbstassemblierung, eingehen.

Die kraftstoffgetriebene dissipative Selbstassemblierung, die diese Arbeit erreichen soll, wird mit einem Beispiel aus der Biologie, d.h. dem Mikrotubuli-Netzwerk, verdeutlicht. Dieses biologische System zeigt die Stärke der supramolekularen Chemie und insbesondere der dissipativen Selbstassemblierung, um Materialien mit einzigartigen Eigenschaften zu erhalten. Der letzte Abschnitt der Einführung enthält Beispiele für künstliche treibstoff-getriebene Assemblierungen, insbesondere solche, die Nanopartikel als Bausteine für supramolekulare Materialien verwenden.

Im ersten Kapitel nach der Einleitung, d.h. Kapitel 4 beschreibe ich das Design eines chemischen Reaktionszyklus, der die Selbstassemblierung von Gold- und Eisenoxid-Nanopartikeln antriebt. Mit diesem System fanden wir überraschend neues Verhalten, das Verstanden wurde, sobald wir die Randbedingungen der Energielandschaft kannten. Drei verschiedene Arten von kraftstoffgetriebener Assemblierung werden von der makroskopischen bis hin zur molekularen Ebene im Detail untersucht.

In Kapitel 5 beschreibe ich die Verwendung des neu entwickelten chemischen Reaktionszyklus, um die Selbstassemblierung von Silizium-Nanopartikeln voranzutreiben. Der Schwerpunkt dieser Arbeit liegt auf der räumlichen zeitlichen Kontrolle des Materials und seiner Eigenschaften, die eine mögliche Anwendung als Wirkstofffreisetzungsplattform ergeben kann. Eine weitere Anwendung der Silizium-Nanokristalle ist in Kapitel 6 beschrieben. Hier detektieren die intrinsisch photolumineszierenden Nanopartikel aromatische Verbindungen. Nach einem abschließenden Kapitel wird eine Liste der Veröffentlichungen und ein Nachdruck eines Buchkapitels über supramolekulare Biomaterialien vorgelegt, das diese Arbeit abrundet.

Supramolecular Chemistry

Abstract.

In this chapter, I will give an overview of supramolecular chemistry how the field developed as well as its fundamental principles. In the next sub-section, I will introduce non-covalent interactions as they play a crucial role in supramolecular chemistry. I will end the section with an example of a molecular machine driven by electric impulses. This machine is an example of a complex system that serves a specific function, unidirectional movement.

1.1. The Beginning of Supramolecular Chemistry

For centuries, chemists synthesized increasingly complex compounds. Their abilities to do so developed drastically. In 1825, it was remarkable that F. Wöhler synthesized urea from non-living materials.[1] (Figure 1a). In 1994, i.e., almost 170 years later, E. Suh and Y. Kishi reported the total synthesis of Palytoxin.[2] This toxin is made of 129 carbon atoms with a total number of 409 atoms (Figure 1b). This total synthesis is one of the most complex syntheses that does not rely on the use of enzymatic conversions. Nevertheless, the strategy of creating covalent bonds to build bigger and more complex molecules reaches its limits.[3] Biology uses, besides the synthesis of molecules, another strategy to create complex systems. Instead of forming covalent bonds, smaller molecules are assembled into larger structures using non-covalent interactions. This non-covalent approach is an elegant method to position a large number of atoms in repeating patterns with similar precision as the covalent approach but using only relatively small molecules. It also limits the complex synthetic routes towards large molecules to a minimum.

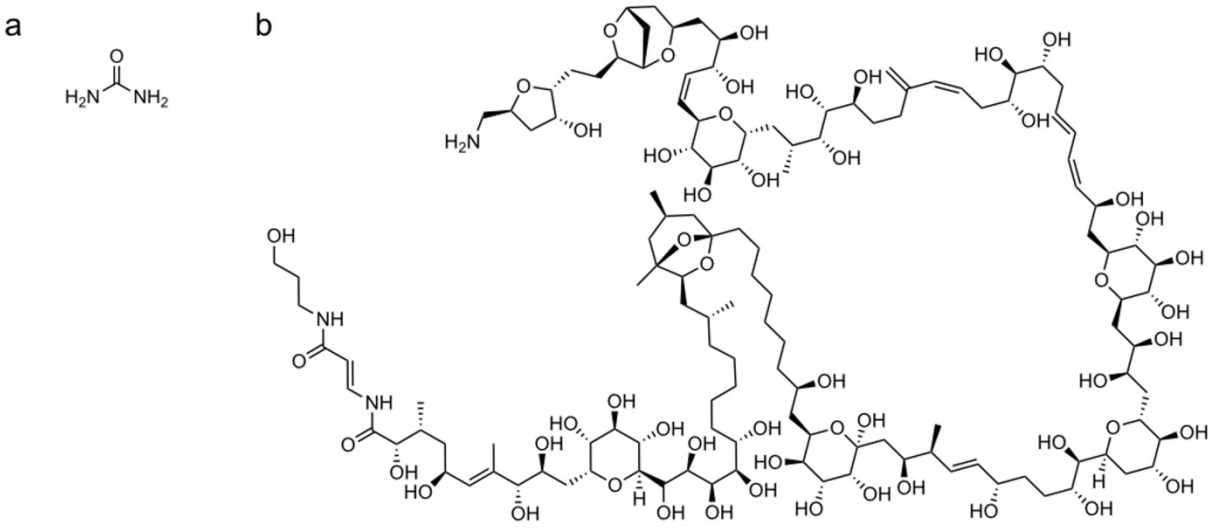

Figure 1: *Structural formulas: a) Urea b) Palytoxin.*

Supramolecular chemistry is now recognized as a key strategy of the chemistry field that J.-M. Lehn described in his Nobel Prize lecture in 1987 as: “the chemistry of the intermolecular bond”.[4] This short definition in combination with granting the Nobel Prize to D. J. Cram, C. Pedersen, and J.-M. Lehn helped to form a new direction in the field of chemistry. Before the recognition of the field with a Nobel Prize, researchers studied

supramolecular systems based on host-guest chemistry and others. For example, Powell described clathrates that include small molecules in their own lattice structures in 1948.[5] The nickel cyanide complex in Figure 2 bares benzene molecules between two layers of complexes thus forming a clathrate published by Powell in 1951.[6] Pedersen worked in 1967 on the synthesis of macrocycles, so-called crown ethers, and studied how these crown ethers could complex small cations (Figure 2b).[7] Remarkably, the hosted cations, like Na^+ and K^+, could be transferred to organic solvents in which these ions are otherwise insoluble.[8] Likewise, cryptands, due to the cage-like structure, have a higher affinity and selectivity for metal ions (Figure 2c).[9]

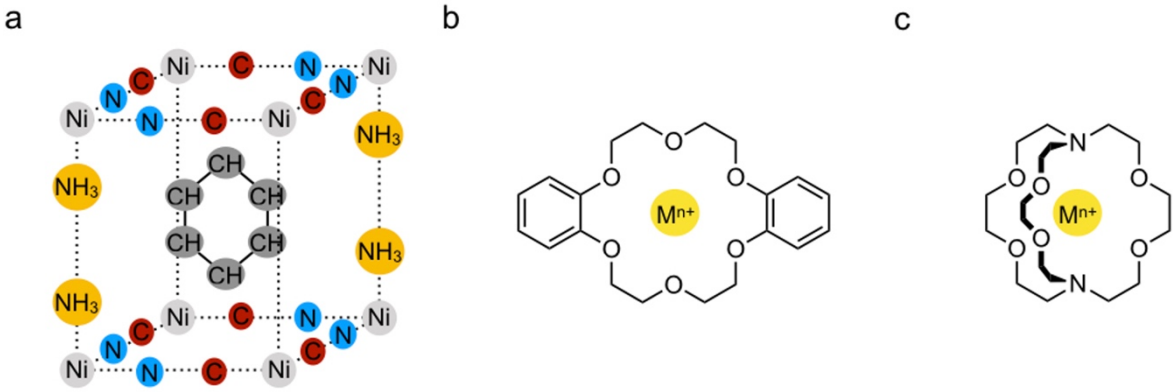

Figure 2: *Schematics of early supramolecular compounds: a) Clathrate* $(Ni(CN)_2NH_3 \cdot C_6H_6)$ *b) Dibenzo-18-crown-6 with a complexed metal cation c) Complex of [2.2.2]Cryptand with a metal cation.*

As the field developed, chemists focused on molecules interacting with one another to form larger systems. “Supramolecular chemistry has grown in importance because it goes beyond the molecule – the focus of classical chemistry.”[10] This phrase from G. Desiraju paraphrased the earlier definition from J.-M. Lehn and gave at the same time a reason in which way the field is different compared to classical chemistry: organic chemistry focusses on the synthesis of the molecule, whereas supramolecular chemistry uses the molecule as a building block to form larger self-assembled molecular structures.

1.2. Non-Covalent Interactions

Supramolecular chemistry, as well as molecular self-assembly which I discuss in the next chapter, makes use of non-covalent interactions to stick molecules together in larger complexes. Also, the early examples of supramolecular compounds in Figure 2 rely on those interactions. In the following paragraph, I give an overview of the non-covalent interactions relevant to this thesis, which can be both attractive or repulsive.[11] It is important to understand the different interactions, as the knowledge provides a deeper understanding of existing materials and can lead the way to design properties in new supramolecular materials.

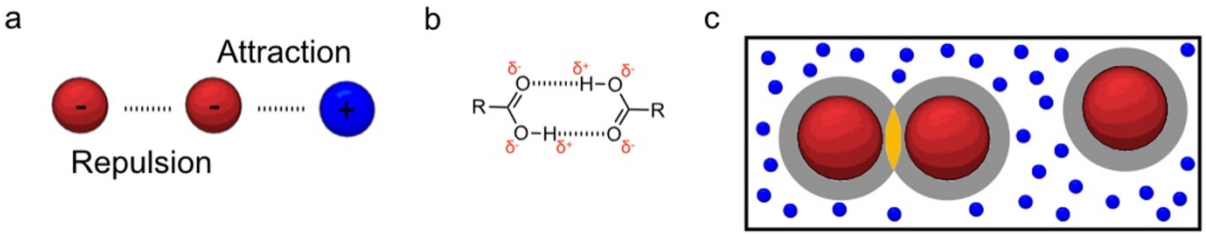

Figure 3: *Concepts of non-covalent interactions: a) Ionic interactions; The red dots are negatively charged, and the blue dot is positively charged. Opposite/alike charges attracted/repel each other, respectively. b) Two hydrogen bonds between acid groups. Partial charges are noted with a δ. c) Big particles (red) in surrounding small solvent molecules (blue). The grey color shows exclusive areas of the big particles. The orange area is space shared between two big neighboring particles.*

Ionic interactions are widespread in ionic crystals, but exists between all charged entities and can be attractive and repulsive.[12] The electrostatic interaction occurs if charged molecules or atoms are present. Two charges of opposite nature will attract one another with bonding energies comparable to covalent bonds. The precursor nanoparticles I use in Chapters 4 to 6 form stable colloidal solutions because of their negatively charged surface. In the experiments, I regulate the electrostatic repulsion between negatively charged nanoparticles to govern the self-assembly.

Another type of electrostatic interaction is the dipole-dipole interaction. A specific example of the dipole-dipole interaction is the hydrogen bond.[13] Hydrogen bonds form when a hydrogen bond donor and a hydrogen bond acceptor with negative (partial) charges share a hydrogen atom between each other. As such, this is similar to other

dipole interactions but with relatively high dissociation energy. It plays a crucial role in living and non-living materials. For example, the hydrogen bond is partly responsible for the hybridization of hybridized DNA or the folding of proteins.[14]

Metal ligand interactions form the lattice structure in Figure 2a. It is an attractive interaction.[12] A central atom, usually a metal, is bound to a couple of surrounding molecules. This idea is well known for complexes and form materials. An ordered 2- or 3-D material builds up via those directed interactions.

A large colloidal particle that is surrounded by solvent molecules has an attractive force towards a neighboring colloidal particle.[15] The solvent molecules between the two particles tend to leave the space in between, and the particles are drawn to each other. The big particles share an area in between depicted in orange in Figure 3c. This effect increases the entropy of the surrounding solvent molecules and is considered to be the driving mechanism. So, colloidal particles start to coagulate in solution, which is referred to as the depletion force. This is an effect that I utilize to cluster nanoparticles in Chapters 4 to 6.

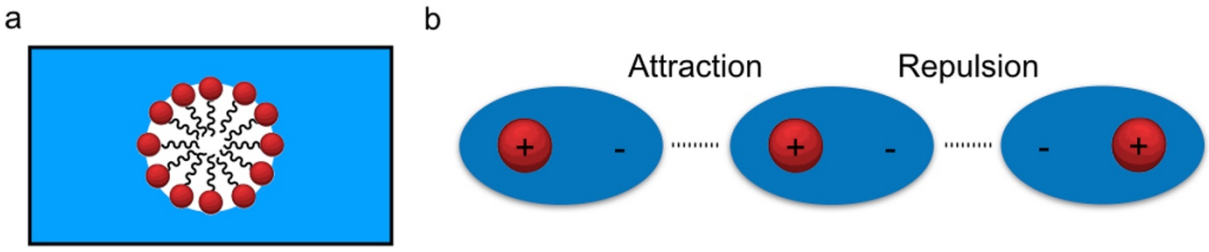

Figure 4: *a) Micelle formation of amphiphiles to reduce surface interactions between hydrophobic parts in the molecule and surrounding water molecules (blue). b) Van der Waals interactions: positively charged nucleus (red) and aspherical negatively charged electron density (blue). Opposite/alike charges attracted/repel each other, respectively. The aspherical shape can be induced or permanent.*

The hydrophobic effect describes the phenomena that a hydrophobic substance is aggregating to bigger structures in water. For example, the amphiphiles in Figure 4a. Logically, it is an attractive effect for hydrophobic molecules. The effect has its origin from the disturbed order of the former pure water solution by the hydrophobic molecules.[13]

Another class of interactions are the van der Waals forces. Those interactions exist between all molecules and particles.[16] Instead of charged entities a dipole (so indeed van der Waals is a form of an electrostatic interaction), permanent or transient, is sufficient. The permanent dipole-dipole interaction is called Keesom interaction, and the range is relatively short. It is also attractive or repulsive and is observed in colloidal materials. The second type is the London dispersion force. The random fluctuations in electron density induce transient dipoles. This interaction is ubiquitous, as every molecule has electrons (Figure 4b).

A lot of the interactions I described here are present at the same time. By tuning the strength of the individual interaction, the attraction or repulsion can be more powerful and lead to assembly or disassembly. For example, a nanoparticle is well soluble in aqueous media if it is sufficiently charged. Reducing the amounts of charges reduces the repulsion and if other attractive forces like the hydrophobic effect or the hydrogen bonding become in total stronger then the repulsive interactions, the particles start to agglomerate. This is demonstrated in detail in Chapters 4 to 6. In the next section, I will show a unique example of a man-made molecular machine that demonstrates the possibilities of the well-balanced interactions as well as the possibilities supramolecular systems offer.

1.3. Molecular Machines

Relatively recently, the Nobel Prize in the field of supramolecular chemistry was awarded to three chemists that used supramolecular chemistry to synthesize molecular machines. Jean-Pierre Sauvage, Sir J. Fraser Stoddart, and Bernard L. Feringa received the prize for the “design and synthesis of molecular machines”.[17] In Figure 3, one example of such a molecular machine developed by B. Feringa is depicted: a nano-car that can “drive” on a Cu surface upon electric stimulation.[18] The design is based on four molecular motors that the group of B. Feringa initially described in a landmark paper.[19] These further developed motors contain three elements: a stator, a rotor, and an axle. Upon stimulation by light or by a redox potential rotor rotates relative to the stator around its axle. In molecular terms, the double bond axle isomerizes forcing the rotor aromatic group to rotate. After years of research, the group found the right molecular design to make unidirectional rotations possible.

Noteworthies are the stereogenic centers and a specific crowding around the axel.[20] Nevertheless, a unidirectional rotating motor is no machine. Thus, the team attached two clockwise rotating motors and two counter-clockwise rotating motors to a molecular scaffold (bodywork) such that a molecular car was built.

The molecular car was deposited on a Cu (1,1,1) surface and analyzed by scanning tunneling microscopy (STM). The STM-tip also served as a source of current for electronic stimulation. The car could move several nanometers upon electronic impulses. In other words, the external electrical energy supplied by the STM tip was absorbed by the car and converted into motion. Also, designs based on rotaxanes, that resemble a muscle, were developed by F. Stoddart.[21] The more and more complex synthesis of catenanes by J.-P. Sauvage inspired the fabrication of the machines.[22]

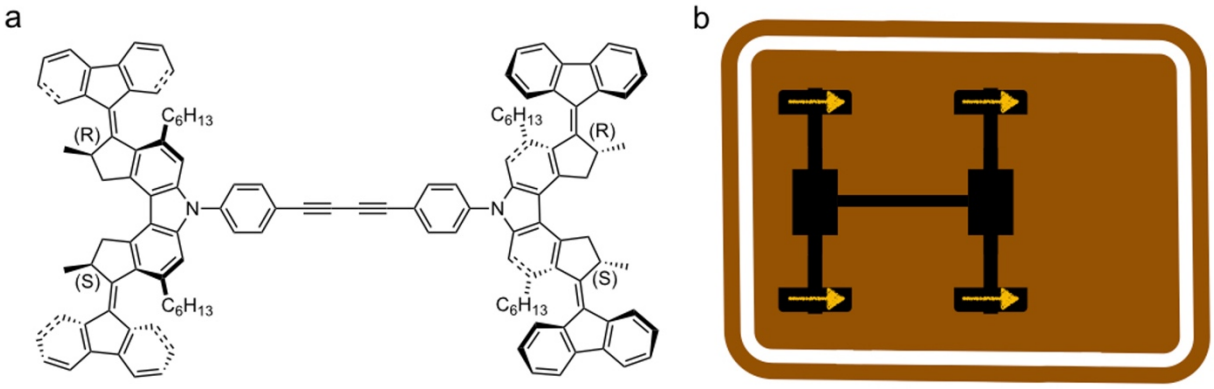

Figure 3: *Nano car: a) Meso-(R,S-R,S) isomer b) Sketch of the four-wheeled nano car on a copper surface. Arrows indicate movement induced by rotation of the "wheels".*

From the development of the first man-made host-guest complex in the early fifties to nano cars and synthetic shuttles has been a magnificent leap for the field of supramolecular chemistry. The non-covalent interactions used to construct molecular machines have been mainly inspired by nature. Biology uses supramolecular machinery to create molecular machineries like the actin motors and myosin molecular muscles. However, biology also uses supramolecular chemistry to make structural components like cells and tissue. Those structural components are the so-called roads for a lot of biological machines. Via those roads, it is possible to transport chemicals very specifically to the area where it is needed. In the strategy of creating those structural components, vast amounts of molecules assemble driven by non-covalent interactions to form assemblies that have different material properties compared to the

non-assembled building blocks. Because of the use of dynamic non-covalent interactions, these materials possess several exciting properties. Biological materials can be self-healing, *e.g.,* our skin repairs itself damage. These materials can be adaptive, which means they can rapidly adjust after a small change in the environment, like a mechanical stimulus to a bone induces a change in the organization of fibers and in the deposition of new bone material to reinforce the weaker parts. Another feature of these materials is the regulation over space and over time (spatiotemporal control), *e.g.,* they can be controlled where to move and when to move. While all these exciting properties are common in biology, the use of self-assembly in synthetic materials (so-called supramolecular materials) remains unexplored and is the topic of the next chapter.

Molecular Self-Assembly

Abstract.

Molecular self-assembly refers to the process in which molecules or nanoparticles spontaneously self-assemble into a larger structure. The non-covalent interactions that drive the formation of supramolecular complexes, like described in the previous chapter, are the reason for the spontaneous process. In the following sections, I will explain the energy landscapes that are associated with self-assembly processes. There, I classify three types of self-assembly of which one, dissipative self-assembly, is the focus of this thesis. Finally, I describe the use of nanoparticles as building blocks for self-assembly.

Parts of this chapter are based on the ideas published or submitted in the manuscripts:

1) R. K. Grötsch, J. Boekhoven, *11 - Unique properties of supramolecular biomaterials through nonequilibrium self-assembly.* In *Self-assembling Biomaterials*, R. M. P. d. Silva, H. S. Azevedo, Eds. Woodhead Publishing: **2018**; pp 235-250.

2) B. Rieß[+], R. K. Grötsch[+], *The design of dissipative molecular assemblies driven by reaction cycles*. **2019**, Submitted.

2.1. Energy Landscape of the Self-Assembly Processes

In this section, I compare several types of self-assembly based on their behavior in the free energy landscape. Upon self-assembly, the building blocks in the assembly can reside in different states of the energy landscape.[23] While the design of the building block is an important parameter for the resulting assembly and its material properties, the position of the building blocks within the energy landscape can also affect the material. Thus, to be able to use molecular self-assembly to design desired materials, one should not only take into account the process of designing building blocks for self-assembly but also consider the energy landscapes in which the building blocks will reside later on. I will focus on the three different energy states depicted in Figure 4: In equilibrium self-assembly, non-equilibrium self-assembly, and dissipative non-equilibrium self-assembly.[24,25] The following paragraphs explain each in detail.

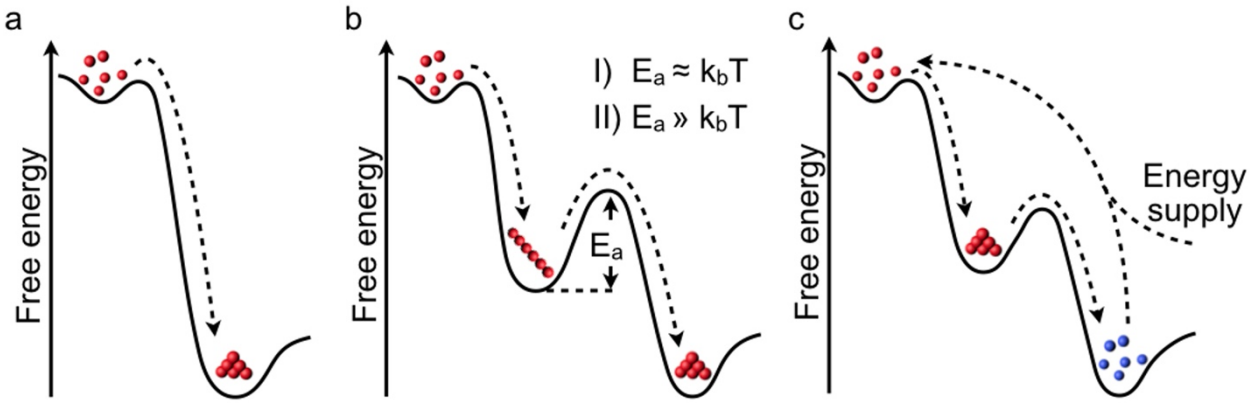

Figure 4: *Schematic free energy landscape of self-assembly: a) In equilibrium self-assembly b) Non-equilibrium self-assembly; I): Metastable assembly; II): Kinetically trapped assembly c) Dissipative non-equilibrium self-assembly.*

2.1.1. In-Equilibrium Self-Assembly

In-equilibrium self-assembly is the most explored method to form supramolecular materials. Here, the global minimum of the building block in its energy landscape is represented by the self-assembled state, while unassembled building blocks represent a state associated with somewhat higher free energy. Consequently, self-assembly is associated with a gain in free energy and thus favored from a thermodynamic point of view (Fig. 1a). Depending on the gain in the free energy upon, building blocks can be

exchanged dynamically with those that are in solution, but this happens at equal rates (hence the term in-equilibrium self-assembly). The dynamic exchange of building blocks is an essential aspect of equilibrium self-assembly, as it offers a mechanism by which the assembly can dynamically try different types of assemblies until it “finds” the global minimum.[26] The dynamics of such an exchange can be designed in the building blocks by the strength of the non-covalent interactions. For example, when the non-covalent interactions are relatively weak, like in the case of spherical micelles,[27] dynamic exchange can take place. Indeed, the building blocks within a micelle have a residence time of merely tens of microseconds. In contrast, the lipids in phospholipids bilayers are characterized by much stronger non-covalent interaction and exchange at rates several orders of magnitude slower.

It is important to note that the global minimum in an energy landscape is strongly dependent on the thermodynamic environment following the second law of thermodynamics. In other words, if one changes the environment of the building blocks in the assembly, for example by addition of a co-solvent, a change in pH or addition of salt, the global minimum may be different. For example, in the new energy landscape, the global minimum may be represented by a disassembled state, and thus, the change in environment can trigger disassembly. Besides, the system needs enough time to transform from the starting point to the new equilibrium.

2.1.2. Non-Equilibrium Self-Assembly

In non-equilibrium self-assembly, the self-assembled state is not represented by the lowest state in the energy landscape. The building blocks in the assembly, thus aim to reach the global minimum. That means new molecular building blocks may be trying different modes of the assembly to find the global minimum. In this case, there are two scenarios depicted in Figure 4b. The energy (E_a) that is needed to overcome to transition to another mode is in the same magnitude as the amount of thermal energy available in the system (k_bT, where k_b is the Boltzmann constant and T the temperature; Fig. 1b I). In this case, the exchange of building blocks is possible, and the material is metastable, *i.e.*, it slowly relaxes to the structure state at the global minimum. In contrast, if E_a is much higher than k_bT, there is no exchange of building blocks. That means that, even though there is a thermodynamic driving force to change the assembly, the available thermal energy does not allow it. Thus, there is no

exchange of building blocks on experimental time-scales, and thus, in theory, this assembly is kinetically trapped in a state it can only escape by changing the energy landscape, e.g., changing the pH, adding a co-solvent or changing the amount of thermal energy (Figure 4b II). Raising the thermal energy transforms the system to a metastable or even an in-equilibrium self-assembly state, depending on how much thermal energy is added and how deep the well of the local minimum was.

2.1.3. Dissipative Non-Equilibrium Self-Assembly

In the assembly processes described so far, the building block that assembles was already present in the system. In the dissipative self-assembly, the process starts one step further back (Figure 4c). Here, the starting material is an inactive precursor that resides in the thermodynamic minimum. Only after a chemical reaction with a source of energy (*e.g.,* a photon or a chemical fuel), the precursor converts into an active building block that can self-assemble. However, the activated building block is intrinsically unstable and spontaneously reacts back to the precursor which induces disassembly. Besides the activation, the fuel also yields waste, that can be a waste molecule or heat. In other words, to sustain the self-assembled state, the system continually absorbs and dissipate energy. Otherwise, the building blocks in the self-assembled state spontaneously deactivate and disassemble. To fulfill these requirements, the process of self-assembly is coupled to a chemical reaction cycle, which I discuss in detail in the next section.

2.2. Dissipative Self-Assembly of Microtubules

While examples of synthetic dissipative assemblies are somewhat limited, examples from biology are ubiquitous. A particularly illustrative example of this type of non-equilibrium self-assembly is the microtubules which are part of the cytoskeleton in cells.[28] The cytoskeleton provides the cell's internal scaffolding and is thus responsible for the shape of cells. Because the scaffold can exert forces on its surrounding matrix, it is also responsible for the migration of cells. All of these functions are possible because of the dynamic nature of the microtubule network. That means, to exert forces on a surrounding matrix, new microtubules need to be assembled on specific sites, while others need to be disassembled. Biology regulates that dynamic behavior by the

constant activation and deactivation of the molecular building blocks that form the microtubule network, *i.e.*, by dissipative self-assembly of tubulin into microtubules. Tubulin is a heterodimer comprising one α-tubulin and one β-tubulin. In order to activate tubulin for self-assembly into microtubules, each α- and β-tubulin binds one molecule of guanosine triphosphate (GTP). With two molecules of GTP bound, the tubulin is activated and spontaneously self-assembles into protofilaments, *i.e.*, stacks of the activated tubulin via a supramolecular polymerization mechanism by non-covalent interactions between the dimers (See Figure 5). Eight to 12 of these protofilaments laterally associate, again via non-covalent interactions, to form a hollow tube with an outer diameter of 25 nm.[29] On one end of this tube, capping proteins stabilize the microtubules such that growth occurs in one direction. However, the microtubule is far from stable on the other end. Upon self-assembly, the activated tubulin dimer is autocatalytically hydrolyzed from GTP-bound to guanosine diphosphate (GDP)-bound tubulin. This GDP-bound tubulin is unable to self-assemble, but, as long as the deactivated tubulin is not at the end cap of the microtubule, it is trapped and cannot leave the microtubule. However, as soon as the tubulin at the tip of the microtubule is also hydrolyzed, a large part of the microtubule collapses rapidly.[29] In other words, as long as activation and assembly at the tip of the tubule occur faster than deactivation, the microtubule grows. However, the moment the activation is slower than the deactivation (for example, because of a low GTP concentration), the tubule rapidly collapses.

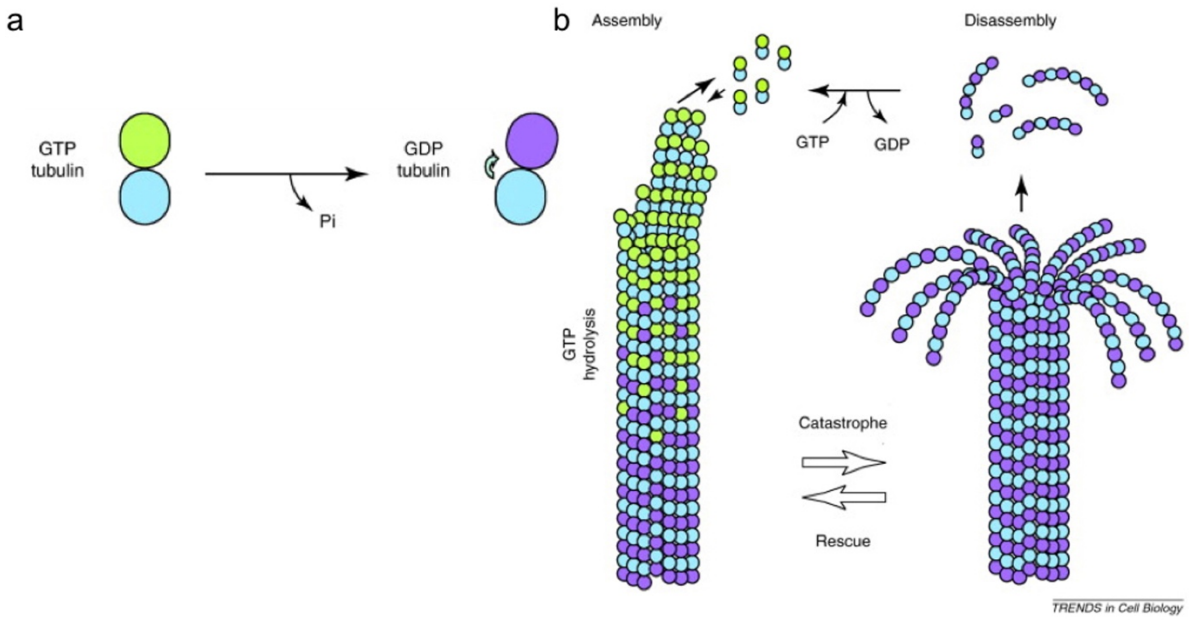

Figure 5: *Microtubule filaments: a) Hydrolysis of one GTP to GDP in the tubulin dimer. The green or purple part of the tubulin represents* β-tubulin with GTP or GDP, respectively. *b) Assembly and disassembly of microtubule filaments. Tubulin dimers with GTP incorporate into a growing filament. Filaments with tubulin dimers with GDP disassemble.*

Taken together, the activation and deactivation of tubulin dimers control the growth and collapse rate of the microtubules. Because activation and deactivation are coupled to a chemical reaction cycle, the entire process of self-assembly is coupled to a chemical reaction cycle. The use of energy-consuming chemical reaction cycles offers the cell kinetic control over the microtubule network. In other words, by tuning the GTP concentration, the microtubule network can be regulated. This means that the rate of assembly and disassembly of the material can be tuned and is not constant but increase or decreases depending on the concentration of chemicals. Such kinetic control leads to new properties that are typically not observed when assemblies are regulated by the laws of thermodynamics. Such behavior includes the ability to grow into a particular direction and to self-heal if the microtubules are damaged. Also, in biology, nothing comes for free. The downside of using chemical reaction cycles to regulate material properties is that, over its entire lifetime, the material requires a constant influx of energy, for microtubules GTP. This mode of self-assembly is referred to as dissipative self-assembly.

The reaction of activation and deactivation regulate the diverse functions fulfilled by the cytoskeleton in a cell. That means that building blocks are rapidly recycled and can be part of different structures with a different function in their lifetime. Being able to use a building block several times for different materials can be useful and efficient in terms of atom-economy. Moreover, the recycling of building blocks that less material has to be transported to an area of interest. The material can self-heal and is by this mode of self-assembly more robust than a system compared to assemblies that reside in equilibrium.[30]

2.3. Synthetic Chemical Reaction Cycles to Drive Dissipative Self-Assembly

Inspired by the exciting properties of microtubules, researchers have developed synthetic analogs of dissipative self-assembly.[23,25,31,32] In this section, I set out the design rules for the chemical reaction cycles that can drive the self-assembly. I will also discuss examples of chemical reaction cycles that have been developed.

For a chemical reaction cycle to drive dissipative self-assembly, it has to comprise at least two chemical reactions, *i.e.*, an activation and deactivation reaction. The activation reaction converts a precursor into a product that can self-assemble. This reaction is irreversible and is driven by the consumption of fuel. In other words, the activation reaction irreversibly converts the precursor into the product via fuel consumption. The fuel is typically a chemical fuel or a photon. In this thesis, I will exclusively focus on the chemically fueled cycles. The deactivation reaction is a spontaneous reaction that reverts the product to the precursor and thereby closed the chemical reaction cycle.

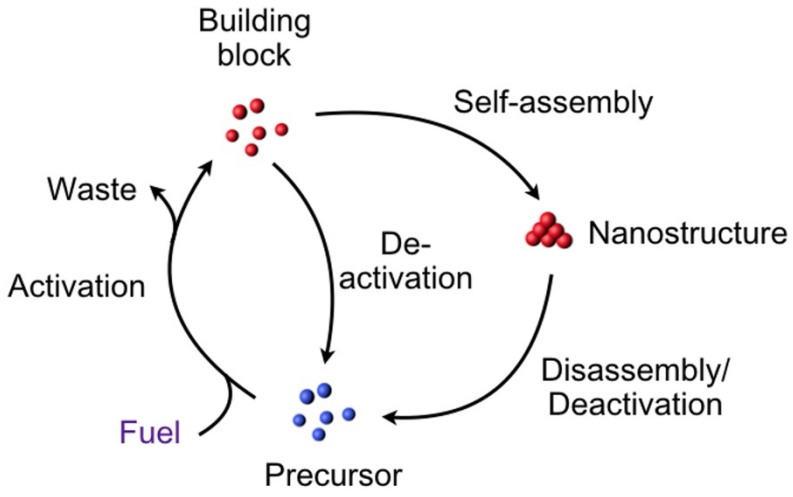

Figure 6: *Schematics of a chemical reaction cycle: the precursor reacts with fuel to the building block. The building block can self-assemble into a nanostructure or spontaneously deactivate to the precursor. The building blocks in the nanostructure disassemble as the precursor spontaneously deactivates.*

In the product state, the attractive non-covalent interactions are sufficiently large to induce self-assembly into a nanostructure. The concentration of the product governs the self-assembly process. Moreover, the kinetics of activation and deactivation regulate the concentration of the product. In other words, the kinetics of the reaction cycle define the emerging assemblies and its associated material properties and not only the molecular design of the building block. This resembles the concept of the previously mentioned example of the microtubules.

In the following, I will discuss several chemical reaction cycles that follow the above design. Van Esch and Eelkema developed the first example of a synthetic reaction cycle for dissipative self-assembly.[33] Three different gelators that are well-soluble in the precursor state are used to test the behavior upon fuel addition. The fuel, dimethyl sulfate, methylates the precursor to form their corresponding methyl esters (Figure 7). The esters are intrinsically unstable in the basic aqueous media and hydrolyze over hours to yield the original precursor. The cycle produces two molecules of waste, in the activation reaction methyl bisulfate, and in the deactivation reaction methanol.

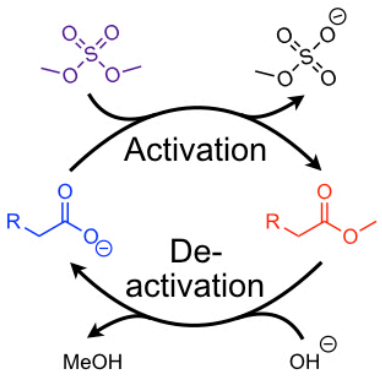

Figure 7: *Chemical reaction cycle of dissipative self-assembly: The carboxylate (precursor) reacts in aqueous media with the dimethyl sulfate to the methyl ester. The ester spontaneously hydrolyzes to the precursor state.*

In the precursor state, the molecules carry negative charges that prevent self-assembly due to electrostatic repulsion. In contrast, upon activation, the negative charge is transiently removed by the methylation of the carboxylates. This activation results in a reduction of the repulsive electrostatic interactions and leads to an attractive force between molecules.

HPLC analyses monitored the different products in the cycle. A kinetic model that described all the relevant reactions in the cycles was written to fit the data. The kinetic model could predict the concentrations of the relevant species in the reaction cycle, as well as the rates. These calculations showed that the amount of ester formed in the chemical reaction cycle strongly depended on the pH and amount of fuel added to the system. So, with fuel concentration, it is possible to gain control over the material properties. Compared to biological systems, this is still a simple system. The reactions are relatively slow, and one of the faster cycles at pH 11 still lasts for several hours. Nevertheless, this work transferred the biological concept to man-made materials.

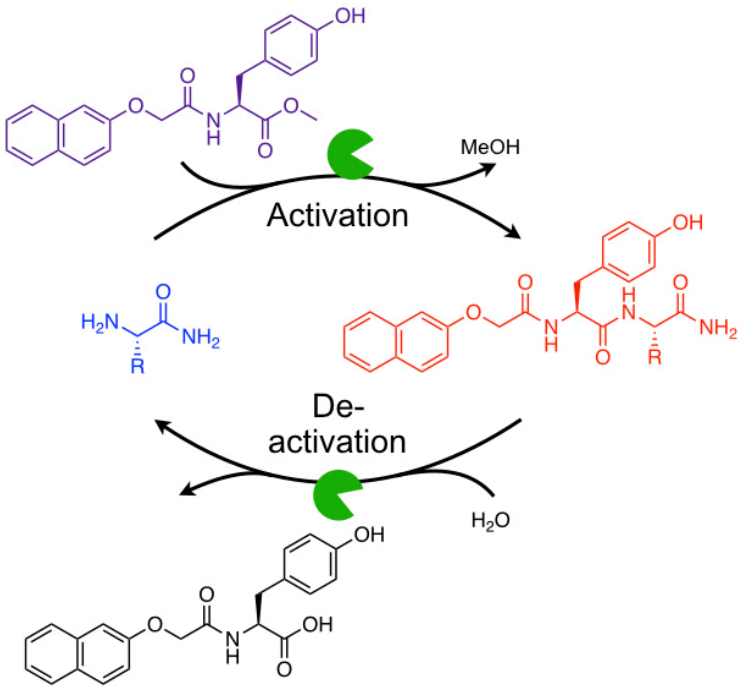

Figure 8: *Chemical reaction cycle of dissipative self-assembly: The coupling of two amino acids (blue represents the precursor and purple the fuel) is catalyzed by the digestive enzyme chymotrypsin (green). This reaction is driven by the hydrolysis of the methyl ester protected amino acid.*

Ulijn and co-workers describe a reaction cycle that forms hydrogels upon the addition of chemical fuel.[34,35] Chymotrypsin, a digestive enzyme, catalyzes the peptide bond formation. A methyl ester protected amino acid is the fuel (Figure 8). The hydrolysis of this methyl ester fuel is driving the cycle, and it produces methanol as waste. The N-terminus of a second amino acid (precursor, blue) reacts with the deprotected amino acid in the fuel, which constitutes the activation reaction. The enzyme also catalyzed the hydrolysis of the peptide bond, the deactivation reaction. Without the enzyme, no reaction is observed. This cycle is an elegant way of using one enzyme that catalyzes the activation as well as the deactivation reaction.

2.4. Nanoparticles As Building Blocks For Dissipative Self-Assembly

Biology uses predominantly small molecules and biopolymers to form molecular assemblies. On the other hand, chemists can further expand the toolbox of the building blocks to non-natural ones. To that end, nanoparticles offer properties that are unique compared to organic building blocks. Nanoparticles are small particles in the range of 1-100 nm. The ratio between the surface to volume is relatively high, and especially the interface between the particle and the surrounding media has a significant influence on the material properties. These particles have shown catalytic activity,[36] photoluminescence,[37] upconversion of photons,[38] superparamagnetism,[39] plasmon resonance[40] and can be electrically conductive.[41] Unknowingly, people used nanoparticles in material science since ancient times. Back then, these materials showed unique colors and glittering effects to beautify surfaces.[42] Predominantly, metal salts were reduced under special conditions to yield those nanoparticles. In modern times the Nobel Prize of 1925 in chemistry was awarded for demonstrating the heterogeneous character of colloidal solutions.[43]

Since the early 20th century, scientists studied the use and synthesis of nanoparticles more thoroughly. These studies have resulted in synthetic pathways and design rules for particles with shapes ranging from spherical, cylindrical to cubical, but also star-like.[44] Moreover, a range of synthetic methodologies allowed for the development of chemical modifications of the surface of the inorganic nanoparticles with organic molecules. For example, Klajn used the formation of self-assembled monolayers to decorate the surfaces of gold or silver particles.[45] The groups of Veinot and Rieger used covalent silicon carbon bonds to functionalize silicon nanocrystals with various organic molecules and tune the properties of the nanoparticles.[46,47] Both types of nanoparticles, gold, and silicon, will be building blocks for the dissipative self-assembly in proceeding chapters.

In the following paragraph, I will discuss three examples of nanoparticular building blocks in self-assembly processes. The three have all their advantages and disadvantages. This results in the last introductory chapter, where I describe the aim of this thesis.

Van Esch and co-workers used a polymeric nanoparticle with polystyrene core a layer of N-isopropyl acrylamide polymer and a partially hydrolyzed polymethyl methacrylate surface.[48] The self-assembly of these 700 nm particles is induced by the addition of a methylating agent and the chemical reaction cycle functions as described in Figure 7. The activation reaction abolishes some of the charges and thereby increases the hydrophobic character of the particles. This hydrophobization is the driving force for the self-assembly. The size of the nanoparticles is sufficiently large to allow following the behavior with a light microscope. Moreover, dynamic light scattering spectroscopy shows the size change of the agglomerating nanoparticles and reveals a transient increase in size. Due to the relatively slow hydrolysis, the chemical cycle takes more than a day to reinstate equilibrium, which limits the possibilities of this system. Nevertheless, it does demonstrate that the controlled clustering of nanoparticular building blocks is possible.

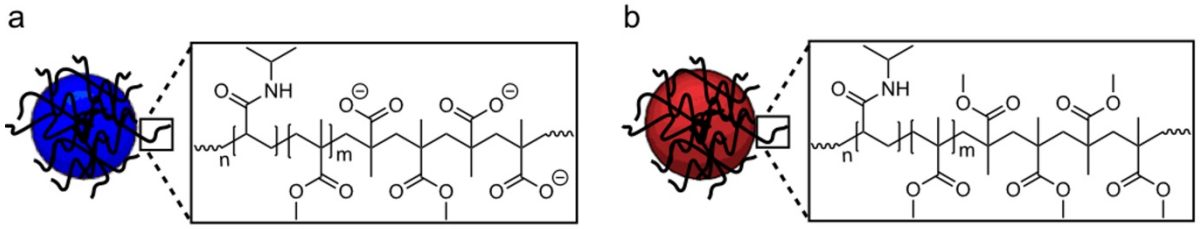

Figure 9: *Polymer-based building block: The 700 nm diameter nanoparticle consists of a polystyrene core with a N-isopropyl acrylamide polymer middle layer and a partially hydrolyzed methyl methacrylate surface. a) Precursor state in blue with many charges on the hydrolyzed methyl methacrylate polymer. b) Product state with unhydrolyzed methyl methacrylate.*

Klajn et al. used gold and silver nanoparticles as building blocks in dissipative self-assembly.[49] The nanoparticles are decorated with trans-4(mercaptoundecanoxy)azobenzene and dodecyl amine to form a stable particle with a size of 6 nm. Instead of a chemical fuel, the isomerization from the trans to the cis conformation induces clustering which is driven by the absorption of UV-light. By removing the source of UV light, the cis-state spontaneously reverts to the trans configuration. This process can be accelerated with visible light and heat. The change in the dipole moment between trans and cis conformation is the driving force to form

agglomerates of the nanoparticles decorated with molecules in cis configuration. The agglomerated nanoparticles shift the color of the solution from red to purple. After embedding the particles in a hydrogel, this color change was used to write messages. A mask blocked parts of the UV light and so only the areas where the light reached the nanoparticles turned blue. After some time, the blue color vanished, i.e., the cis azobenzenes switched back to the trans conformation, and the nanoparticles separated again. Now a new image can be written in the same material.

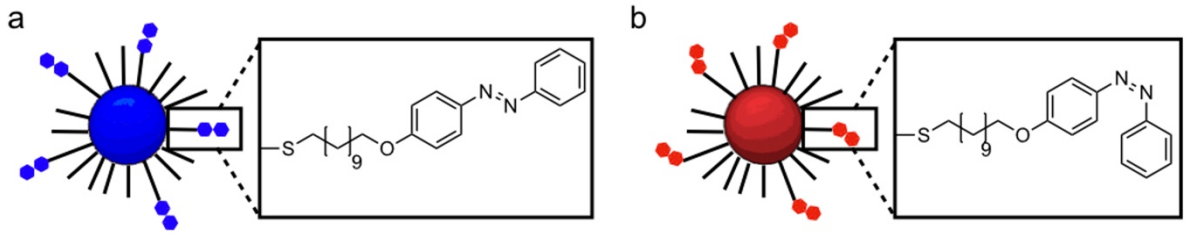

Figure 10: *Gold or silver nanoparticles with a diameter of 6 nm. a) Precursor state in blue with trans-4-(mercaptoundecanoxy)azobenzene and dodecyl amine surface functionalization. b) Product state in red with cis-4-(mercaptoundecanoxy)azobenzene and dodecyl amine surface functionalization.*

This reusability demonstrates that with dissipative self-assembly, it is possible to control the time of the color change as well as the area.

A different approach to use nanoparticles as building blocks in a dissipative assembly was described by Walther et al.[50] Instead of changing a molecule on the surface of the nanoparticle, the DNA i-motif strand that is attached is sensitive towards pH changes. This sensitivity means that at acidic pH, the DNA self-folds and the nanoparticles of 20 nm diameter form a stable colloidal solution. This is the precursor state and depicted in Figure 11a. Then the pH is changed transiently via two chemicals. The first one is the basic buffer TRIS that nearly instantaneously raises the pH from 5.5 to 8.5. The relative slow hydrolysis of β-butyrolactone compared to the addition of TRIS brings the pH down to 4.5. At a pH above 6, the i-motif strand unfolds into the product state and is available for the duplex formation of a complementary strand (Figure 11b). Nanoparticles with this complementary strand are already present in solution and start to form agglomerates with the product particles. The formation of hydrogen bonds is

the driving force of the agglomeration. This is only possible if the cytosine nucleobases are not partially protonated at lower pHs.

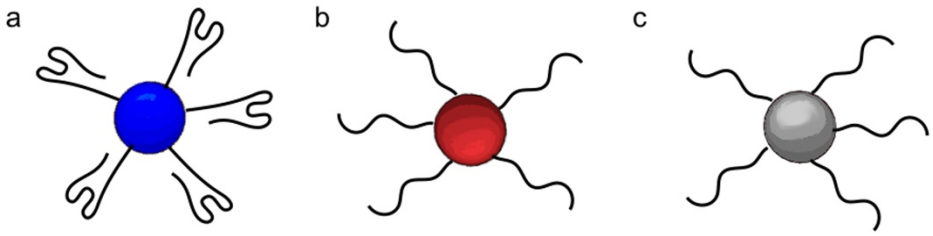

Figure 11: *Gold nanoparticles with a diameter of 20 nm. a) Precursor state in blue with DNA i-motif switch and thiolated poly(thymine) on the surface. Under acidic conditions, the i-motif switch forms a self-folded DNA strand. b) Product state in red with DNA i-motif switch and thiolated poly(thymine) on the surface. Under basic conditions, the i-motif switch forms an active DNA to form a duplex with the complementary strand. c) Complementary nanoparticle in grey with complementary DNA strand and thiolated poly(thymine) on the surface.*

Aim of the Thesis

Biology demonstrates the ultimate power of supramolecular materials. I describe in Chapter 2, the microtubule network as an example, which shows unique material properties like self-healing, adaptivity, and spatio-temporal control. Synthetic chemists and material scientist have the power to create non-natural materials and push a step beyond what biology can do. The nanoparticles mentioned in Chapter 4 are a prime example of that. Combining the unique properties of dissipative self-assembly, as observed in biology, with the non-natural nanoparticles-based materials is thus the aim of this thesis. While some steps towards that goal have been set by others. The examples of nanoparticles in dissipative self-assembly so far are working under extreme conditions with toxic fuels, are relying on light as a fuel source or show an indirect way of stimulus response.

The first step in the thesis is to develop a chemical reaction cycle that can be used in a biological setting. I should thus find a reaction cycle that operates under physiological or close to physiological conditions without the use of toxic chemicals. In Chapter 5, I describe the development of such a reaction cycle with gold nanoparticles. Gold nanoparticles are of interest as they are a reference system for nanoparticles. The characterization of this cycle leads to a deeper understanding of the energy landscapes and shows for the first time pathways selective behavior in dissipative self-assembly of nanoparticles.

With the new chemical reaction cycle that functions under physiological conditions, new materials for biomedical applications should be developed. The shift from gold to silicon nanoparticles offers the excellent biocompatibility and the abundance of the element silicone in the earth crust. In chapter 6, I develope such a material based on silicon nanoparticles that can be used as a drug delivery platform.

Moreover, the use as a sensing agent should be examined with photoluminescent silicon nanoparticles. This leads to the findings in Chapter 7.

In conclusion, the thesis aim is to develop a new chemical reaction cycle that induces the dissipative self-assembly of nanoparticles. Finally, the use of the nanomaterial in applications can demonstrate the accomplished spatio-temporal control of the material, similar to the biological paragon.

Pathway Dependence in the Fuel-Driven Self-Assembly of Nanoparticles.

Abstract.

In this work, we describe the newly developed dissipative self-assembly of gold and iron oxide nanoparticles driven by a chemical fuel. The nanoparticles are endowed with a carboxylate shell. Due to the anionic charges of the carboxylates, these particles are well-soluble in water. Addition of a chemical fuel, 1-ethyl-3-(3-dimethylaminopropyl) carbodiimide (EDC), in combination with a nucleophilic chemical, N-Hydroxysuccinimide, changes their hydrophobicity. This change from charged carboxylates to N-Hydroxysuccinimide esters induces the self-assembly. Hydrolysis of the esters induces disassembly and reinstates the initial state. In other words, those reactions form a complete reaction cycle with a precursor that is activated to the product and spontaneously deactivates from the product back to the precursor. However, upon addition of fuel, we encountered three distinct behaviors: no assembly, dissipative self-assembly, and a kinetically trapped assembly. This behavior can be exploited in pathway complexity experiments that lead to nanomaterials with the same chemical composition but different states in the energy landscape and thus in the material appearance. In conclusion, when using chemical reactions to drive the self-assembly of nanoparticle or molecules, one should not only consider the reaction cycle, but also the energy landscapes involved in the self-assembly.

This work has been published:

Title:	Pathway Dependence in the Fuel-Driven Self-Assembly of Nanoparticles.
Authors:	Raphael K. Grötsch, Caren Wanzke, Maximilian Speckbacher, Arzu Angı, Prof. Dr. Bernhard Rieger, Prof. Dr. Job Boekhoven
First published:	03. June 2019
Journal:	Journal of the American Chemical Society, **2019**, 1431, 25, 9872 – 9878.
Publisher:	American Chemical Society
DOI:	10.1021/jacs.9b02004

Reprinted with permission from J. Am. Chem. Soc. **2019**, 1431, 25, 9872 – 9878.

This section states the individual work of each author in the publication above. R. K. Grötsch designed and conducted all experiments. C. Wanzke imaged with a cryogenic transmission electron microscope the different nanoparticle states in solution and M. Speckbacher conducted the scanning electron microscope measurements of precipitated and drop casted nanoparticle agglomerates. A. Angı helped with IR measurements to identify the chemical reaction cycle. The manuscript was written by R. K. Grötsch and J. Boekhoven. The work was performed under the supervision and guidance of B. Rieger and J. Boekhoven.

JACS
JOURNAL OF THE AMERICAN CHEMICAL SOCIETY
Article
Cite This: J. Am. Chem. Soc. 2019, 141, 9872−9878
pubs.acs.org/JACS

Pathway Dependence in the Fuel-Driven Dissipative Self-Assembly of Nanoparticles

Raphael K. Grötsch,[†] Caren Wanzke,[†] Maximilian Speckbacher,[‡] Arzu Angı,[†,⊥] Bernhard Rieger,[†,⊥] and Job Boekhoven*[,†,∥]

[†]Department of Chemistry and [∥]Institute for Advanced Study, Technical University of Munich, Lichtenbergstraße 4, 85748 Garching, Germany

[‡]Molecular Electronics, Department of Electrical and Computer Engineering, Technical University of Munich, Thersienstraße 90, 80333 Munich, Germany

[⊥]Wacker-Chair of Macromolecular Chemistry, Catalysis Research Center, Ernst-Otto-Fischer-Straße 1, 85747 Garching, Germany

Supporting Information

ABSTRACT: We describe the self-assembly of gold and iron oxide nanoparticles regulated by a chemical reaction cycle that hydrolyzes a carbodiimide-based fuel. In a reaction with the chemical fuel, the nanoparticles are chemically activated to a state that favors assembling into clusters. The activated state is metastable and decays to the original precursor reversing the assembly. The dynamic interplay of activation and deactivation results in a material of which the behavior is regulated by the amount of fuel added to the system; they either did not assemble, assembled transiently, or assembled permanently in kinetically trapped clusters. Because of the irreversibility of the kinetically trapped clusters, we found that the behavior of the self-assembly was prone to hysteresis effects. The final state of the system in the energy landscape depended on the pathway of preparation. For example, when a large amount of fuel was added at once, the material would end up kinetically trapped in a local minimum. When the same amount of fuel was added in small batches with sufficient time for the system to re-equilibrate, the final state would be the global minimum. A better understanding of pathway complexity in the energy landscape is crucial for the development of fuel-driven supramolecular materials.

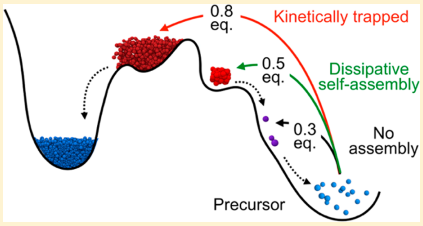

INTRODUCTION

In supramolecular materials, molecules or nanoparticles assemble into larger, more complex structures.[1−4] The building blocks in these assemblies are held together by noncovalent interactions, which result in materials that have vastly different properties compared to their nonassembled building blocks. Particularly successful examples of building blocks include amphiphiles,[5] gelators,[6] peptides,[7] and nanoparticles functionalized with DNA.[8] The type of assembly and its associated material properties can be encoded in the molecular design of the building blocks, resulting in exciting materials like supramolecular polymers that can regulate cell behavior.[9−11] However, recent work has demonstrated that the intended self-assembled state is sometimes not reached, because the assemblies can trap molecules in a local minimum in their energy landscape.[12−14] Such systems are prone to hysteresis effects, which means that the order in which the assembly is prepared can affect the final state. Even if the composition of the final material is the same, its material properties can differ depending on the preparative pathway.[15−18] The properties of supramolecular materials are thus not only dependent on the molecular design of the building blocks but can also depend on the pathway of preparation of the materials.

In dissipative self-assembly, the self-assembly of molecules or nanoparticles is regulated by a chemical reaction cycle.[19−21] The reaction cycle comprises a fuel-driven activation reaction and a spontaneous deactivation reaction. In the activation reaction, a precursor reacts irreversibly with a chemical fuel giving rise to a building block for self-assembly. The deactivation reaction spontaneously reverts the building block to the precursor. The consequence of the reaction cycle is that building blocks have a finite lifetime. The finite lifetime of the building blocks in the assemblies means that the assemblies are dynamic[22−24] and evolve. The emerging material properties are controlled by kinetic parameters, like the initial concentration of fuel[25] and feedback of the assemblies on their reaction cycle,[26,27] which leads to exciting materials like self-abolishing supramolecular gels,[22,28] self-erasing inks,[29] solutions of supramolecular polymers that oscillate between morphologies,[30] and solutions of nano-

Received: February 27, 2019
Published: June 3, 2019

DOI: 10.1021/jacs.9b02004
J. Am. Chem. Soc. 2019, 141, 9872−9878

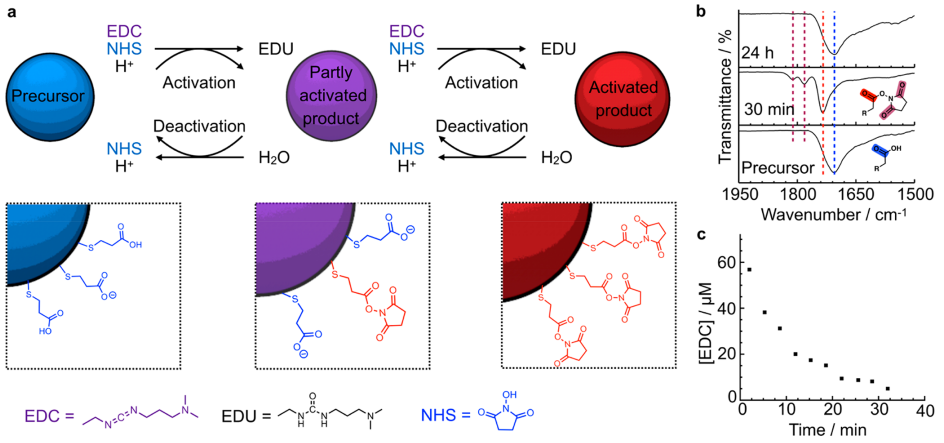

Figure 1. (a) The chemical reaction cycle driven by the hydrolysis of EDC. The carboxylates on a gold nanoparticle can react with EDC and NHS to form the corresponding NHS ester (activation). The intrinsically unstable NHS-ester deactivates over time into the precursor via its hydrolysis. Depending on the amount of EDC added, the precursor is partly or fully activated. (b) FTIR spectra of the nanoparticles before and 30 min and 24 h after the addition of 0.5 equiv (125 μM) of EDC to a solution of the precursor. Dashed lines from purple to blue mark the peaks for 1811, 1782, 1734, and 1705 cm^{-1}. (c) The EDC concentration as a function of time for the same experimental condition as described in (b).

particles clusters that degrade over time.[31−33] Despite these exciting material properties, fundamental understanding of the energy landscapes and evolving material properties of fuel-driven dissipative self-assembly, in particular, in the context of pathway complexity, is lacking.

RESULTS AND DISCUSSION

In this work, we describe that pathway dependence is also applicable to dissipative self-assembly. We use gold and iron oxide nanoparticles as precursors in a chemical reaction cycle. The hydrolysis of condensing agents drives the reaction cycle. Upon activation, the nanoparticles can either remain unassembled, assemble into transient clusters, or form a kinetically trapped assembly, depending on the amount of fuel added. However, we also find that the same amount of fuel can result in a different response depending on the chosen preparative pathway.

As building blocks, we used carboxylate-terminated gold or iron oxide nanoparticles with a diameter of 3.5 and 15 nm, respectively, as measured by cryogenic transmission electron microscopy (see Materials and Methods in Supporting Information and Figure SI1). These nanoparticles were well-soluble in water, and we regulated their assembly behavior by a chemical reaction cycle we recently introduced (Figure 1a).[31] In the reaction cycle, the carboxylate groups on the particles were transiently converted in their corresponding *N*-hydroxysuccinimide (NHS) ester driven by the hydrolysis of 1-ethyl-3-(3-(dimethylamino)propyl)-carbodiimide (EDC). In the activation reaction, the EDC reacted irreversibly with the surface-bound carboxylic acid groups and NHS in the solution to form the corresponding metastable NHS-ester. In the deactivation, the NHS-ester hydrolyzed to the original carboxylic acid state. In the buffer at pH 6.4, the carboxylic acids on the nanoparticles in solution were to some degree deprotonated rendering them well-soluble in water. In contrast, the NHS-ester is uncharged, and the loss of charge was expected to induce the clustering of the particles, thereby inducing the dissipative self-assembly of the nanoparticles.

We assessed the behavior of the gold nanoparticles in response to EDC by Fourier transformed infrared (FTIR) spectroscopy. We prepared a solution of the nanoparticles at a concentration of 250 μM acid groups (Figure SI2) in 25 mM NHS and 20 mM 2-(*N*-morpholino)ethanesulfonic acid (MES) buffer at pH 6.4, which yielded a reddish solution. We consider the concentration of 250 μM acid groups as 1 equiv when calculating the amount of EDC we added to initiate the reaction cycle. In other words, 1.0 equiv of EDC could theoretically convert all acid groups on the particles into their corresponding NHS-ester. On the basis of the diameter of the gold nanoparticles and assuming a surface area per mercaptopropionic acid of 0.16 nm^2,[34] we calculated that, on average, each particle carries 250 molecules of mercaptopropionic acid (see Methods section in Supporting Information). The FTIR spectroscopy on the particles before the addition of EDC revealed a clear band associated with the carbonyl of a carboxylic acid (Figure 1b). We added 0.5 equiv of EDC (125 μM) to the precursor solution to initiate the reaction cycle and observed the formation of three new bands, which we associated with the carbonyls of the NHS-ester. After 24 h, FTIR showed that the three new bands had disappeared. In other words, the spectrum was similar to the spectrum of the precursor. Similar trends in the FTIR data were found when 0.3 equiv (75 μM) or 0.8 equiv (200 μM) of EDC was added to the solutions (vide infra, Figure SI3).

We used high-pressure liquid chromatography (HPLC) to follow the evolution of the concentration of EDC during the reaction cycle. We found a sharp decay of the concentration of EDC in the first minute, which we explain by a previously described side reaction between EDC and NHS.[35] We found a further decline in the EDC concentration over time, which is

DOI: 10.1021/jacs.9b02004
J. Am. Chem. Soc. 2019, 141, 9872−9878

the result of the reaction of the carboxylic acid groups on the surface of the particles with the EDC (Figure 1c). After 30 min, most of the EDC had been consumed by the reaction cycle. The combination of FTIR and HPLC analytics show strong evidence for the chemical reaction cycle described in Figure 1a.

Characterizing the macroscopic behavior of the nanoparticle solution upon the addition of EDC was the next step. In a first experiment, the precursor was fueled with 0.3, 0.5, or 0.8 equiv of EDC. By time-lapse photography, no apparent changes were visible in the first 30 min for any of the samples. However, as time progressed, the solution fueled with 0.8 equiv of EDC showed the formation of a precipitate, while the supernatant became clear (Figure 2a). We followed the evolution of the

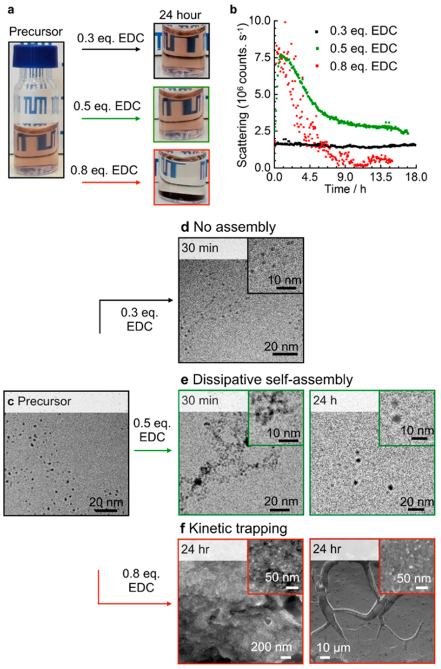

Figure 2. (a) Photographs of the solutions before (precursor) and 24 h after EDC addition. (b) The scattering rates as measured by DLS as a function of time for different amounts of EDC added to the nanoparticles. (c–e) Cryo-TEM micrographs of the precursor solution, a solution 30 min after fueling with 0.3 equiv of EDC (d) and a solution 30 min and 24 h after fueling with 0.5 equiv of EDC. (f) SEM micrographs of the precipitate formed by fueling the precursor with 0.8 equiv of EDC.

material in more detail using dynamic light scattering (DLS). We measured that the particles had a hydrodynamic diameter of 13 nm before the addition of EDC. With 0.3 equiv of EDC, we did not observe any evidence of self-assembly by DLS. That means, neither the size of the particles nor the total scattering rate was affected by the addition of EDC (Figures 2b and SI4). The lack of assemblies is a strong indication that an insufficient amount of NHS-ester per particle is formed to overcome the interparticle repulsion, and thus no assembly was induced. In contrast, when we added 0.5 equiv of EDC, the scattering rate increased from 2 to 7.5 Mcps, while the mean hydrodynamic diameter of the particle in solution increased from 13 to 41 nm in the first hour (Figure SI4). After 2 h, the scattering decreased gradually to a value close to the original level. In that time frame, the radius had also decreased to the original 12 nm. These combined experiments suggest that we can induce transient self-assembly of the gold nanoparticles provided that a sufficient amount of EDC is added. When the nanoparticles were fueled by 0.8 equiv of EDC, DLS showed a similar rapid increase in the size and scattering rate, pointing toward the assembly of the particles. However, the scattering rate as a function of time became noisy, and the radius could not be fitted reliably. The scattering rate dropped to a level far below the original value after 6 h and never came back to the original level. We explain the loss of scattering to the precipitation of the gold nanoparticles in line with the observations made by time-lapse photography.

To confirm that the self-assembly was driven by the hydrophobization upon forming the NHS-ester, we performed two control experiments with DLS. These experiments rule out, for example, that the intermediate *O*-acylisourea[35] was causing the agglomeration. First, we exchanged the NHS in solution for the anionic *N*-hydroxysulfosuccinimide (sulfo-NHS) and fueled the experiment with 0.5 equiv of EDC. In this experiment, DLS showed no evidence of self-assembly. In a second experiment, no NHS was present when we fueled with 0.5 equiv of EDC. Again, DLS showed no evidence of assembly. Both experiments demonstrate that the hydrophobic NHS is required to induce assembly (Figure SI5).

We used electron microscopy to analyze the assembly of the gold nanoparticles induced by EDC. Before the cycle was initiated, cryo-TEM showed individual nanoparticles and small aggregates of the nanoparticles (Figure 2c). When the solution was imaged 30 min after the addition of 0.3 equiv of EDC, we found a similar scenario, that is, predominantly nonassembled nanoparticles (Figure 2d). In contrast, when we added 0.5 equiv of EDC as fuel, we found clusters of the particles. These clusters comprised hundreds of particles that were relatively loosely packed (Figures 2e and SI6). Moreover, after 24 h the clusters were not observed, but instead, mostly individual nanoparticles were found reminiscent of the precursor state. The electron microscopy data, combined with the DLS data and the study on the kinetics of the reaction cycle, provide compelling data to conclude that we can induce the transient dissipative assembly of gold nanoparticles under these conditions.

In contrast, when we investigated the sample that was fueled with 0.8 equiv of EDC by scanning electron microscopy (SEM), we observed assemblies of several hundreds of micrometers (Figure 2f). We tried cryo-TEM imaging, but because of the size of the clusters, it was not possible. These large assemblies consisted of thousands of nanoparticles. The size of these assemblies explains why they precipitated. Moreover, the size could also explain why, after 24 h, the structures had not disassembled. Samples stored for four weeks also showed the precipitation (Figure SI7), which seems to suggest that the precipitate traps the particles into an assembly from which they cannot escape.

The nanoparticles could be kinetically trapped because of two reasons. Either the nanoparticles are densely packed and

DOI: 10.1021/jacs.9b02004
J. Am. Chem. Soc. 2019, 141, 9872–9878

exclude all the water from the assemblies, which inhibits the hydrolysis (deactivation) reaction and, thus, inhibits the disassembly. We found a similar mechanism of inhibition of hydrolysis in other work.[36] Alternatively, because of the relatively high fuel concentration, the particles form a large assembly and can undergo strong noncovalent interactions (e.g., hydrogen bonding of the carboxylic acids or van der Waals interactions), such that the energy barrier for disassembly becomes too high to overcome. Such kinetic trapping of nanoparticles, even in their deactivated state, has been demonstrated before for gold nanoparticles that self-assembled in response to light.[37]

To test the first hypothesis, we performed an FTIR study on the assemblies after addition of 0.8 equiv of EDC and tested whether the surface of the nanoparticles reverted to their original state. For these clusters, NHS-ester bands could be measured after 24 h (Figure 3a; Figure SI8 for full spectra).

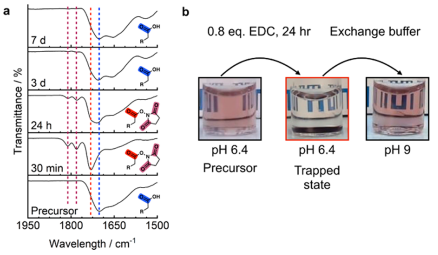

Figure 3. (a) FTIR analyses of the sample fueled with 0.8 equiv of EDC over time. (b) Photographs before and 24 h after the addition of 0.8 equiv of EDC. Only by addition of buffer at pH 9 could the nanoparticles be redissolved.

That seems to suggest that hydrolysis is delayed, because these bands were not visible after 24 h in the dissipative self-assembling sample (vide supra, Figure 1b). However, 7 d after addition of the 0.8 equiv of EDC, the FTIR showed that the NHS ester had fully hydrolyzed and that the precursor state was recovered from a surface chemistry point of view. Nevertheless, the deactivated nanoparticles remained in a precipitate. The combined observation seems to suggest that both hypothesized mechanisms play a role: the large scale of the assemblies slows the hydrolysis but does not inhibit it entirely, and the large assemblies kinetically trap the nanoparticles, whether they are in the activated state or not.

We found that samples fueled with more than 0.8 equiv of EDC behaved similarly; that is, all samples resulted in a precipitate that did not dissolve (Figure SI9). Vigorously shaking, sonicating or heating these samples did not bring the precipitated nanoparticles back to their precursor state. Only by increasing the pH from 6.4 to 9.0 by exchanging the buffer could we redissolve the precipitate (Figure 3b). This observation also confirms that the particles are trapped by noncovalent reversible interactions, which can be overcome by increasing the interparticle electrostatic repulsion.[38] Indeed, a final electron microscopy study demonstrated that the particles, before initiating the cycle and after 24 h in the kinetically trapped state, had similar diameters as measured by conventional TEM (Figure SI10). Because the kinetically trapped clusters were large, we chose to use conventional TEM over cryo-TEM in this experiment. That observation rules out that the particles coalesced when trapped in the precipitate. Taken together, the precipitate comprised the particles that were kinetically trapped due to noncovalent interactions.

The combined data set allows us to sketch an overview of the pathways and energy landscapes involved in the fuel-driven self-assembly of the nanoparticles (Figure 4). In the reaction

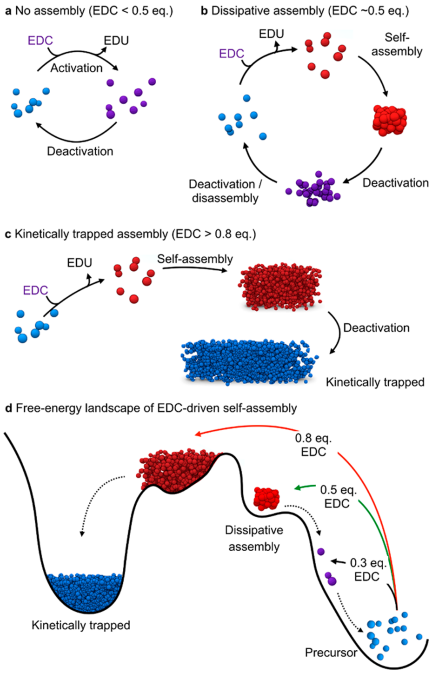

Figure 4. Pathways of self-assembly driven by a chemical reaction cycle. (a) The nonassembling cycle. (b) The dissipative self-assembling cycle. (c) The pathway that was resulting in kinetically trapped particles. (d) Schematic representation of the free energy landscape of the EDC driven self-assembly. Solid lines are uphill events that consume energy. Dashed lines are spontaneous downhill events. Note that there is no pathway from the kinetically trapped state to the precursor state.

pathways, there is a minimum amount of fuel required to induce the self-assembly of the activated state; that is, when 0.3 equiv or less of EDC was used, we observed the NHS-ester but no evidence for self-assembly. We refer to this as the nonassembling pathway (Figure 4a). In contrast, when 0.5 equiv of fuel was added, the reaction cycle formed particles that were sufficiently activated to induce their self-assembly. The particles disassembled over time, which was driven by the deactivation reaction. We refer to this as the dissipative self-assembly pathway; that is, the particles transiently assemble by dissipating energy obtained from the reaction cycle (Figure 4b). Finally, when more than 0.5 equiv of fuel was added, the particles were sufficiently activated for assembly. However, they assembled in a tightly clustered state that inhibited deactivation to some degree. Moreover, after deactivation, the

DOI: 10.1021/jacs.9b02004
J. Am. Chem. Soc. 2019, 141, 9872−9878

particles remained kinetically trapped in the large assemblies (Figure 4c).

In Figure 4d, we depict a tentative energy landscape of the self-assembly of the nanoparticles driven by EDC. The precursor state (right) is likely the global minimum of the landscape. When EDC (energy) is added, the population can shift uphill. For example, when 0.3 equiv is added (non-assembling pathway), the particles are activated but freely fall back to the precursor state over time. When 0.5 equiv is added, the particles are further activated and can assemble. That nonequilibrium state represents a local minimum in the landscape. Its low energy barrier ensures that the particles can disassemble over time. Finally, when 0.8 equiv of fuel is added, the particle reaches another local minimum. This minimum is characterized by a high-energy barrier toward the precursor state. Instead, after deactivation, the state remains kinetically trapped in a final local minimum.

While the dissipative self-assembly of nanoparticles driven by various chemical reaction cycles has been demonstrated before,[29,32,39] the notion of kinetically trapping has been underexplored.[37] To test if the fuel-driven self-assembly and kinetic trapping that we described in this work is unique to one precursor, we tested the chemical reaction cycle to drive the self-assembly of carboxylate-terminated iron oxide nanoparticles. We used commercially available nanoparticles with a diameter of 15 ± 2 nm as measured by cryo-TEM (see Figure SI1) and a hydrodynamic diameter of 28 ± 7 nm as measured by DLS (Table SI1). Besides the fact that these particles are based on a different metal, they also carry a different surface chemistry. The iron oxide particles were covered with a monolayer of oleic acid, which was then coassembled with hydrolyzed poly(maleic anhydride-*alt*-1-octadecene). The concentration of surface-bound carboxylates was 5 mM in a buffer of 200 mM MES at pH 6.5 and 20 mM NHS. We considered the concentration of 5 mM acid groups as 1 equiv when calculating the equivalents of EDC to add. In line with the previous observations, the behavior of the solution depended on the amount of EDC we added. For the addition of 0.4 equiv of EDC (2.0 mM), no change by time-lapsed photography or by DLS was detected (Figure 5a,b). In contrast, when we added 2.0 equiv of EDC (10 mM), we observed precipitation of the iron oxide nanoparticles. DLS showed a rapid increase in the scattering rate after which it decayed to zero. These observations are in line with the kinetic trapping scenario observed for the gold nanoparticles. We used IR spectroscopy to confirm the transient formation of the NHS-ester. When 0.4 or 2.0 equiv of EDC was added, we observed the peaks characteristic for the NHS ester. Moreover, for 0.4 equiv, the peaks were not visible within 24 h. In contrast, for 2.0 equiv, it took 3 d to show similar bands as before the addition of EDC (Figures 5c,d and SI11 for full spectra). The combined data sets suggest that the behavior of the EDC-driven chemical reaction cycle is similar for gold and iron oxide nanoparticles that carry a carboxylate group on their surface.

The notion that two of the EDC-driven pathways were reversible (nonassembling and dissipative assembling) and a third pathway was not (kinetically trapped) prompted us to explore pathway complexity experiments, that is, an experiment in which the pathway to the same final conditions leads to different outcomes. We compared the outcome of two experiments that both received more than the 0.8 equiv of fuel. In one experiment, we added the fuel in small batches of less than 0.5 equiv. In the other experiment, we added all fuel at once.

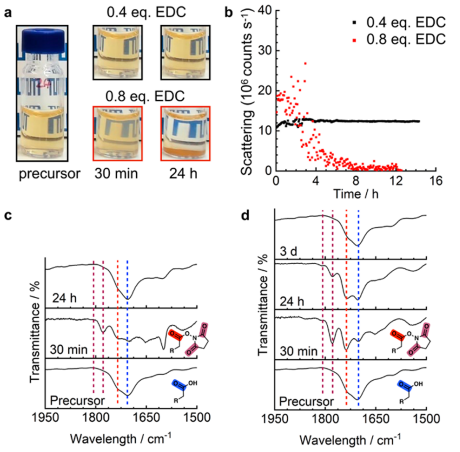

Figure 5. (a) Photographs of the iron oxide nanoparticle solutions before (precursor), 30 min, and 24 h after EDC addition. (b) The scattering rates as measured by DLS as a function of time for different amounts of EDC added to the nanoparticles. (c, d) FTIR diagram of the precursor, 30 min and 24 h after addition of 0.4 (c) and 0.8 (d) equiv of EDC to a solution of the precursor. Dashed lines from purple to blue mark the peaks for 1811, 1782, 1734, and 1705 cm^{-1}.

Specifically, we added three batches of 0.3 equiv of EDC at 24 h intervals to the gold nanoparticles. In another experiment, we added two batches of 0.45 equiv of EDC with 36 h intervals. In a final experiment, we added 0.9 equiv in one batch and waited for 72 h (Figure 6a). The multiple additions of smaller batches of fuel resulted in a solution of the nanoparticles with no evidence of precipitation over the entire course of the experiment. In contrast, when the 0.9 equiv were added to the nanoparticles in one batch, the experiment resulted in precipitation. After 72 h, all solutions were measured by DLS spectroscopy, which showed similar diameter and count rates as the precursor sample for the first two samples. In contrast, the sample fueled with 0.9 equiv of fuel showed a greater radius and a lower count rate, confirming the kinetically trapped state (see Table SI2).

We added to the iron oxide nanoparticles five batches of 0.4 equiv of EDC with two-day intervals, as well as 2.0 equiv in one batch (Figure 6b). While no precipitation was observed for the sequentially fueled sample, the other sample resulted in the formation of a precipitate within hours after addition of the fuel, which remained present during the entire experiment. DLS spectroscopy confirmed that the sequentially fueled sample showed similar scattering rate and particle diameter compared to the precursor. In contrast, the sample that received the same amount of fuel, but all at once, showed no reliable scattering data, indicative of the kinetically trapped precipitate (see Table SI2).

CONCLUSIONS

Our work shows that the self-assembly behavior of gold and iron oxide nanoparticles can be regulated by an EDC-driven chemical reaction cycle that converts carboxylates on the

DOI: 10.1021/jacs.9b02004
J. Am. Chem. Soc. 2019, 141, 9872−9878

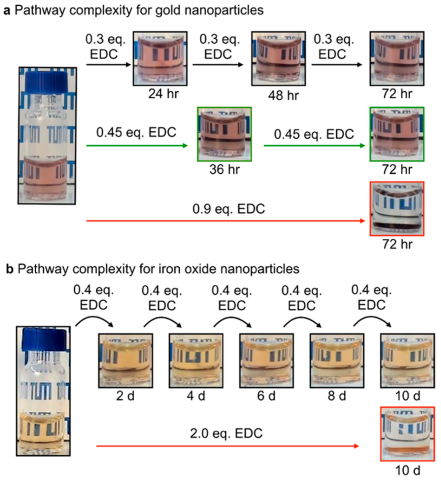

Figure 6. (a) Pathway complexity in the EDC-driven reaction cycle involving gold- (a) or iron oxide- (b) based nanoparticles as a precursor.

particle to their corresponding NHS-esters. With small amounts of EDC, the nanoparticles are activated, but to an insufficient degree for self-assembly. When more EDC is added, the gold or iron oxide nanoparticles assemble dissipatively driven by the reaction cycle; that is, they assemble and disassemble after EDC has been depleted. In contrast, when a large amount of EDC is added, the nanoparticles form large assemblies that remain kinetically trapped. The notion of a fuel-dependent kinetic trap implies that the behavior of the system is prone to pathway complexity; that is, the final position of the gold and iron oxide nanoparticles in their free energy landscape may depend on the preparative pathway. Indeed, we find that, when a large amount of EDC is added in small batches, it does not result in a kinetically trapped state. In contrast, when the same amount of EDC is added at once, it results in the irreversible kinetic trapping of the assemblies. In other words, two solutions of gold or iron oxide nanoparticles that are of the same final compositions (buffer, pH, temperature, reagents, and products) but have a different preparative history can result in different states in the energy landscape. The associated material properties are thus also dependent on sample history. To further develop supramolecular materials with complexity and sophistication as observed in living materials, an understanding of the relations between energy landscapes, material properties, and pathways complexity is fundamental.

■ ASSOCIATED CONTENT

Supporting Information

The Supporting Information is available free of charge on the ACS Publications website at DOI: 10.1021/jacs.9b02004.

Materials and methods, DLS data, TEM, SEM, and FTIR spectra, titration data (PDF)

■ AUTHOR INFORMATION

Corresponding Author

*job.boekhoven@tum.de

ORCID

Bernhard Rieger: 0000-0002-0023-884X

Job Boekhoven: 0000-0002-9126-2430

Funding

Deutsche Forschungsgemeinschaft via the International Research Training Group ATUMS (IRTG 2022) European Union Seventh Framework Programme under Grant No. 291763.

Notes

The authors declare no competing financial interest.

■ ACKNOWLEDGMENTS

R.K.G., B.R., M.S., and J.B. are grateful for funding from the Deutsche Forschungsgemeinschaft via the International Research Training Group ATUMS (IRTG 2022). C.W. is grateful for funding from the Deutsche Forschungsgemeinschaft through Transregional Collaborative Research Center (SFB/Transregio) 235 Project 16. J.B. is grateful for funding by the Technical University of Munich–Institute for Advanced Study, funded by the German Excellence Initiative and the European Union Seventh Framework Programme under Grant No. 291763. A.A. acknowledges funding from Studienstiftung des Deutschen Volkes.

■ REFERENCES

(1) Amabilino, D. B.; Smith, D. K.; Steed, J. W. Supramolecular materials. *Chem. Soc. Rev.* **2017**, *46* (9), 2404–2420.

(2) Stupp, S. I.; LeBonheur, V. V.; Walker, K.; Li, L. S.; Huggins, K. E.; Keser, M.; Amstutz, A. Supramolecular Materials: Self-Organized Nanostructures. *Science* **1997**, *276* (5311), 384–9.

(3) Aida, T.; Meijer, E. W.; Stupp, S. I. Functional supramolecular polymers. *Science* **2012**, *335* (6070), 813–7.

(4) Lampel, A.; McPhee, S. A.; Park, H. A.; Scott, G. G.; Humagain, S.; Hekstra, D. R.; Yoo, B.; Frederix, P.; Li, T. D.; Abzalimov, R. R.; Greenbaum, S. G.; Tuttle, T.; Hu, C.; Bettinger, C. J.; Ulijn, R. V. Polymeric peptide pigments with sequence-encoded properties. *Science* **2017**, *356* (6342), 1064–1068.

(5) Israelachvili, J. N.; Mitchell, D. J.; Ninham, B. W. Theory of self-assembly of hydrocarbon amphiphiles into micelles and bilayers. *J. Chem. Soc., Faraday Trans. 2* **1976**, *72*, 1525–1568.

(6) van Esch, J. H.; Feringa, B. L. New Functional Materials Based on Self-Assembling Organogels: From Serendipity towards Design. *Angew. Chem., Int. Ed.* **2000**, *39* (13), 2263–2266.

(7) Hartgerink, J. D.; Beniash, E.; Stupp, S. I. Self-assembly and mineralization of peptide-amphiphile nanofibers. *Science* **2001**, *294* (5547), 1684–8.

(8) Mirkin, C. A.; Letsinger, R. L.; Mucic, R. C.; Storhoff, J. J. A DNA-based method for rationally assembling nanoparticles into macroscopic materials. *Nature* **1996**, *382* (6592), 607–9.

(9) Zhang, S. Fabrication of novel biomaterials through molecular self-assembly. *Nat. Biotechnol.* **2003**, *21* (10), 1171–8.

(10) Alakpa, E. V.; Jayawarna, V.; Lampel, A.; Burgess, K. V.; West, C. C.; Bakker, S. C. J.; Roy, S.; Javid, N.; Fleming, S.; Lamprou, D. A.; Yang, J.; Miller, A.; Urquhart, A. J.; Frederix, P. W. J. M.; Hunt, N. T.; Péault, B.; Ulijn, R. V.; Dalby, M. J. Tunable Supramolecular Hydrogels for Selection of Lineage-Guiding Metabolites in Stem Cell Cultures. *Chem.* **2016**, *1* (2), 298–319.

(11) Silva, G. A.; Czeisler, C.; Niece, K. L.; Beniash, E.; Harrington, D. A.; Kessler, J. A.; Stupp, S. I. Selective differentiation of neural progenitor cells by high-epitope density nanofibers. *Science* **2004**, *303* (5662), 1352–5.

DOI: 10.1021/jacs.9b02004
J. Am. Chem. Soc. 2019, 141, 9872–9878

(12) Panettieri, S.; Ulijn, R. V. Energy landscaping in supramolecular materials. *Curr. Opin. Struct. Biol.* **2018**, *51*, 9−18.
(13) Sorrenti, A.; Leira-Iglesias, J.; Markvoort, A. J.; de Greef, T. F. A.; Hermans, T. M. Non-equilibrium supramolecular polymerization. *Chem. Soc. Rev.* **2017**, *46* (18), 5476−5490.
(14) Ogi, S.; Stepanenko, V.; Sugiyasu, K.; Takeuchi, M.; Wurthner, F. Mechanism of self-assembly process and seeded supramolecular polymerization of perylene bisimide organogelator. *J. Am. Chem. Soc.* **2015**, *137* (9), 3300−7.
(15) Tantakitti, F.; Boekhoven, J.; Wang, X.; Kazantsev, R. V.; Yu, T.; Li, J.; Zhuang, E.; Zandi, R.; Ortony, J. H.; Newcomb, C. J.; Palmer, L. C.; Shekhawat, G. S.; de la Cruz, M. O.; Schatz, G. C.; Stupp, S. I. Energy landscapes and functions of supramolecular systems. *Nat. Mater.* **2016**, *15* (4), 469−76.
(16) Korevaar, P. A.; Newcomb, C. J.; Meijer, E. W.; Stupp, S. I. Pathway selection in peptide amphiphile assembly. *J. Am. Chem. Soc.* **2014**, *136* (24), 8540−3.
(17) Merindol, R.; Loescher, S.; Samanta, A.; Walther, A. Pathway-controlled formation of mesostructured all-DNA colloids and superstructures. *Nat. Nanotechnol.* **2018**, *13* (8), 730−738.
(18) Leira-Iglesias, J.; Sorrenti, A.; Sato, A.; Dunne, P. A.; Hermans, T. M. Supramolecular pathway selection of perylenediimides mediated by chemical fuels. *Chem. Commun.* **2016**, *52* (58), 9009−9012.
(19) van Rossum, S. A. P.; Tena-Solsona, M.; van Esch, J. H.; Eelkema, R.; Boekhoven, J. Dissipative out-of-equilibrium assembly of man-made supramolecular materials. *Chem. Soc. Rev.* **2017**, *46* (18), 5519−5535.
(20) De, S.; Klajn, R. Dissipative Self-Assembly Driven by the Consumption of Chemical Fuels. *Adv. Mater.* **2018**, *30* (41), No. e1706750.
(21) Grötsch, R. K.; Boekhoven, J. Unique properties of supramolecular biomaterials through nonequilibrium self-assembly. In *Self-assembling Biomaterials;* Silva, R. M. P. D., Azevedo, H. S., Eds.; Woodhead Publishing, 2018; pp 235−250.
(22) Boekhoven, J.; Hendriksen, W. E.; Koper, G. J.; Eelkema, R.; van Esch, J. H. Transient assembly of active materials fueled by a chemical reaction. *Science* **2015**, *349* (6252), 1075−9.
(23) Debnath, S.; Roy, S.; Ulijn, R. V. Peptide nanofibers with dynamic instability through nonequilibrium biocatalytic assembly. *J. Am. Chem. Soc.* **2013**, *135* (45), 16789−92.
(24) Maiti, S.; Fortunati, I.; Ferrante, C.; Scrimin, P.; Prins, L. J. Dissipative self-assembly of vesicular nanoreactors. *Nat. Chem.* **2016**, *8* (7), 725−31.
(25) Tena-Solsona, M.; Wanzke, C.; Riess, B.; Bausch, A. R.; Boekhoven, J. Self-selection of dissipative assemblies driven by primitive chemical reaction networks. *Nat. Commun.* **2018**, *9* (1), 2044.
(26) Tena-Solsona, M.; Riess, B.; Grötsch, R. K.; Lohrer, F. C.; Wanzke, C.; Kasdorf, B.; Bausch, A. R.; Muller-Buschbaum, P.; Lieleg, O.; Boekhoven, J. Non-equilibrium dissipative supramolecular materials with a tunable lifetime. *Nat. Commun.* **2017**, *8*, 15895.
(27) Rieß, B.; Boekhoven, J. Applications of Dissipative Supramolecular Materials with a Tunable Lifetime. *Chem. Nano Mat* **2018**, *4* (8), 710−719.
(28) Heuser, T.; Steppert, A. K.; Molano Lopez, C.; Zhu, B.; Walther, A. Generic concept to program the time domain of self-assemblies with a self-regulation mechanism. *Nano Lett.* **2015**, *15* (4), 2213−9.
(29) Kundu, P. K.; Samanta, D.; Leizrowice, R.; Margulis, B.; Zhao, H.; Borner, M.; Udayabhaskararao, T.; Manna, D.; Klajn, R. Light-controlled self-assembly of non-photoresponsive nanoparticles. *Nat. Chem.* **2015**, *7* (8), 646−52.
(30) Leira-Iglesias, J.; Tassoni, A.; Adachi, T.; Stich, M.; Hermans, T. M. Oscillations, travelling fronts and patterns in a supramolecular system. *Nat. Nanotechnol.* **2018**, *13* (11), 1021−1027.
(31) Grötsch, R. K.; Angi, A.; Mideksa, Y. G.; Wanzke, C.; Tena-Solsona, M.; Feige, M. J.; Rieger, B.; Boekhoven, J. Dissipative Self-Assembly of Photoluminescent Silicon Nanocrystals. *Angew. Chem., Int. Ed.* **2018**, *57* (44), 14608−14612.
(32) van Ravensteijn, B. G. P.; Hendriksen, W. E.; Eelkema, R.; van Esch, J. H.; Kegel, W. K. Fuel-Mediated Transient Clustering of Colloidal Building Blocks. *J. Am. Chem. Soc.* **2017**, *139* (29), 9763−9766.
(33) Sawczyk, M.; Klajn, R. Out-of-Equilibrium Aggregates and Coatings during Seeded Growth of Metallic Nanoparticles. *J. Am. Chem. Soc.* **2017**, *139* (49), 17973−17978.
(34) Delamarche, E.; Michel, B.; Gerber, C.; Anselmetti, D.; Guentherodt, H. J.; Wolf, H.; Ringsdorf, H. Real-Space Observation of Nanoscale Molecular Domains in Self-Assembled Monolayers. *Langmuir* **1994**, *10* (9), 2869−2871.
(35) Totaro, K. A.; Liao, X.; Bhattacharya, K.; Finneman, J. I.; Sperry, J. B.; Massa, M. A.; Thorn, J.; Ho, S. V.; Pentelute, B. L. Systematic Investigation of EDC/sNHS-Mediated Bioconjugation Reactions for Carboxylated Peptide Substrates. *Bioconjugate Chem.* **2016**, *27* (4), 994−1004.
(36) Riess, B.; Wanzke, C.; Tena-Solsona, M.; Grötsch, R. K.; Maity, C.; Boekhoven, J. Dissipative assemblies that inhibit their deactivation. *Soft Matter* **2018**, *14* (23), 4852−4859.
(37) Klajn, R.; Bishop, K. J. M.; Grzybowski, B. A. Light-controlled self-assembly of reversible and irreversible nanoparticle supra-structures. *Proc. Natl. Acad. Sci. U. S. A.* **2007**, *104* (25), 10305.
(38) Song, G.; Li, J.; Yuan, Y.; Yao, L.; Gu, J.; Liu, Q.; Zhang, W.; Su, Y.; Zhang, D. Large-Area 3D Hierarchical Superstructures Assembled from Colloidal Nanoparticles. *Small* **2019**, *15* (18), 1805308.
(39) Heinen, L.; Walther, A. Temporal control of i-motif switch lifetimes for autonomous operation of transient DNA nanostructures. *Chemical Science* **2017**, *8* (5), 4100−4107.

DOI: 10.1021/jacs.9b02004
J. Am. Chem. Soc. 2019, 141, 9872−9878

Pathway dependence in the fuel-driven dissipative self-assembly of nanoparticles.

Raphael K. Grötsch[1], Caren Wanzke[1], Maximilian Speckbacher[2], Arzu Angi[3], Bernhard Rieger[3] and Job Boekhoven*[1,4]

1 Department of Chemistry, Technical University of Munich, Lichtenbergstraße 4, 85748 Garching (Germany).
2 Molecular Electronics, Department of Electrical and Computer Engineering, Technical University of Munich, Theresienstraße 90, 80333 Munich (Germany).

3 WACKER-Lehrstuhl für Makromolekulare Chemie, Technical University of Munich, Lichtenbergstraße 4, 85748 Garching (Germany) and Catalysis Research Center, Ernst-Otto-Fischer-Straße 1, 85748 Garching (Germany).

4 Institute for Advanced Study, Technical University of Munich, Lichtenbergstraße 4, 85748 Garching (Germany).

Supporting Information

Table of Content

1. Materials

Tetrachloroauric (III) acid trihydrate and trisodium-citrate dihydrate were purchased from Carl Roth. Iron oxide (II,II) magnetic nanoparticles solution with 10 nm in diameter and carboxylic acids as reactive groups on the surface (measured diameter by cryo-TEM = 15 nm; SPH-10 organic layer: Monolayer of oleic acid bound to the iron oxide and co-assembled on to the hydrophobic alkyl chain hydrolyzed polymaleic anhydride-alt-1-octadecene on the surface, for a detailed description of the synthesis see Nie et. al[1]), sodium 3-mercaptopropionic acid, N-Hydroxysuccinimide (NHS), 1-ethyl-3-(3-dimethylaminopropyl)carbodiimide (EDC), and 2-(N-morpholino) ethanesulfonic acid (MES) were purchased from Sigma-Aldrich. All chemicals were used without further purification. Water was obtained from a Millipore water purifier system.

2. Methods

Synthesis of gold NP

The synthesis followed a modified Turkevich protocol.[2] A tetrachloroauric (III) acid solution (HAuCl4 · 3 H2O, 5,8 mmol/l, 25 ml) was poured into refluxing water (250 ml). After the solution boiled again, a solution of sodium 3-mercaptopropionic acid (0,39 mmol/l, 25 ml) and trisodium citrate dihydrate (2,0 wt%) was injected. Heating for 1,5 hours yielded a pale red solution. The solution was slowly cooled to room temperature.

Determination of the concentration of surface bonded carboxylic acid groups

A fraction of the gold nanoparticles or iron oxide nanoparticles was dispersed in water and the pH was set to pH 10.5 by addition of NaOH (conc.). It was titrated against HCl (0.01 M) to determine the pKa and the number of carboxylates on the nanoparticle surface in the sample (See Figure SI1).

Average number of ligands per gold nanoparticle

Based on the TEM, we find the particles have a diameter of 3.5 nm (see below). That diameter corresponds to an average surface area per particle 38.5 nm^2. The surface area a thiol ligand occupies on a gold nanoparticle has been found to be 0.16 nm^2.[3]

From these numbers, we can calculate that on average each particles contains roughly 250 molecules of mercaptopropionic acid.

Reaction conditions for the chemical reaction cycle

Gold nanoparticles were dispersed in MES buffer (0.02 M, pH = 6.4) with 25 mM NHS to yield a 0.25 mM solution of carboxylates surface groups. Iron oxide nanoparticles were dispersed in MES buffer (0.2 M, pH = 6.5) with 20 mM NHS to yield a 5 mM solution of carboxylates surface groups.

In order to start the cycle, EDC was added from a high-concentration stock solution. The solution was pipetted a few times to induce mixing and allowed to stand without stirring. We noticed that stirring increased the tendency of the particles to precipitate in response to EDC.

Dynamic light scattering (DLS).

DLS measurements were performed using a Malvern Zetasizer Nano ZS with a laser wavelength of 633 nm. The nanoparticles solutions were measured using disposable cuvettes (PS). Each measurement consisted of 6 acquisitions with an acquisition time of 20 s.

Transmission electron microscopy (TEM)

Cryo-TEM imaging was performed on a Tecnai Spirit microscope (FEI/Thermo Fisher) operating at 120 kV or a Jeol JEM-1400 plus operating at 120 kV. The grids (C-Flat R1.2/1.3, 400 mesh, Cu or Quantifoil R2/2 on Cu-grid 400 mesh were used) were freshly glow-discharged for 90 seconds with 50 mA prior to use. Preparation of the grids was performed in a FEI/Thermo Fisher Vitrobot at 25 °C with the relative humidity set to 100%. The sample was incubated for 30 seconds on the grid, blotted for 2 seconds (blotting force set to -1) and then directly plunged into liquid ethane that was pre-cooled by liquid nitrogen. The cryo-TEM grids were transferred and stored in liquid nitrogen, and when needed, placed into a Gatan cryo-transfer-specimen holder to insert into the microscope. The specimen temperature was maintained at -170 °C during the data collection. The images were recorded in a low-dose mode on a CCD camera.

TEM imaging was performed on a Tecnai Spirit microscope (FEI/Thermo Fisher) operating at 120 kV. The Cu400 TEM grids were collodion-supported, carbon coated and freshly glow-discharged for 45 seconds with 35 mA prior to use. The sample was incubated for 45 seconds on the grid, blotted for 1 second and dried for 15 min. The images were recorded in a low-dose mode on a CCD camera.

Scanning electron microscopy (SEM)

SEM imaging was performed on a Zeiss NVision 40 operating at an electron high tension of 5 kV. Samples for SEM were prepared as described above. 24 hours after the EDC addition, the buffer was slowly exchanged with methanol. The clusters in methanol were transferred on a Si-wafer.

Fourier-transform infrared spectroscopy (FTIR).

First, the nanoparticles were isolated by acidifying the reaction solution at the indicated times during or before the cycle. Then the aggregated nanoparticles were centrifuged, the supernatant was removed and the NCs were redispersed in ethanol and acidified again. The centrifugation and dispersion steps were performed three times to obtain a pellet of precipitated particles. The pellet of nanoparticles were redispersed in 30 µL of ethanol and then dried on the measurement-crystal of the Bruker Vertex 70 FTIR using a platinum ATR from Bruker.

High pressure liquid chromatography (HPLC)

The kinetics of the chemical reaction networks were monitored over time by means of analytical HPLC (HPLC, Thermofisher Dionex Ultimate 3000, Hypersil Gold 250 x 4.8 mm, 25°C). A 400 µL sample was prepared as described above, filtered with a 25 mm syringe filter (200 nm polyethersulfone) and placed into a screw cap HPLC vial. Every 10 minutes, samples of the freshly filtered solutions were directly injected without further dilution, and all compounds involved were separated using a linear gradient water: ACN from 100:0 to 70:30. Calibration curves for EDC (λ= 220 nm) were performed in duplicate in order to quantify the compound over time.

Time-lapse photography. In a 1 ml HPLC-vial, 600 - 750 µL of NP solution were imaged with a high-definition camera. Time-lapse software was programmed to image the sample in intervals from 2 to 30 min.

3. Supporting Tables

Table SI1. Dynamic light scattering – Precursors of gold and iron oxide nanoparticles

Table SI1. The hydrodynamic diameter (d), derived count rate (DCR) and polydispersity index (PDI) data of gold nanoparticles (NP) and iron oxide nanoparticles as obtained by dynamic light scattering (DLS) in MES (2-(N-morpholino) ethanesulfonic acid) buffered aqueous solution.

	Gold NP			Iron oxide NP		
	d (nm)	DCR (mcps)	PDI (%)	d (nm)	DCR (mcps)	PDI (%)
	13.1	1.90	63	27.9	14.6	27
	12.7	1.91	56	18.4	14.7	26
	12.1	1.90	56	20.5	14.7	26
	12.2	1.89	63	35.2	14.8	27
	12.0	1.89	56	31.3	14.7	27
	13.3	1.90	55	19.6	14.6	28
	12.9	1.88	62	37.1	14.7	28
	12.7	1.89	56	28.6	14.7	27
	12.2	1.87	61	32.5	14.6	27
	13.2	1.89	55	30.6	14.7	29
Mean	12.6 ± 0.5	1.89 ± 0.01	58 ± 4	28 ± 7	14.7 ± 0.1	27 ± 1

Table SI2. DLS – Pathway complexity of gold and iron oxide nanoparticles

Table SI2. The hydrodynamic diameter (d), derived count rate (DCR) data of the gold and iron oxide nanoparticles obtained after the multiple addition of EDC to precursor solutions (3x 0.3 equivalents every 24 h, 2x 0.45 equivalents every 36 h, 1 x 0.9 equivalents for the gold nanoparticles; 5 x 0.4 equivalents every 48 h, 1x 2.0 equivalents for iron oxide nanoparticles). The samples were measured after 3 or 10 days, respectively.

	Gold NP		Iron oxide NP	
	d / nm	DCR / mcps	d / nm	DCR /mcps
Precursor	12.6 ± 0.5	1.89 ± 0.01	28 ± 7	14.7 ± 0.1
3x 0.3 equivalents; 3d	14 ± 1	2.39 ± 0.01		
2x 0.45 equivalents; 3d	15 ± 1	2.15 ± 0.01		
1x 0.9 equivalents; 3d	20 ± 4	0.53 ± 28		
5x 0.4 equivalents;10 d			27 ± 1	14.8 ± 0.1
1x 2.0 equivalents;10 d			-*	-*

* Due to the precipitation, insufficient nanoparticles were in the solution to measure reliable data for the iron oxide NP sample 10 days after the addition of 2.0 equivalents of EDC via DLS.

4. Supporting Figures

Figure SI1. Cryogenic-transmission electron microscopy of gold and iron oxide nanoparticle precursor

The cryogenic-transmission electron microscopy (cryo-TEM) micrographs of the precursor solutions are used for the size distribution analyses. Following the guidelines of Murphy and Buriak and Scott's rule for the bin width,[4,5] we measured 300 nanoparticles and depicted the results in a histogram.

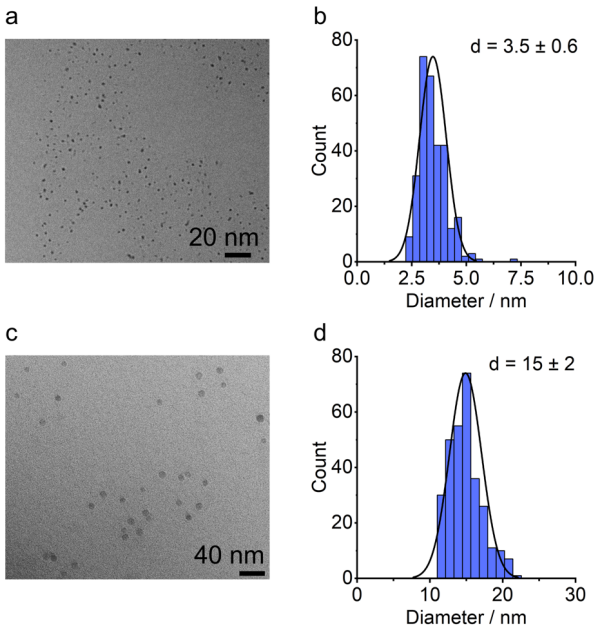

Figure SI1. Cryo-TEM micrographs of **a)** gold and **c)** iron oxide nanoparticles in MES buffer. Histogram of the **b)** gold and **c)** iron oxide nanoparticle diameters size distribution.

Figure SI2. Titration of gold and iron oxide nanoparticles

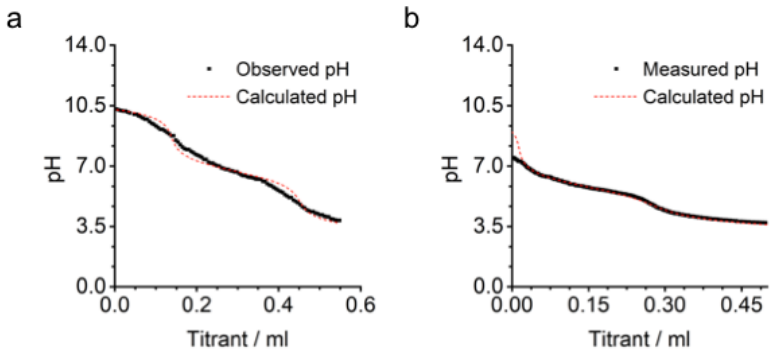

Figure SI2. Plot of the pH value as a function of the titrant (0.01 M HCl) for **a)** gold nanoparticles and **b)** iron oxide nanoparticles. The black curves indicate the measured values, whereas the red markers indicate the fitted values by Hyperquad 2008. Based on the fit, we calculated the pKa of the surface bound acids to **a)** 6.7 and **b)** 5.8.

Figure SI3. FTIR spectroscopy after addition of 0.3 equivalents of EDC to the gold nanoparticles

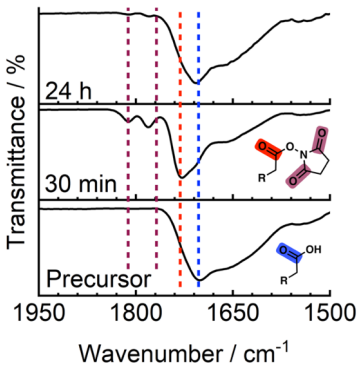

Figure SI3. Fourier-transformed Infrared (FTIR) diagram of the precursor, 30 minutes and 24 hours after the addition of 0.3 equivalents of EDC to a solution of the gold nanoparticles and NHS. Dashed lines from purple to blue mark the peaks for 1811, 1782, 1734 and 1705 cm^{-1}, respectively.

Figure SI4. DLS – diameter of gold nanoparticles

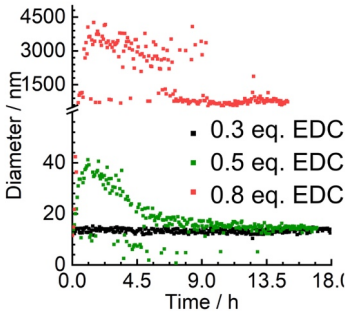

Figure SI4. Plot of the diameter of the particles and assemblies as a function of time as measured by DLS. The size changes were induced by the EDC addition.

Figure SI5. DLS – diameter of gold nanoparticles

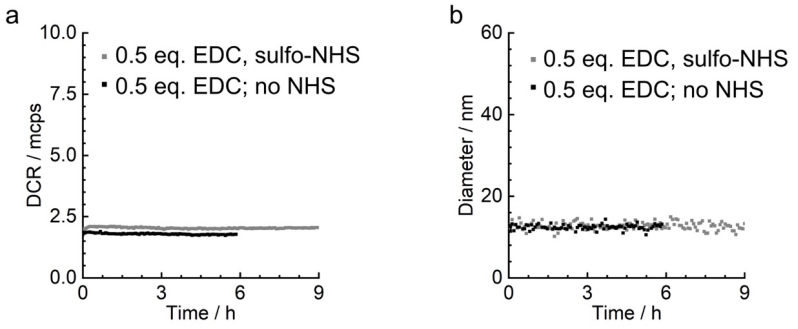

Figure SI5. Plot of **a)** the scattering rate and b**)** the diameter of the gold nanoparticles as a function of time measured by DLS. In the first experiment sulfo-NHs, which carries a negative charge, replaced NHS. In the second experiment no NHS at all was added.

Figure SI6. Supporting Scanning Electron Microscopy

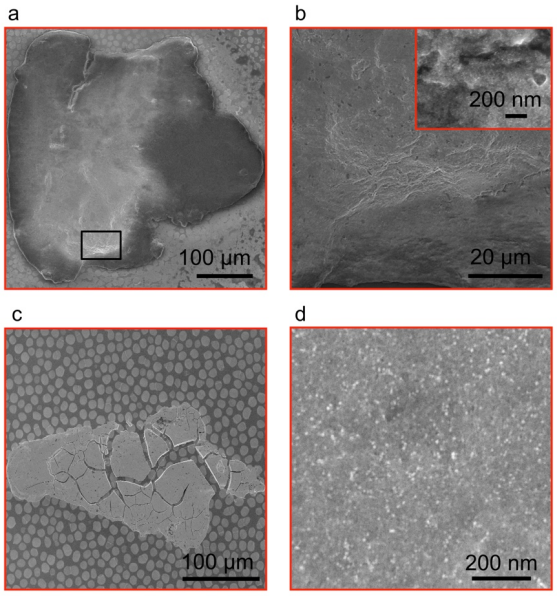

Figure SI6. **a - d**) Scanning electron microscopy (SEM) micrographs of clusters of the precipitate that formed after the addition of 0.8 equivalents of EDC.

Figure SI7. Time-lapsed photography for the addition of 0.8 equivalents of EDC to gold nanoparticles

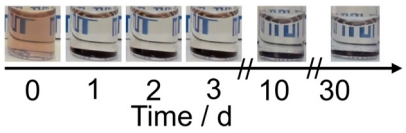

Figure SI7. Time-lapse photographs of a precursor solution after the addition of 0.8 equivalents of EDC.

Figure SI8. FTIR of 0.3, 0.5 and 0.8 equivalents of EDC addition to gold nanoparticles

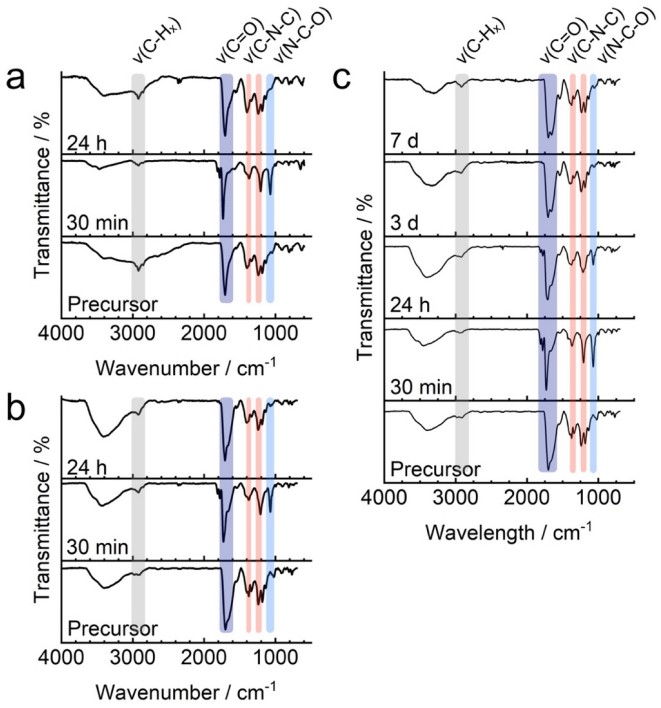

Figure SI8. FTIR spectra of gold nanoparticles. Three timepoints depicted for the addition of **a**) 0.5 **b**) 0.3 equivalents of EDC and five timepoints for the addition of **c)** 0.8 equivalents of EDC. Broad O-H band at 3000 – 3500 cm^{-1}, propionic acid functionalized gold nanoparticles alkyl peaks at 2900 cm^{-1} ($C-H_2$/$C-H_3$), Carbonyl peak at 1705 cm^{-1} (C=O). Additional NHS-ester peaks at 1814, 1784, and 1738 cm^{-1} appear, originating from the carbonyl groups of the NHS ester. In addition, characteristic signals of the succinimide cycle were observed at 1370 cm^{-1} νs(C–N–C), 1206 cm^{-1} νs(C –N–C), and 1065 cm^{-1} νs(N–C–O). c) FTIR spectrum 24 hours or 7 days after EDC addition. The signals of NCs with propionic acid surface groups have reappeared.

Figure SI9. DLS of 0.3 – 2 equivalents of EDC addition to gold nanoparticles

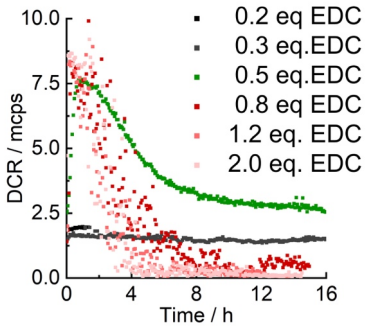

Figure SI9. DLS diagram of the diameter as a function of time. Size changes induced by EDC addition (black 0.2, grey 0.3, green 0.5 and red 0.8, 1.2, 2.0 equivalents of EDC).

Figure SI10. Supporting Transmission Electron Microscopy

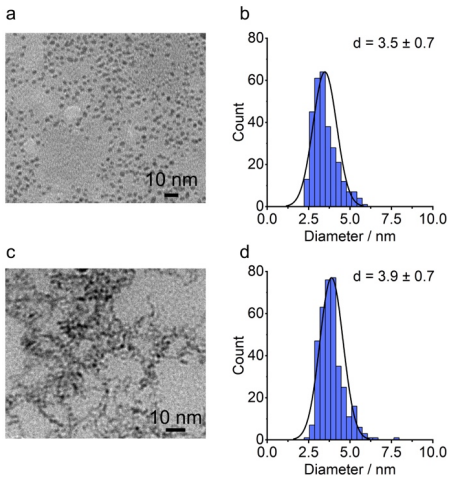

Figure SI10. TEM micrographs of gold nanoparticles **a)** in MES buffer and **c)** 24 h after the addition of 0.8 eq. of EDC. Histogram of gold nanoparticles diameter size distribution **b)** in MES buffer and **d)** 24 h after the addition of 0.8 eq. of EDC.

Figure SI11. FTIR data for the addition of 0.4 and 0.8 equivalents of EDC to the iron oxide nanoparticles

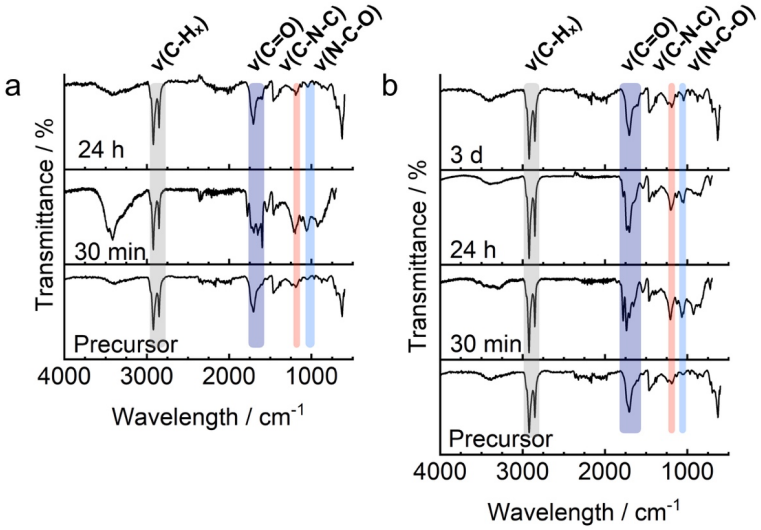

Figure SI11. FTIR spectra of the iron oxide nanoparticles at different time points in the reaction cycle. Three and four time points are shown for the addition of **a)** 0.4 **b)** 0.8 equivalents of EDC, respectively. Broad O-H band at 3000 – 3500 cm^{-1}, acid functionalized iron oxide nanoparticles alkyl peaks at 2900 cm^{-1} (C-H_2 and C-H_3), carbonyl peak at 1705 cm^{-1} (C=O). We observed additional NHS ester peaks appear, while the carbonyl peaks disappeared after EDC addition, at 1814, 1784, and 1738 cm^{-1} originating from the carbonyl groups of the NHS ester. In addition, characteristic signals of the succinimide cycle were observed at 1206 cm^{-1} νs(C –N–C), and 1065 cm^{-1} νs(N–C–O). FTIR spectrum 24 hours or 3 days after EDC addition. The signals of NCs with acid surface groups have reappeared.

5. References

(1) Duan, H.; Kuang, M.; Wang, X.; Wang, Y. A.; Mao, H.; Nie, S., Reexamining the Effects of Particle Size and Surface Chemistry on the Magnetic Properties of Iron Oxide Nanocrystals: New Insights into Spin Disorder and Proton Relaxivity. *The Journal of Physical Chemistry C* **2008,** *112* (22), 8127-8131.
(2) Yonezawa, T.; Kunitake, T., Practical preparation of anionic mercapto ligand-stabilized gold nanoparticles and their immobilization. *Colloids and Surfaces a-Physicochemical and Engineering Aspects* **1999,** *149* (1-3), 193-199.
(3) Hinterwirth, H.; Kappel, S.; Waitz, T.; Prohaska, T.; Lindner, W.; Lämmerhofer, M., Quantifying Thiol Ligand Density of Self-Assembled Monolayers on Gold Nanoparticles by Inductively Coupled Plasma–Mass Spectrometry. *ACS Nano* **2013,** *7* (2), 1129-1136.
(4) Murphy, C. J.; Buriak, J. M., Best Practices for the Reporting of Colloidal Inorganic Nanomaterials. *Chemistry of Materials* **2015,** *27* (14), 4911-4913.
(5) Anderson, S. L.; Luber, E. J.; Olsen, B. C.; Buriak, J. M., Substance over Subjectivity: Moving beyond the Histogram. *Chemistry of Materials* **2016,** *28* (17), 5973-5975.

Dissipative Self-Assembly of Photoluminescent Silicon Nanocrystals

Abstract

The above described and characterized dissipative self-assembly of nanoparticles is transferred from the gold and iron oxide nanoparticles to silicon nanocrystals. The silicon nanocrystals offer excellent biocompatibility, and the above-described reaction cycle operates under physiological conditions. The focus of this publication is the demonstration of the unique properties of the nanomaterial that culminate in a potential spatio-temporal controlled drug delivery platform. The nanoparticles are functionalized with a hexanoic acid surface and serve as the precursor in the reaction cycle. This surface is negatively charged; therefore, the particles are well soluble in a buffered solution at pH 6.5. The chemical reaction cycle transforms the carboxylates on the surface into N-Hydroxysuccinimide esters rendering the particles uncharged and less soluble. The uncharged particles form agglomerates with tens of micrometers in size. Over time, as the esters are intrinsically unstable in water, the particles regain their charges and start to repel one and another again and finally disassemble after hours. With the spatio-temporal control of the material, a time-delayed nanoparticle uptake in mammalian cells was achieved. This demonstrated that with a biologically active substance on the surface, as a next step, this system could be used for time-controlled drug delivery.

This work has been published:

Title:	Dissipative Self-Assembly of Photoluminescent Silicon Nanocrystals
Authors:	Raphael K. Grötsch, Arzu Angı, Yonatan G. Mideksa, Caren Wanzke, Dr. Marta Tena-Solsona, Prof. Dr. Matthias J. Feige, Prof. Dr. Bernhard Rieger, Prof. Dr. Job Boekhoven
First published:	24. July 2018
Journal:	Angewandte Chemie International Edition, **2018**, *57*, 14608 – 14612.
Publisher:	Wiley-VCH
DOI:	10.1002/anie.201807937
Angew. Chem.:	10.1002/ange.201807937

Reprinted with permission of John Wiley and Sons; License Number: 4575950376854.

This section states the individual work of each author in the publication above. R. K. Grötsch designed all experiments and conducted analytical experiments with the nanoparticles and conducted the fluorescent microscopy studies of the nanoparticle uptake experiments. A. Angı synthesized the nanoparticles and helped with the cell experiments and the IR measurements. C. Wanzke imaged with a cryogenic transmission electron microscope the nanoparticles. Y. G. Mideksa seeded the cells and wrote the cells methods part in the SI. R. K. Grötsch, A. Angı, and J. Boekhoven wrote the manuscript. The work was performed under the supervision and guidance of M. J. Feige, B. Rieger, and J. Boekhoven.

GDCh Communications Angewandte International Edition Chemie

Self-Assembly

International Edition: DOI: 10.1002/anie.201807937
German Edition: DOI: 10.1002/ange.201807937

Dissipative Self-Assembly of Photoluminescent Silicon Nanocrystals

*Raphael K. Grötsch[+], Arzu Angı[+], Yonatan G. Mideksa, Caren Wanzke, Marta Tena-Solsona, Matthias J. Feige, Bernhard Rieger, and Job Boekhoven**

Abstract: *Solutions of silicon nanocrystals (SiNCs) are used in a diverse range of applications because of their tunable photoluminescence, biocompatibility, and the abundance of Si. In dissipative supramolecular materials, self-assembly of molecules or nanoparticles is driven by a chemical reaction network that irreversible consumes fuel. The properties of the emerging structures are controlled by the kinetics of the underlying chemical reaction network. Herein, we demonstrate the dissipative self-assembly of photoluminescent SiNCs driven by a chemical fuel. A chemical reaction induces self-assembly of the water-soluble SiNCs. However, the assemblies are transient, and when the chemical reaction network runs out of fuel, the SiNCs disassemble. The lifetime of the assemblies is controlled by the amount of fuel added. As an application of the transient supramolecular material, we demonstrate that the platform can be used to control the delayed uptake of the nanocrystals by mammalian cells.*

Silicon nanocrystals (SiNCs) have garnered significant attention[1] for their unique properties, which include size-dependent photoluminescence,[2] low-toxicity,[3] and biocompatibility.[4,5] Moreover, the elemental abundance of silicon favors the applications in sensors,[6] LEDs,[7] solar cells,[8] and bio-imaging.[9,10] The surface chemistry of SiNCs plays a critical role in these applications because it can alter the nanocrystal's natural properties.[11] Thus properties such as cytotoxicity,[12] photoluminescent emission quantum yield,[13] or emission wavelength,[14] can be tuned through functionalization of the SiNCs' surface. Strategies to modify the surface chemistry of the SiNCs rely on the formation of stable, covalent bonds. The static nature of these bonds does not allow for dynamic material properties that evolve or that adapt to environmental changes.

In contrast, dissipative supramolecular materials are intrinsically dynamic, and their function can be controlled over space and time.[15] For these materials, the self-assembly of molecules is coupled to (photo)chemical reaction networks. In these chemical reaction networks, an activation reaction activates a precursor, which enables the precursor to undergo self-assembly. The reaction can only occur at the expense of a source of energy, typically a photon or a chemical fuel, and is irreversible. That is, the activation reaction "burns" a source of energy to activate a precursor for self-assembly. The activated product can then self-assemble to form a supramolecular material. However, the product is metastable and spontaneously deactivates into the original precursor via the deactivation reaction. The dissipative self-assembly implies that the supramolecular material is dynamic and forms in response to energy. Man-made examples of dissipative self-assembly include the ATP-fueled assembly of amphiphiles into temporary nanoreactors,[16] the formation of transient self-healing hydrogels driven by the hydrolysis of methylating agents,[17] the carbodiimide-driven formation of colloids that can deliver hydrophobic agents,[18] among others.[19,20] In the context of the dissipative assembly of nanoparticles, researchers have described the light-driven self-assembly of silver and gold nanoparticles into self-erasing inks,[21] and the dynamic pH controlled clustering of gold nanoparticles.[22] Another example used methylating agents to drive the assembly of colloids.[20]

Herein, we describe a new chemical reaction network that drives the dissipative self-assembly of SiNCs (Figure 1a). We show that the emerging clusters of SiNCs change size predictably over time and that the emerging materials can be re-used in multiple cycles. We use the evolving size of the SiNC clusters to delay the uptake of the SiNCs by mammalian fibroblasts-like cells. The combined experiments open a platform that could deliver therapeutics with a delayed and regulated uptake kinetics.

We functionalized SiNCs with 5-hexenoic acid to make them water-soluble (the precursor in Figure 1a). An acid-titration experiment revealed their pKa to be approximately 6.9 (Figure SI1 in the Supporting Information). The SiNCs were dissolved in a buffer at a final surface-bound carboxylic acid concentration of 5 mM. The buffer we used was a 200 mM 2-(*N*-morpholino)ethanesulfonic acid (MES) buffer with 100 mM *N*-hydroxysuccinimide (NHS) at pH 6.5 in water. At this pH, more than half of the carboxylic groups on the SiNCs were deprotonated. As a result, the electrostatic

[*] R. K. Grötsch,[+] C. Wanzke, Dr. M. Tena-Solsona, Prof. Dr. J. Boekhoven
Department of Chemistry, Technische Universität München
Lichtenbergstrasse 4, 85748 Garching (Germany)
E-mail: job.boekhoven@tum.de
A. Angı,[+] Prof. Dr. B. Rieger
WACKER-Lehrstuhl für Makromolekulare Chemie
Technische Universität München
Lichtenbergstrasse 4, 85748 Garching (Germany)
and
Catalysis Research Center
Ernst-Otto-Fischer-Strasse 1, 85748 Garching (Germany)
Y. G. Mideksa, Prof. Dr. M. J. Feige
Center for Integrated Protein Science at the Department of Chemistry, Technische Universität München
Lichtenbergstrasse 4, 85748 Garching (Germany)
R. K. Grötsch,[+] Y. G. Mideksa, C. Wanzke, Dr. M. Tena-Solsona, Prof. Dr. M. J. Feige, Prof. Dr. J. Boekhoven
Institute for Advanced Study, Technische Universität München
Lichtenbergstrasse 2a, 85748 Garching (Germany)
[+] These authors contributed equally to this work.
Supporting information and the ORCID identification number(s) for the author(s) of this article can be found under: https://doi.org/10.1002/anie.201807937.

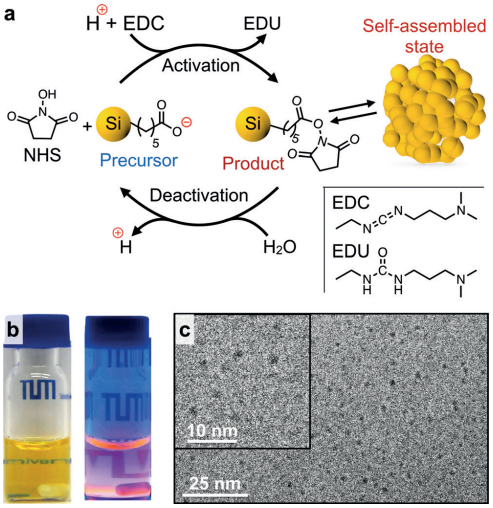

Figure 1. a) Schematic representation of the chemical reaction network. Carboxylate surface groups on the SiNCs react with EDC and NHS to form a transient NHS ester. The loss of surface charges induced the temporary self-assembly of SiNCs. b) Photographs of a solution of the precursor in MES buffer under visible (left) and UV (365 nm, right) light. c) Cryo-TEM images of the precursor solution.

stabilization achieved by these charges made the SiNCs well-soluble in the buffer. Indeed, dissolution of the SiNCs in the buffer yielded a yellow transparent colloidal solution (Figure 1b). Under UV irradiation the yellow solution emitted red light, strongly indicating that the SiNCs maintained their intrinsic photoluminescence. The emission was further verified in a spectrophotometer, which showed a photoluminescent emission maximum at 681 nm when irradiated with 365 nm UV light (Figure SI2). We determined the hydrodynamic diameter of the SiNCs to be (5.5 ± 1.1) nm by dynamic light scattering (Table SI1). Cryogenic transmission electron microscopy (cryo-TEM) corroborated the successful synthesis of the SiNCs and their homogeneous dissolution. From the micrographs, we determined their diameter to be (3.6 ± 0.5) nm (Figure 1c, Figure SI3b). Finally, UV/Vis spectra of the SiNCs showed absorption at wavelengths shorter than 400 nm (Figure SI4).

The carboxylic acid functionalized SiNCs served as the precursors in the chemical reaction network we introduce herein (Figure 1a). In the activation reaction, the carboxylate groups on the SiNC surface were converted into the corresponding NHS-esters by the irreversible consumption of 1-ethyl-3-(3-dimethylaminopropyl) carbodiimide (EDC). In the deactivation reaction, the NHS esters hydrolyzed back to their initial carboxylate state. The cycle could only operate for as long as EDC was present because the activation irreversibly consumed EDC. Moreover, the loss of electrostatic stabilization upon the conversion of the precursor induced assembly of the SiNCs into clusters. Taken together, the irreversible consumption of EDC induced the transient assembly of the SiNCs.

We studied the kinetics of the aforementioned reaction network. The SiNCs solution was fueled with a 7 mM solution of EDC, and the evolution of the concentration of EDC was monitored via high-pressure liquid chromatography (HPLC, Figure 2a). The concentration of EDC decreased to less than

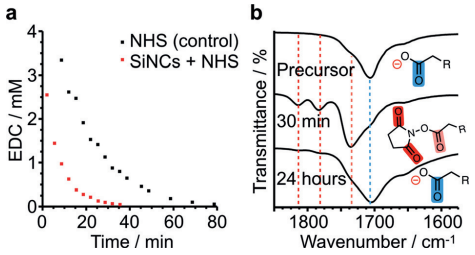

Figure 2. a) The EDC concentration as a function of time. The red markers correspond to the addition of 7 mM EDC to a solution of SiNCs in MES-buffer (200 mM) and NHS (100 mM), the black markers show the same experiment without the SiNCs as a control. b) FTIR spectra of the precursor SiNCs; 30 min and 24 h after addition of 7 mM EDC. Dashed lines from left to right: 1814, 1784, 1738, 1706 cm^{-1} (R=-$(CH_2)_4$-SiNC).

3 mM within the first minute, after which it further decayed exponentially. No substantial amount of EDC was detected after 35 min. The initial rapid decay was likely a result of a reaction of EDC with NHS.[23] This hypothesis was further corroborated by a similar rapid decrease in the EDC concentration in a control experiment without the SiNCs (Figure 2a). The EDC decay rate was higher in the presence of SiNCs than in the control reaction. This accelerated decay served as a good indicator of the reaction between the carbodiimide and the carboxylate surface groups of SiNCs.

We monitored the surface groups of the SiNCs in response to EDC by Fourier-transform infrared (FTIR) spectroscopy (Figure 2b, see Figure SI5 for full spectra). Before the addition of EDC, the spectrum of the SiNCs showed a C=O band at 1706 cm^{-1}, which corresponds to the carboxylic acid groups.[24,25] Upon the addition of 7 mM EDC, the peak at 1706 cm^{-1} weakened to a small shoulder and three new peaks arose at 1814 cm^{-1}, 1784 cm^{-1} and 1738 cm^{-1}, which correspond to ν_s(C=O, NHS ester), ν_s(C=O NHS imide), and to ν_s(C=O NHS-imide), respectively. Importantly, 24 h after the addition of EDC, the NHS-ester peaks mostly disappeared, whereas the carboxylic acid peak at 1706 cm^{-1} recovered (Figure 2b). This result is a good indication that the NHS ester is transient and hydrolyzes to the original precursor. The combined results demonstrate that the carboxylic acids on the SiNCs' surface were transiently converted into their corresponding NHS ester at the expense of EDC.

The initially yellow clear solution became turbid upon the addition of EDC. Moreover, the turbid solution became transparent over the course of hours, pointing to an assembly and disassembly process of the SiNCs. We used time-lapse photography to follow the changes in turbidity over time

(Figure 3a). An EDC concentration of at least 6.5 mM was required to induce a noticeable increase in turbidity. When the EDC concentration was 6.5 mM, the increase in turbidity persisted for more than 4 h. Moreover, we observed that, with increasing EDC concentration, the samples remained turbid longer. For example, with 12.5 mM EDC, which corresponds to a 2.5-fold excess of fuel over the surface-bound carboxylates, the turbidity persisted approximately 17 h. When a 20-fold excess of fuel was added, the solutions remained turbid for longer than 2 days (Figure SI6).

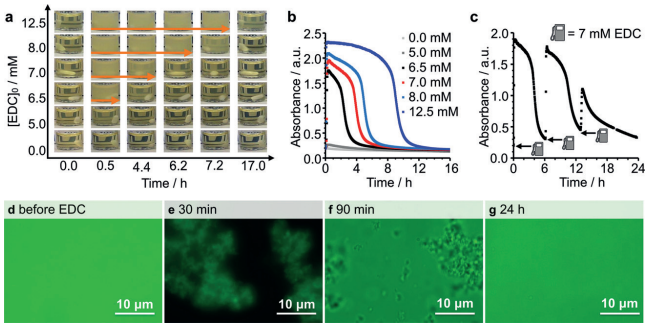

Figure 3. a) Photographs of SiNC solutions with different initial EDC concentrations over time; each column represents a different time point. b) Absorbance at 500 nm over time as a quantification of turbidity induced by the addition of different concentrations of EDC (0.0, 5.0, 6.5, 7.0, 8.0, and 12.5 mM). c) Three consecutive additions of 7 mM EDC to the same SiNC solution. Turbidity was monitored via UV/Vis spectrophotometry (absorbance at 500 nm). d)–g) Fluorescent micrographs acquired before (d) and 30 min (e), 90 min (f) and, 24 h (g) after the addition of 7 mM EDC. The intrinsic fluorescence of the SiNCs was measured.

We quantified the transient turbidity by measuring the absorbance at 500 nm in a UV/Vis spectrophotometer. When EDC was added to the samples, the turbidity increased in the first 30 min to a maximum, then decreased to its original level (Figure 3b). To quantify the lifetime of the increased turbidity, we set an arbitrary absorbance threshold at 0.27 absorbance units. Above this threshold, the sample was considered turbid; below the threshold, it was considered transparent. We found that the lifetime of the turbidity increased linearly with increasing EDC concentration between 6.5 to 12.5 mM (Figure SI7).

We used the intrinsic photoluminescence of the SiNCs in combination with fluorescence microscopy to study the nature of the turbidity in greater detail. Before the addition of EDC, fluorescence microscopy revealed a homogeneous fluorescent solution without evidence of assemblies. In contrast, 30 min after the addition of 7 mM EDC, we observed bright fluorescent clusters of tens of micrometers, whereas the surrounding solution showed no fluorescent emission (Figure 3d,e). From the lack of fluorescence in the surrounding solution, we concluded that most of the SiNCs had been incorporated into the clusters. After 90 min, we observed smaller clusters and the surrounding solution started to emit light again (Figure 3f). These observations point toward the disassembly of the clusters into the SiNCs. After 24 h, we observed a homogeneous photoluminescent solution, reminiscent of the solution shown in the micrographs collected before the addition of EDC (Figure 3g). Moreover, cryo-TEM images of SiNC solutions after the reaction cycle revealed a size distribution of SiNCs ($d = 3.6 \pm 0.7$ nm) similar to that before the addition of EDC (Figure 1c, Figure SI3). Unfortunately, cryo-TEM on the samples during the cycle proved challenging probably because of the size of the clusters. Instead, we used confocal microscopy and found clusters of the particles of tens of microns in all three dimensions (Figure SI8).

The possibility of inducing transient assembly of the SiNCs in consecutive cycles was also tested. The first reaction cycle was initiated with the addition of 7 mM EDC. After the solution had lost its turbidity, the next cycle was started by addition of a new batch of 7 mM EDC. The turbidity measurements showed that the cycles could be repeated as many as three times. However, the third cycle showed signs of fatigue, that is, the maximum turbidity the sample reached was only 59% of the value compared to the first cycle. All three cycles showed lifetimes of approximately 6.2 h (Figure 3c). Two possible reasons could explain the fatigue: The reaction between the carboxylic acids and EDC can yield N-acylurea[24] as a stable side product that cannot revert to the precursor state, or the waste product 1-[3-(Dimethylamino)propyl]-3-ethylurea (EDU) interferes with the assembly process. We only observed minimal amounts of the N-acylurea by FTIR after three cycles (Figure SI9). In contrast, we found that addition of EDU affected the cycle drastically, which would explain the fatigue after three cycles (Figure SI10). Performing the experiment under argon to limit SiNC oxidation did not change the fatigue (Figure SI11).

From these experiments, we conclude that EDC induced the transient assembly of the SiNCs into clusters. The lifetime of these assemblies is tunable, and the assembly–disassembly process can be repeated several times. Encouraged by these results, we began exploring the properties of these SiNC assemblies for potential future biomedical applications. Recent work has shown that SiNCs are readily taken up by cells, likely through passive diffusion of the relatively small particles.[4,9] We wondered whether we could delay such passive uptake by the transient clustering of the SiNCs. Our rationale was that the particle clusters might not be taken up because of their large size. However, as the clusters disassemble the SiNC precursors become available for passive uptake (Figure 4a).

To test the delayed uptake of the particles, we confirmed the uptake of SiNCs by a mammalian cell line by incubating COS-7 fibroblast-like cells with the SiNCs for 9 h. In these experiments, the SiNCs were added to cells in a mixture of phosphate-buffered saline (PBS, see Supporting Information

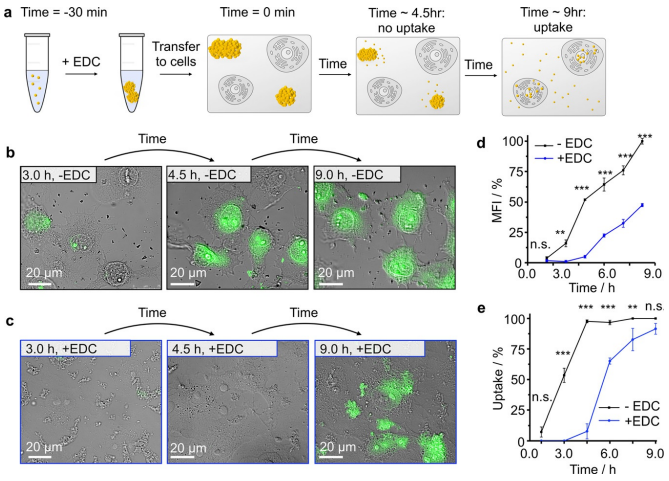

Figure 4. a) Schematic overview of the experiment. For the control experiment, no EDC is added (-EDC). The delayed uptake (4.5 h) depends on the amount of EDC added to the particles in the first step. b),c) Fluorescence micrographs of cells incubated with the SiNC solution without EDC (b) and with EDC (c) for 3.0, 4.5, and 9.0 h. d) Mean fluorescence intensity of the nucleus as a function of time for cells incubated with SiNCs and SiNCs + 9 mM EDC. The highest uptake after 9 hours is set to 100%. e) Percentage of cells that have taken up a significant amount of SiNCs, that is, with a nucleus intensity above the threshold level of 50 a.u. Error bars depict ± standard deviation of the mean for $n \geq 3$, and two-way analysis of variance (ANOVA) with a Bonferroni post-test is used between the with and without EDC at each time point. ** and *** represent a P value <0.01 and <0.001, respectively.

for details) and MES. At intervals of 1.5 h, the cells were thoroughly washed and tested for uptake of the SiNCs by live-cell fluorescence microscopy. We measured the mean fluorescence intensity of the nuclei of the cells. After the first 1.5 h, the mean fluorescence intensity was similar to an untreated control sample. In contrast, after 3.0 h, the cells were brighter than those of an untreated control sample (Figure 4b, Figures SI13, 14). Moreover, the fluorescence intensity continued to increase with increasing incubation time (Figure 4d). To quantify the fraction of cells that had taken up SiNCs, we set a threshold value fluorescence intensity (see Supporting Information). Above this value, we considered the cell had taken up a significant amount of SiNCs (Figure 4e). The quantification of the uptake followed a similar trend over time: In the first 1.5 h, only a small fraction of the cells had taken up particles, whereas all cells had taken up after 4.5 h.

In a second experiment, the uptake of the SiNCs fueled by EDC was tested. The assembly of SiNCs was initiated by the addition of 9 mM EDC. After 30 min, the turbid solution with the SiNC clusters was added to the cells. It should be clarified that after 30 min, most of the EDC had reacted (Figure 2) and the cells were thus only exposed to minimal amounts of EDC. The lack of EDC after 30 min also implies that the growth of the clusters is likely minimal and the material properties are dominated by the hydrolysis and disassembly kinetics. We determined the lifetime of the metastable clusters to be 6 h in the presence of cell media but in the absence of cells (Figure SI15). In the first hours of the experiment with cells, we did not observe an increase in the mean fluorescence intensity of the cells (Figure 4d). Only after 6 h, did we start to see an increase in fluorescence of the nuclei compared to the control without SiNCs. Moreover, the fraction of cells that had taken up SiNCs had also drastically increased compared to earlier time points (Figure 4e). The mean fluorescence of the cells continued to increase with time, and the number of cells that had taken up SiNCs reached greater than 90% after 9.0 h of incubation. We also confirmed the viability of the COS-7 cells in the conditions we used in these experiments (Figure SI12). Finally, we confirmed the observed differences in uptake profile were not a result of the EDU, the waste product of the reaction cycle (Figure SI16).

When we compare the evolution of the uptake by the cells of the SiNC treated or not treated with EDC, a picture emerges that confirms our hypothesis. It becomes apparent that the cells cannot take up the clusters, because after 4.5 h there was an insignificant uptake when EDC was added, whereas all cells had taken up SiNCs in the experiment without EDC. This comparison points to inhibition of uptake when the SiNCs are assembled into a cluster. After 6.0 h, that is, when the clusters are disassembling (Figure SI15), we observed uptake of the SiNCs, which points to a mechanism in which the cells take up the SiNCs that have been released from the clusters. Because of the dissipative chemistry, this release of the SiNCs is delayed and so is the uptake. The fraction of cells with particles reaches similar levels as the experiments without EDC only after 9.0 h.

In conclusion, we demonstrated the dissipative self-assembly of SiNCs driven by EDC as chemical fuel. The SiNCs assembled into clusters of tens of micrometers. By varying the amount of EDC, we tuned the lifetime of SiNC clusters between 4 h and 2 days. A biological application of the transient character of SiNC clusters was explored. We showed that the time of uptake of the SiNCs by COS-7 cells could be delayed with our dissipative self-assembled system. We foresee that such dissipative supramolecular materials, whether SiNCs or other types of nanoparticles, could be used in the future to engineer materials that can delay the delivery of therapeutics into or inside cells.

Acknowledgements

This work was supported by the Technische Universität München—Institute for Advanced Study, funded by the

German Excellence Initiative and the European Union Seventh Framework Programme under grant agreement N° 291763 and the International Research Training Group ATUMS (IRTG 2022). A.A. acknowledges funding from Studienstiftung des deutschen Volkes. M.T.-S. acknowledges the European Union's Horizon 2020 Research and Innovation program for the Marie Sklodowska Curie Fellowship under grant agreement N° 747007.

Conflict of interest

The authors declare no conflict of interest.

Keywords: cellular uptake · chemical reaction network · dissipative self-assembly · non-equilibrium self-assembly · silicon nanocrystals

How to cite: *Angew. Chem. Int. Ed.* **2018**, *57*, 14608–14612
Angew. Chem. **2018**, *130*, 14817–14822

[1] M. Dasog, J. Kehrle, B. Rieger, J. G. C. Veinot, *Angew. Chem. Int. Ed.* **2016**, *55*, 2322; *Angew. Chem.* **2016**, *128*, 2366.
[2] a) C. M. Hessel, D. Reid, M. G. Panthani, M. R. Rasch, B. W. Goodfellow, J. Wei, H. Fujii, V. Akhavan, B. A. Korgel, *Chem. Mater.* **2012**, *24*, 393; b) O. Wolf, M. Dasog, Z. Yang, I. Balberg, J. G. C. Veinot, O. Millo, *Nano Lett.* **2013**, *13*, 2516.
[3] a) Q. Wang, Y. Bao, X. Zhang, P. R. Coxon, U. A. Jayasooriya, Y. Chao, *Adv. Healthcare Mater.* **2012**, *1*, 189; b) X. Cheng, S. B. Lowe, P. J. Reece, J. J. Gooding, *Chem. Soc. Rev.* **2014**, *43*, 2680; c) N. H. Alsharif, C. E. M. Berger, S. S. Varanasi, Y. Chao, B. R. Horrocks, H. K. Datta, *Small* **2009**, *5*, 221.
[4] F. Erogbogbo, K.-T. Yong, I. Roy, G. Xu, P. N. Prasad, M. T. Swihart, *ACS Nano* **2008**, *2*, 873.
[5] H. Nishimura, K. Ritchie, R. S. Kasai, M. Goto, N. Morone, H. Sugimura, K. Tanaka, I. Sase, A. Yoshimura, Y. Nakano et al., *J. Cell. Biol.* **2013**, *202*, 967.
[6] C. M. Gonzalez, M. Iqbal, M. Dasog, D. G. Piercey, R. Lockwood, T. M. Klapötke, J. G. C. Veinot, *Nanoscale* **2014**, *6*, 2608.
[7] a) F. Maier-Flaig, J. Rinck, M. Stephan, T. Bocksrocker, M. Bruns, C. Kübel, A. K. Powell, G. A. Ozin, U. Lemmer, *Nano Lett.* **2013**, *13*, 475; b) A. Angı, M. T. Loch, R. Sinelnikov, J. Veinot, M. Becherer, P. Lugli, B. Rieger, *Nanoscale* **2018**, *10*, 10337.
[8] M. Dutta, L. Thirugnanam, P. van Trinh, N. Fukata, *ACS Nano* **2015**, *9*, 6891.
[9] J. H. Warner, A. Hoshino, K. Yamamoto, R. D. Tilley, *Angew. Chem. Int. Ed.* **2005**, *44*, 4550; *Angew. Chem.* **2005**, *117*, 4626.
[10] B. F. P. McVey, R. D. Tilley, *Acc. Chem. Res.* **2014**, *47*, 3045.
[11] K. Dohnalová, T. Gregorkiewicz, K. Kůsová, *J. Phys. Condens. Matter* **2014**, *26*, 173201.
[12] a) S. Bhattacharjee, I. M. C. M. Rietjens, M. P. Singh, T. M. Atkins, T. K. Purkait, Z. Xu, S. Regli, A. Shukaliak, R. J. Clark, B. S. Mitchell et al., *Nanoscale* **2013**, *5*, 4870; b) A. Shiohara, S. Hanada, S. Prabakar, K. Fujioka, T. H. Lim, K. Yamamoto, P. T. Northcote, R. D. Tilley, *J. Am. Chem. Soc.* **2010**, *132*, 248.
[13] M. A. Islam, M. H. Mobarok, R. Sinelnikov, T. K. Purkait, J. G. C. Veinot, *Langmuir* **2017**, *33*, 8766.
[14] a) A. Angi, R. Sinelnikov, A. Meldrum, J. G. C. Veinot, I. Balberg, D. Azulay, O. Millo, B. Rieger, *Nanoscale* **2016**, *8*, 7849; b) M. Dasog, G. B. De los Reyes, L. V. Titova, F. A. Hegmann, J. G. C. Veinot, *ACS Nano* **2014**, *8*, 9636.
[15] a) S. A. P. van Rossum, M. Tena-Solsona, J. H. van Esch, R. Eelkema, J. Boekhoven, *Chem. Soc. Rev.* **2017**, *46*, 5519; b) A. Sorrenti, J. Leira-Iglesias, A. J. Markvoort, T. F. A. de Greef, T. M. Hermans, *Chem. Soc. Rev.* **2017**, *46*, 5476; c) R. Merindol, A. Walther, *Chem. Soc. Rev.* **2017**, *46*, 5588; d) F. Della Sala, S. Neri, S. Maiti, J. L.-Y. Chen, L. J. Prins, *Curr. Opin. Biotechnol.* **2017**, *46*, 27; e) R. Grötsch, J. Boekhoven, *Unique properties of Supramolecular Biomaterials through Non-equilibrium Self-assembly in Self-assembling Biomaterials*, Woodhead Publishing, Oxford, **2018**; f) B. Rieß, J. Boekhoven, *ChemNanoMat* **2018**, https://doi.org/10.1002/cnma.201800169.
[16] S. Maiti, I. Fortunati, C. Ferrante, P. Scrimin, L. J. Prins, *Nat. Chem.* **2016**, *8*, 725.
[17] a) J. Boekhoven, W. E. Hendriksen, G. J. M. Koper, R. Eelkema, J. H. van Esch, *Science* **2015**, *349*, 1075; b) J. Boekhoven, A. M. Brizard, K. N. K. Kowlgi, G. J. M. Koper, R. Eelkema, J. H. van Esch, *Angew. Chem. Int. Ed.* **2010**, *49*, 4825; *Angew. Chem.* **2010**, *122*, 4935.
[18] a) M. Tena-Solsona, B. Rieß, R. K. Grötsch, F. C. Löhrer, C. Wanzke, B. Käsdorf, A. R. Bausch, P. Müller-Buschbaum, O. Lieleg, J. Boekhoven, *Nat. Commun.* **2017**, *8*, 15895; b) B. Rieß, C. Wanzke, M. Tena-Solsona, R. K. Grötsch, C. Maity, J. Boekhoven, *Soft Matter* **2018**, *14*, 4852.
[19] a) A. Sorrenti, J. Leira-Iglesias, A. Sato, T. M. Hermans, *Nat. Commun.* **2017**, *8*, 15899; b) C. G. Pappas, I. R. Sasselli, R. V. Ulijn, *Angew. Chem. Int. Ed.* **2015**, *54*, 8119; *Angew. Chem.* **2015**, *127*, 8237.
[20] B. G. P. van Ravensteijn, W. E. Hendriksen, R. Eelkema, J. H. van Esch, W. K. Kegel, *J. Am. Chem. Soc.* **2017**, *139*, 9763.
[21] R. Klajn, P. J. Wesson, K. J. M. Bishop, B. A. Grzybowski, *Angew. Chem. Int. Ed.* **2009**, *48*, 7035; *Angew. Chem.* **2009**, *121*, 7169.
[22] L. Heinen, A. Walther, *Chem. Sci.* **2017**, *8*, 4100.
[23] K. A. Totaro, X. Liao, K. Bhattacharya, J. I. Finneman, J. B. Sperry, M. A. Massa, J. Thorn, S. V. Ho, B. L. Pentelute, *Bioconjugate Chem.* **2016**, *27*, 994.
[24] S. Sam, L. Touahir, J. Salvador Andresa, P. Allongue, J.-N. Chazalviel, A. C. Gouget-Laemmel, C. Henry de Villeneuve, A. Moraillon, F. Ozanam, N. Gabouze et al., *Langmuir* **2010**, *26*, 809.
[25] C. Wang, Q. Yan, H.-B. Liu, X.-H. Zhou, S.-J. Xiao, *Langmuir* **2011**, *27*, 12058.

Manuscript received: July 11, 2018
Accepted manuscript online: July 24, 2018
Version of record online: August 27, 2018

Angewandte Chemie
Eine Zeitschrift der Gesellschaft Deutscher Chemiker

Supporting Information

Dissipative Self-Assembly of Photoluminescent Silicon Nanocrystals

*Raphael K. Grötsch[+], Arzu Angı[+], Yonatan G. Mideksa, Caren Wanzke, Marta Tena-Solsona, Matthias J. Feige, Bernhard Rieger, and Job Boekhoven**

anie_201807937_sm_miscellaneous_information.pdf

Author Contributions

M.F. Supervision: Supporting
B.R. Supervision: Supporting.

Supporting Information

Table of Content

1. Supplementary Tables

Dynamic light scattering

Table SI1. Hydrodynamic diameter and PDI data of SiNCs obtained by dynamic light scattering in MES buffered aqueous solution.

	Hydrodynamic Diameter (nm)	PDI (%)
	5.0	30
	6.2	22
	5.7	24
	4.0	24
	5.9	30
	6.0	29
	4.2	24
	7.7	26
	5.2	28
	5.0	40
Mean Diameter	5.5 ± 1.1	
Mean PDI		28 ± 5

2. Supplementary Figures

Titration of SiNC

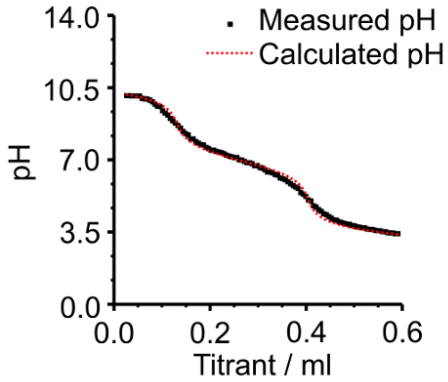

Figure SI1. *Plot of the pH value as a function of the titrant (0.01 M HCl) of a SiNC batch. The black curve indicates the measured values, whereas the red markers the fitted values by HySS 2009. Based on the fit, we calculated a pKa of 6.9 of the surface bound carboxylates. The total amount of acid in the sample was calculated to be 2.6 µmoles.*

Photoluminescence Spectroscopy

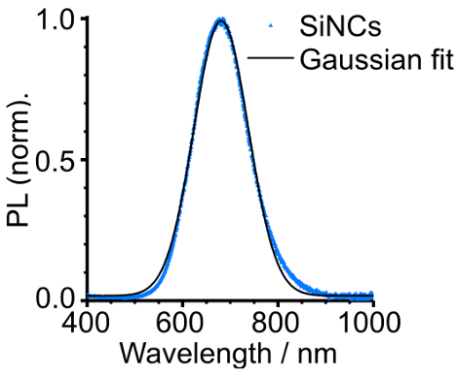

model	Gauss
equation	$y=y_0 + (A/(w*sqrt(pi/2)))*$ $exp(-2*((x-xc)/w)^2)$
y_0	0.0179 ± 0.0008
x_c	680.8 ± 0.1
w	114.6 ± 0.3
A	139.9 ± 0.4
R^2(COD)	0.997

Figure SI2. *Photoluminescence (PL) of SiNCs in MES buffered aqueous solution (100 mM NHS, Ex. 365 nm).*

Cryogenic-Transmission Electron Microscopy (cryo-TEM)

The analysis of the cryo-TEM pictures and the resulting data depiction followed the guidelines of Murphy and Buriak.[1] We measured 300 particles for the size distribution and applied Scott's rule for the bin width in histograms of a normal distribution.

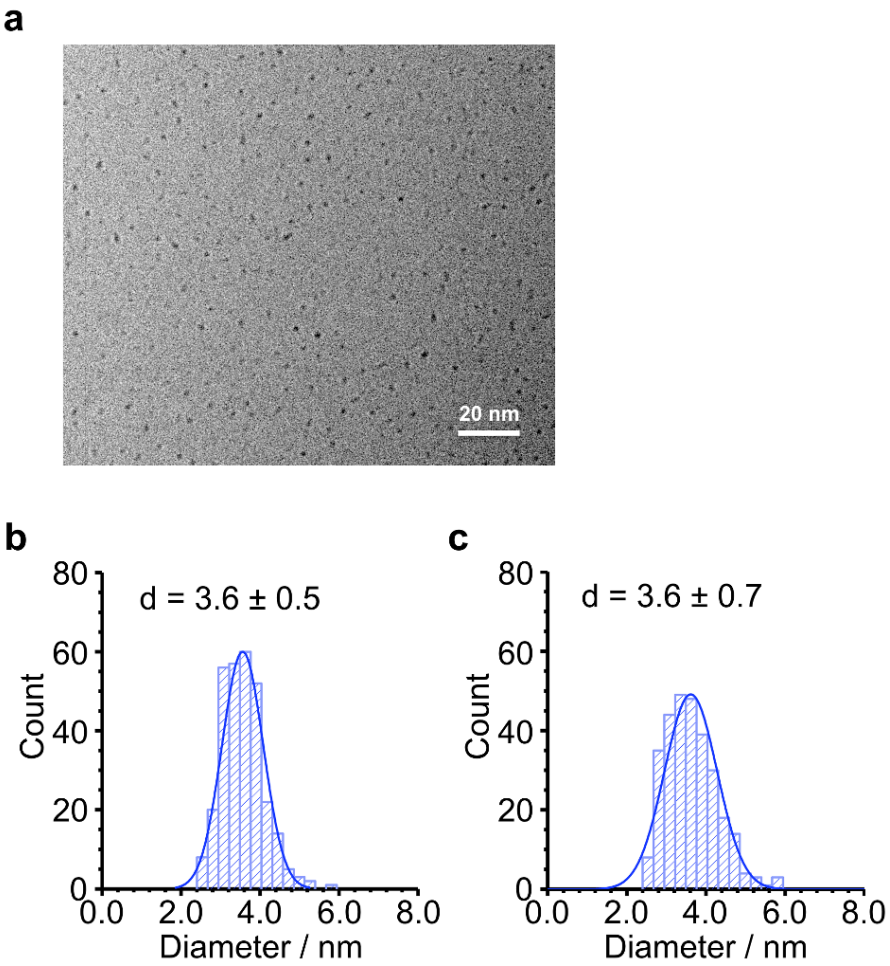

Figure SI3. a) Cryo-TEM micrographs of SiNCs 24 h after EDC addition. **b,c)** Histograms of the distribution of the SiNC diameters before (b) and 24 h after (c) 7 mM EDC addition.

UV/VIS Spectroscopy

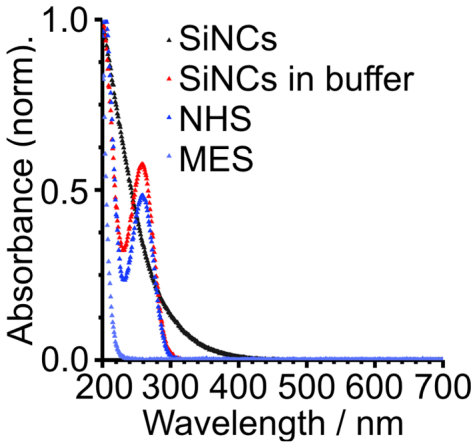

Figure SI4. *UV-Vis spectra of SiNCs in water (pH = 6.5), SiNCs in buffer (MES, NHS, pH = 6.5), NHS, and MES. Absorbance is normalized to 1 at 200 nm.*

Fourier-transform Infrared Spectroscopy

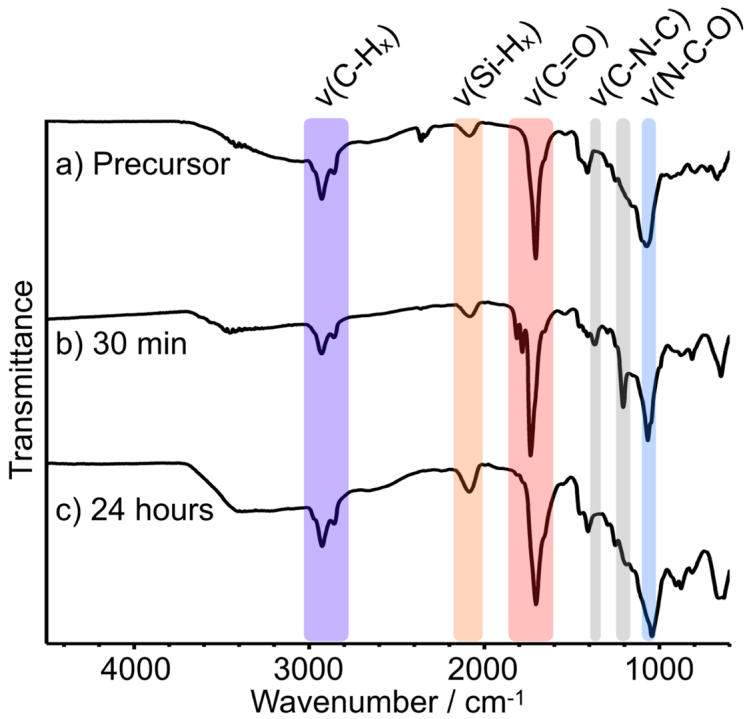

Figure SI5. FTIR spectra of SiNCs. a) FTIR spectrum of the precursor solution before addition of EDC. Si–H_x peaks at ~2100, 906 and 660 cm^{-1}; broad Si−O band centered at 1050 cm^{-1},hexanoic acid functionalized SiNCs alkyl peaks between 2825-2955 cm^{-1} (C-H_2 and C-H_3), at 1450 cm-1 and 1408 cm^{-1} (C-H δ-deformation); Carbonyl peak at 1705 cm^{-1} (C=O) together with a broad O-H peak between 3500-2500 cm^{-1}. b) FTIR spectrum of the precursor solution 30 min after 7 mM EDC addition. The NHS ester additional peaks appear at 1814, 1784, and 1738 cm^{-1} originating from the carbonyl groups of the NHS ester. In addition, characteristic signals of the succinimide cycle were observed at 1370 cm^{-1} νs(C–N–C), 1206 cm^{-1} νs(C –N–C), and 1065 cm^{-1} νs(N–C–O). c) FTIR spectrum 24 hours after EDC addition. The signals of SiNCs with hexanoic acid surface groups have reappeared.

Time-lapse Photography

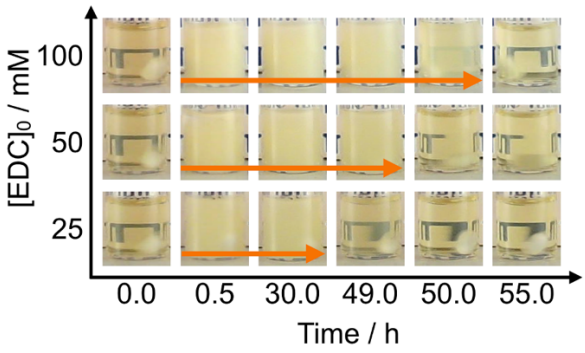

***Figure SI6**. Photographs at different points in time during a dissipative cycle initiated by addition of 25, 50 and 100 mM of EDC to SiNC solutions.*

Lifetime against concentration EDC

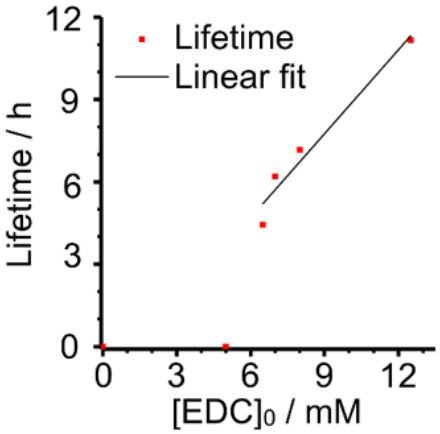

Figure SI7. *The lifetime of the transient SiNC clusters as a function of the initial EDC concentration added. The lifetime was determined by UV-Vis spectroscopy.*

Confocal fluorescent microscopy

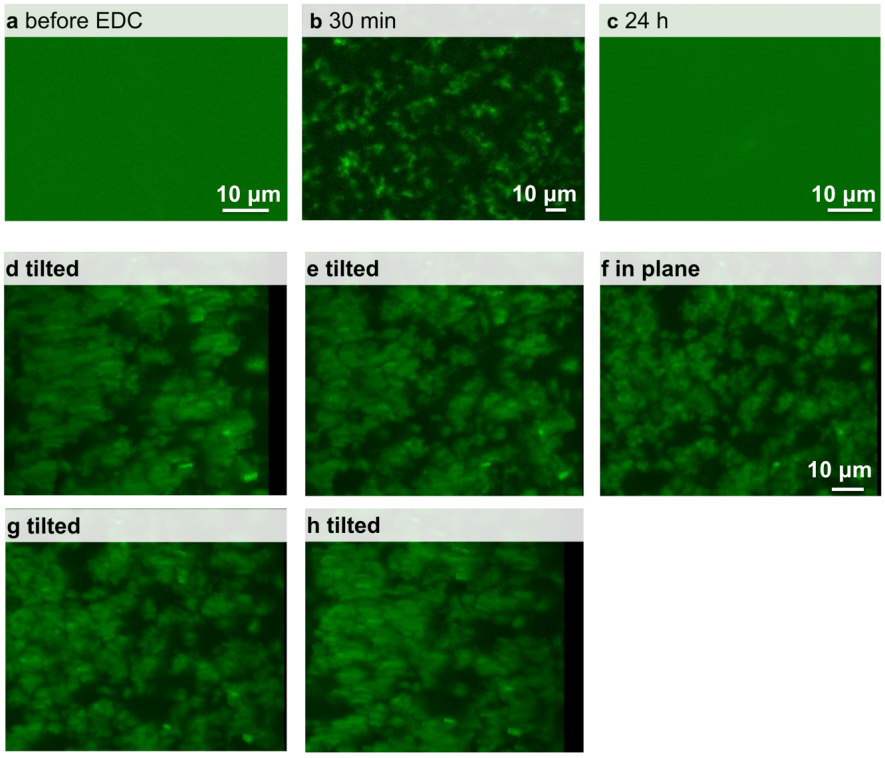

Figure SI8. *Fluorescent micrographs acquired before (a) and 30 min (b) and, 24 h (c) after the addition of 7 mM EDC. d-h) 3D projection of the clusters.*

Fourier-transform Infrared Spectroscopy

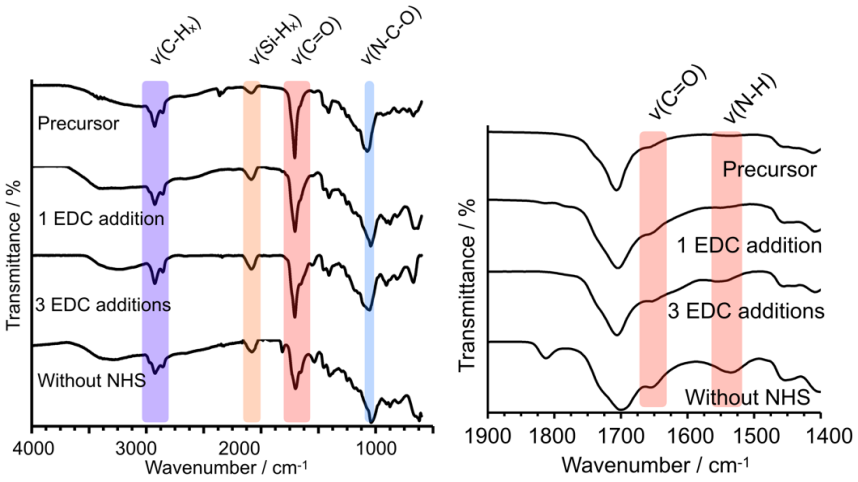

Figure SI9. FTIR spectra of SiNC Precursor. **Precursor**) FTIR spectrum of the precursor solution before addition of EDC. Si–H_x peaks at ~2100, 906 and 660 cm^{-1}; broad Si−O band centered at 1050 cm^{-1},hexanoic acid functionalized SiNCs alkyl peaks between 2825-2955 cm^{-1} (C-H_2 and C-H_3), at 1450 cm-1 and 1408 cm^{-1} (C-H δ-deformation); Carbonyl peak at 1705 cm^{-1} (C=O) together with a broad O-H peak between 3500-2500 cm^{-1}. **1 EDC addition)** FTIR spectrum of the precursor solution 24 h after 7 mM EDC addition. Slightly broadened peaks compared to the precursor spectra. **3 EDC additions)** FTIR spectrum of the precursor solution 24 h after the third 7 mM EDC addition. Slightly broadened peaks compared to the precursor spectra and new peaks at 1650 and 1535 cm-1, which we assigned to ν(amide C=O) and ν(amide N-H) of N-Acylurea. **Without NHS**) FTIR spectrum 24 hours after EDC addition to Precursor solution without NHS. In the spectra without NHS we see peaks at 1650 and 1535 cm^{-1}, which we assigned to ν(amide C=O) and ν(amide N-H) of N-Acylurea. Another peak appears at 1815 cm^{-1}, which we assigned to anhydride formation. In addition, the carbonyl peak at 1705 cm^{-1} is also measured.

UV/Vis as a function of time with different EDU concentrations

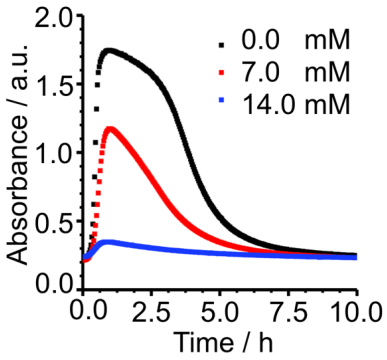

Figure SI10. *UV-Vis absorbance at 500 nm as a function of time as a quantification of turbidity induced by addition of 7 mM EDC. The turbidity is a measure for cluster formation. The different EDU concentrations (black 0.0 mM, red 7.0 and blue 14.0 mM) represent the waste accumulation for the cycle experiment after 0, 1 and 2 cycles. EDU decreases the UV absorbance drastically with increasing concentration.*

UV/Vis as a function of time under Argon atmosphere

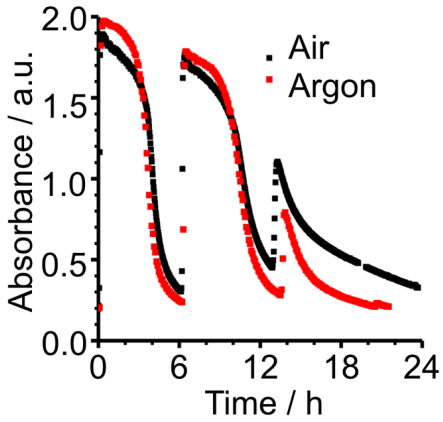

Figure SI11. *UV-Vis absorbance at 500 nm as a function of time as a quantification of turbidity induced by addition of 7 mM EDC. The turbidity is a measure for cluster formation. The argon sample was synthesized and measured under argon atmosphere with degassed solvents. The air sample was synthesized as described.*

Viability assay

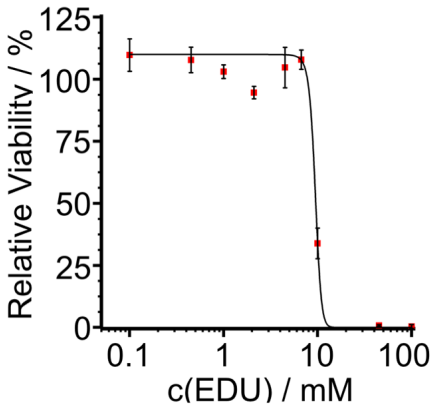

Figure SI12. *Viability assay. Relative viability against EDU concentration. After 6.7 mM EDU viability starts to decrease.* IC_{50}*: 9.5 mM EDU.*

Microscopy of COS-7cells

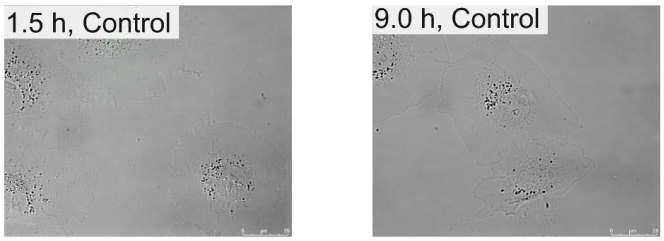

Figure SI13: Fluorescence microscopy images of COS-7 cells. *Cells incubated without SiNCs as a control experiment.*

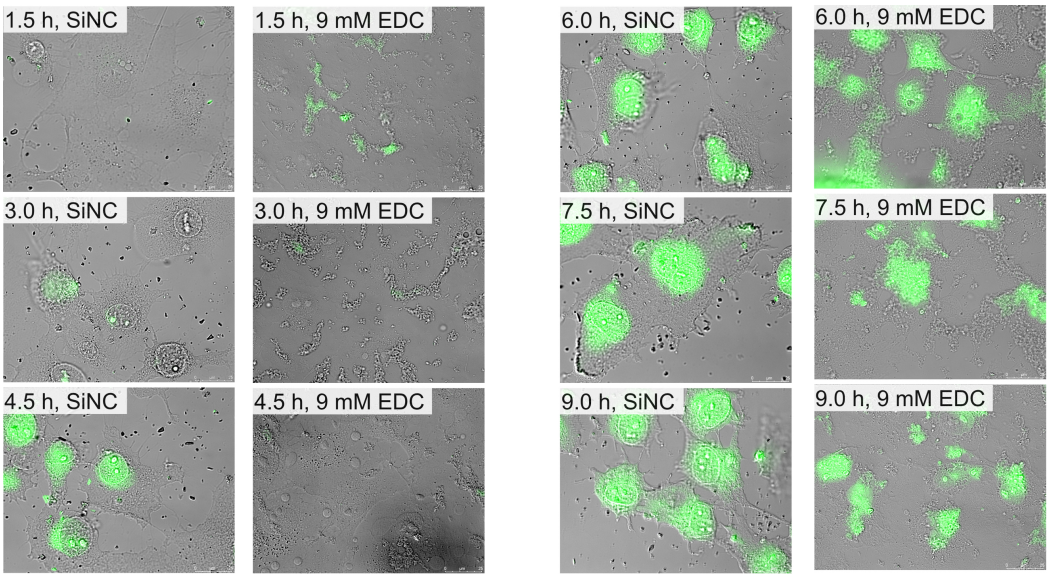

Figure SI14: Fluorescence microscopy images of COS-7 cells. *Cells incubated with SiNCs. In the left column, cells are incubated with untreated SiNCs. In the right column cells are incubated with SiNCs that have been treated with 9 mM EDC for 30 minutes prior to the incubation.*

We chose a threshold of 50 a.u. above the background for the mean fluorescent intensity to count cells with a significant uptake of SiNCs.

UV/Vis as a function of time under cell-experiment conditions

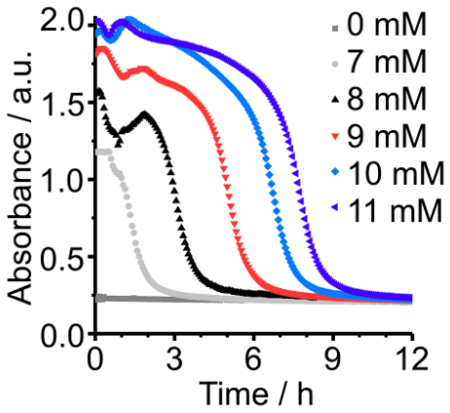

Figure SI15. *UV-Vis absorbance at 500 nm as a function of time as a quantification of turbidity induced by addition of different concentrations of EDC (0.0, 7.0, 8.0, 9.0, 10.0, and 11.0). The turbidity is a measure for cluster formation. The conditions were used to mimic the cell experiment's environment, i.e., EDC was added 30 min prior to mixing the SiNC cluster solution with PBS in a 1 to 1 ration. The experiment was carried out at 25°C for the first 30 min and then continued at 37°C.*

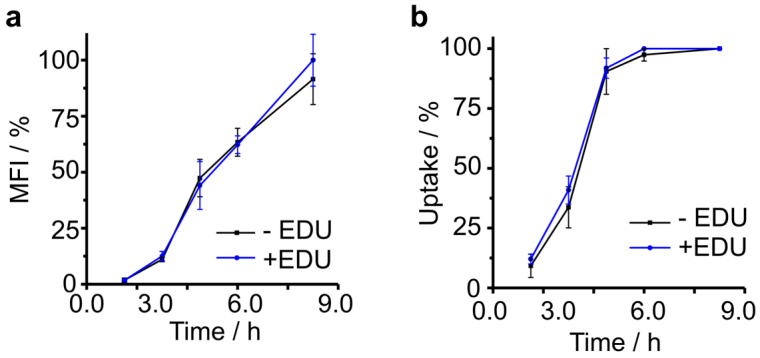

Figure SI16. *a) Mean fluorescence intensity of the nucleus as a function of time for cells incubated with SiNCs and SiNCs + 9 mM EDU. The highest uptake after 9 hours is set to 100%. b) Percentage of cells that have taken up a significant amount of SiNCs, i.e., with a nucleus intensity above the threshold level of 10 a.u.. Both experiments show that the presence of EDU does not change the uptake of the SiNCs*

3. Materials

5-Hexenoic acid, hydrofluoric acid (HF, 48%) ethanol, N-Hydroxysuccinimide (NHS), 1-ethyl-3-(3-dimethylaminopropyl)carbodiimide (EDC), and 2-(N-morpholino) ethanesulfonic acid (MES) were purchased from Sigma-Aldrich. Azobisisobutyronitrile (AIBN) was bought from Fluka. All chemicals were used without further purification, except for NHS which was recrystallized twice. Dry toluene was obtained from a MBraun SPS 800 solvent purification system with Argon 5.0 as the operating gas. Water was obtained from a Milli-Q water purifier system.

4. Experimental Details

Synthesis of the SiNC/SiO_2 composite. The SiNCs were prepared via thermolysis of polymeric hydrogen silsesquioxane (HSQ) which was synthesized following a literature procedure.[2] After the synthesis, HSQ (7 g) was weighed in a quartz reaction boat, placed in to a Nabertherm RD 30/200/11 furnace with quartz working tube and heated from room temperature to a peak processing temperature of 1100 °C with 18 °C/min heating rate in a slightly reducing atmosphere (5% H_2 /95% N_2). The sample was kept at 1100 °C for 1 h. A brown solid was obtained and ground into a fine powder using a mortar and pestle. Then the composite was shaken in ethanol for 24h with high-purity silica beads using a WAB Turbula mixer for further grinding. The resulting SiNC/SiO_2 composite was dried in vacuo and stored in glass vials.

Liberation of Hydride-Terminated SiNCs. Free-standing, hydride terminated SiNCs with an average diameter of 3.6 ± 0.5 nm are obtained upon etching this composite with an ethanol:water:HF (1:1:1) mixture and final extraction into toluene. 150 mg of the SiNC/SiO_2 composite was weighed into an ethylene-tetrafluoroethylene beaker equipped with a Teflon-coated stir bar. Ethanol (1.5 mL) and water (1.5 mL) were then

added, and stirred to form a brown suspension. 1.5 ml 49% HF aqueous solution was added, and the composite is etched for 30 min. Hydride-terminated SiNCs were subsequently extracted from the aqueous layer into ca. 15 mL of toluene by multiple (i.e., 3 × 5 mL) extractions. The SiNC-toluene suspension was centrifuged in an ETFE-centrifuge tube at 9000 rpm for 5 mins. To remove any residual water/ethanol, extracted particles dispersed in 5 ml dry toluene and centrifuged once more.

Surface Functionalization of SiNCs. Freshly etched, hydride-terminated SiNCs were dispersed in 0.5 ml dry toluene and transferred to a Schlenk flask equipped with a stirring bar. 10 mg AIBN was dissolved in 0.5 ml dry toluene and added to the reaction flask. Upon addition of 0.3 ml 5-hexenoic acid, the reaction mixture was degassed 3 times via freeze-thaw cycles. The flask was filled with argon and placed in a 70°C oil bath for 16 hours. At the end of the reaction, functionalized SiNCs were purified by 3 centrifugation/dispersion cycles with ethanol and pentane. Resulting SiNCs were readily dispersible in ethanol.

Determination of the concentration of surface bonded –COOH groups. A fraction of 10% of the obtained SiNCs was dispersed in water and the pH was set to pH 10.5 by addition of concentration NaOH. It was titrated against HCl (0.01 M) to determine the pKa and the number of carboxylates on the SiNC surface in the sample (See Fig. S1l).

Reaction conditions for the dynamic self-assembly. The remaining fraction (90%) of the SiNCs were dispersed in degassed MES Buffer (0.2 M, pH = 6.5) with 100mM NHS to yield a 5 mM solution of carboxylates surface groups. SiNC solution referred from here on has this concentration.

All measurements and reactions were performed with freshly synthesized SiNCs and under stirring with 600 rpm if not stated otherwise.

Photoluminescence spectroscopy (PL). PL spectra were measured with an AVA-Spec 2048 from Avantes using a Prizmatix (LED Current controller) as the light source.

Dynamic light scattering (DLS). DLS measurements were performed using a Zetasizer Nano ZS from Malvern with a laser wavelength of 633 nm. The SiNCs solutions were measured using a disposable cuvettes (PS). Each measurement consisted of 6 acquisitions with an acquisition time of 20 s.

Cryogenic-Transmission Electron Microscopy (cryo-TEM). Samples for cryo-TEM were prepared as described above. Shortly before imaging, the samples were diluted a 20-fold to decrease the density of SiNCs in the micrographs. Cryo-TEM imaging was performed on a Tecnai Spirit microscope (FEI/Thermo Fisher) operating at 120 kV. The grids (C-Flat R1.2/1.3, 400 mesh, Cu) were freshly glow-discharged for 90 seconds prior to use. Preparation of the grids was performed in a FEI/Thermo Fisher Vitrobot at 25 °C with the relative humidity set to 100%. The sample was incubated for 30 seconds on the grid, blotted for 2 seconds (blotting force set to -1) and then directly plunged into liquid ethane that was pre-cooled by liquid nitrogen. The cryo-TEM grids were transferred and stored in liquid nitrogen, and when needed, placed into a Gatan cryo-transfer-specimen holder to insert into the microscope. The specimen temperature was maintained at -170 °C during the data collection. The images were recorded in a low-dose mode on a CCD camera.

Fourier-Transform Infrared Spectroscopy (FTIR). FTIR spectra were obtained of the SiNCs. First, the SiNCs were isolated by acidifying the reaction solution of the samples before or after a cycle. To isolate the SiNCs during a cycle, EDC was added and the SiNCs were allowed to aggregate into their clusters. Then the aggregated SiNCs were centrifuged, the supernatant was removed and the SiNCs were redispersed in

ethanol/pentane. The centrifugation and dispersion steps were performed three times to obtain a pellet of precipitated particles. The SiNCs were then dried on the measurement-crystal of the Bruker Vertex 70 FTIR using a Platinum ATR from Bruker.

In order to obtain information on the interaction of the surface –COOH groups with EDC and NHS, two control experiments were performed. First, only NHS was added to the SiNCs solution. In the absence of the EDC, NHS does not react with the surface as the spectrum of SiNCs only exhibit signals correlated to hexanoic acid groups. In the second experiment, only EDC was added to the SiNCs solution. In this case, first O-Acylurea forms as the –OH of the carboxyl group adds to EDC. O-Acylurea then can yield 2 different products: i.) An anhydride due to a reaction with a neighboring carboxyl group ii.) N-acylurea via intramolecular rearrangement of an acyl functionality. The bands in FTIR spectrum may relate to the formation of N-acylurea, as the signals at 1727 cm^{-1} νs(C=O, N-acylurea), 1647 cm^{-1} νs(C=O, peptide (amide I) and 1531 cm^{-1} (peptide N-H bending (amide II). At the same time, the peak at 1815 cm-1 can also be assigned to anhydride C=O. Both possible products seem to coexist at the surface of SiNCs.

High Pressure Liquid Chromatography (HPLC). The kinetics of the chemical reaction networks were monitored over time by means of analytical HPLC (HPLC, Thermofisher Dionex Ultimate 3000, Hypersil Gold 250 x 4.8 mm, 25°C). A 400 µL sample was prepared as described above, filtered with a 25 mm syringe filter (w/200 µm polyethersulfone) and placed into a screw cap HPLC vial. Every 10 minutes, samples of the freshly filtered solutions were directly injected without further dilution, and all compounds involved were separated using a linear gradient water: ACN from 100:0 to 70:30. Calibration curves for EDC (λ= 220 nm) were performed in duplicate in order to quantify the compound over time.

Time-lapse photography. In a 1 ml HPLC vial 600 µl of SiNC solution were stirred in front of a camera. A picture was taken every two minutes. EDC (1 M water solution) was added according to the concentrations of each sample.

Fluorescent Microscopy. For each time (before EDC, 30, 90 min, 24h), a fresh aliquot (20 µL) of the sample was placed on a microscope slide, covered with a 12 mm diameter coverslip and imaged within the first minute. A Leica DMi8 inverted wide-field microscope (100x objective) with DIC and GFP filters (Exc. BP 470/40; Em. BP 525/50; DC 495) was used.

Confocal Fluorescence Microscopy. Confocal fluorescence microscopy was performed on a Leica SP5 confocal microscope using a 63x oil immersion objective. Samples were prepared as described above for the fluorescent microscopy. 20 µL (timepoints: before EDC, 30 min, 24 h after) of the sample was deposited in a circle of grease on the glass slide and covered with a 12 mm diameter coverslip. Samples were excited with 543 nm laser and imaged at 580-700 nm.

Cell-based experiments. COS-7 cells were grown in Dulbecco's Modified Eagle's Medium (DMEM) containing L-Ala-L-Gln (AQmedia, Sigma-Aldrich) supplemented with 10% (v/v) fetal bovine serum (Biochrom) and a 1% (v/v) antibiotic-antimycotic solution (25 µg/ml amphotenicin B, 10 mg/ml streptomycin, and 10,000 units of penicillin) at 37°C in a humidified 5% CO_2 atmosphere. 24 hours prior to the experiments, cells were seeded at 80% confluency on a µ-slide 8-well plate (ibidi) and further incubated at 37°C with 5% CO_2. Either SiNC or self-assembled SiNC (i.e. SiNC incubated with 9mM EDC for 30 minutes) were added to cells in a 1:1 dilution with DPBS and incubated for the indicated time points. Cells treated with only DPBS served as a control to estimate viability, stress levels and the background fluorescence. After addition of SiNC, cells were washed twice with DMEM without phenol red (Gibco) containing 10% (v/v) fetal

bovine serum, 2 mM Glutamax™ (Gibco), pyruvate and 25 mM HEPES. Cells were then monitored on a 37°C-heated stage using a Leica DMi8 inverted wide-field microscope (63x objective) with DIC and GFP filters ($\lambda_{exc.}$ BP 470/40; $\lambda_{em.}$ BP 525/50; DC 495).

To quantify the cell uptake of the SiNCs the mean fluorescence of the nucleus was measured. A threshold values of 50 a.u. above the background fluorescence of the control cells was chosen as significant uptake. Above this value, the cell was consider to have taken up SiNCs.

Viability Assay. COS-7 cells were incubated at 37°C with 5% CO_2 for 9 hours in PBS/MES-buffer with different EDU concentrations (0.0, 0.1, 0.45, 1.0, 2.1, 4.5, 6.7, 10.0, 45.0, 100.0 mM). The media was exchanged for DMEM with 0.5 mg/ml Methylthiazolyldiphenyl-tetrazolium bromide (MTT) as a yellow dye that is converted into a water insoluble formazan. After three hours the media is exchanged for DMSO to liberate the formazan crystals and 30 min later the absorbance is measured at 570 nm (background (630 nm) subtracted).

5. References

[1] a) S. L. Anderson, E. J. Luber, B. C. Olsen, J. M. Buriak, Chem. Mater. **2016**, 28, 5973; b) C. J. Murphy, J. M. Buriak, Chem. Mater. **2015**, 27, 4911.

[2] H. M. Bank, M. E. Cifuentes, E. M. Theresa, United States Pat. **1991**, 5.

Silicon Nanocrystals as a Reusable Sensing Agent

Abstract.

Encouraged by the dissipative self-assembly of silicon nanocrystals described in Chapter 5,[51] we explored nanocrystals for further applications. Aromatic molecules quench the photoluminescence of silicon nanocrystals *via* an electron- or energy-transfer mechanism,[52] with a quenching efficiency that differs with different aromatics.[53,54] The relation between molecular structure and quenching efficiency opens the door to use silicon nanocrystals as a sensing agent, *i.e.,* a material that can detect and quantify the presence of specific molecules. The silicon nanocrystal's ability to sense aromatic molecules combined with the reusability of materials formed via dissipative self-assembly prompted us to study the dissipative self-assembly of SiNCs as a recyclable sensor.

6.1. Results and Discussion

We set out to test the ability of our silicon nanocrystals to sense aromatic molecules by the addition of para-benzoquinone (p-BQ) to a solution of silicon nanocrystals. We used nanocrystals with a hexanoic acid surface functionalization. They were dissolved in a buffered solution of 200 mM 2-(N-morpholino)ethanesulfonic acid and 100 mM N-hydroxysuccinimide with a hexanoic acid concentration of 5 mM (Figure SI1). Cryogenic transmission electron microscopy and dynamic light scattering showed a radius of 3.6 ± 0.5 nm and a hydrodynamic radius of 5.5 ±1.1 nm, respectively (Figure SI2 and Table SI1). The photoluminescence showed an emission maximum at 681 nm when the samples were irradiated with UV light of 365 nm. (Figure SI3) The addition of the p-BQ as quencher rapidly decreased the photoluminescence of the silicon nanocrystals (Figure 1 and detailed experimental description Figure SI4). To our surprise, the quenched photoluminescence recovered to some degree after the addition of 7 mM EDC. We hypothesize that the dissipative self-assembly expelled part of the water and quencher molecules between the silicon nanocrystals, thus decreasing their ability to quench the fluorescence of the silicon nanocrystals (Fig. 1a). To quantify this behavior, we used three aromatic compounds known to quench silicon nanocrystals: the already mentioned para-benzoquinone, 4,4-bipyridine (4,4-BP) and 2-phenylmethylpyridine (2-PMP) with a final concentration in the silicon nanocrystal solution of 4.44, 0.13, and 1.29 mM, respectively. They reduced the photoluminescence of silicon nanocrystals by 99, 86 and, 79%, respectively (Fig. 1b). All showed an increase in photoluminescence, i.e., a loss in quenching, after the addition of EDC.

Next, we tested the silicon nanocrystal clusters use for a reusable detection platform for aromatic compounds following the schematics in figure 1a. Two different quencher molecules were added to the same silicon nanocrystals consecutively. First, we added 4,4-BP and measured a decrease in the photoluminescence of 86%. Then, 7 mM EDC was added to initiate the recovery cycle. Upon the EDC addition, the silicon nanocrystals clustered. We collected the silicon nanocrystals assemblies by centrifugation, after which they were washed, and re-dispersed in a fresh solution. The clusters disassembled over time, and the photoluminescence signal came back to 88% of the value before the addition of quencher (Fig. 1c). Then, the silicon nanocrystals

were used to measure the quenching by a second aromatic compound: 2-PMP. In response to this quencher, the photoluminescence dropped by 64% and could be recovered to 89% through the same purification cycle as mentioned above. In both sensing rounds, the photoluminescence intensity of silicon nanocrystals was not fully recovered after the recycling steps, which can be due to the loss of silicon nanocrystals in the purification steps or remaining trace amounts of quencher in the sample.

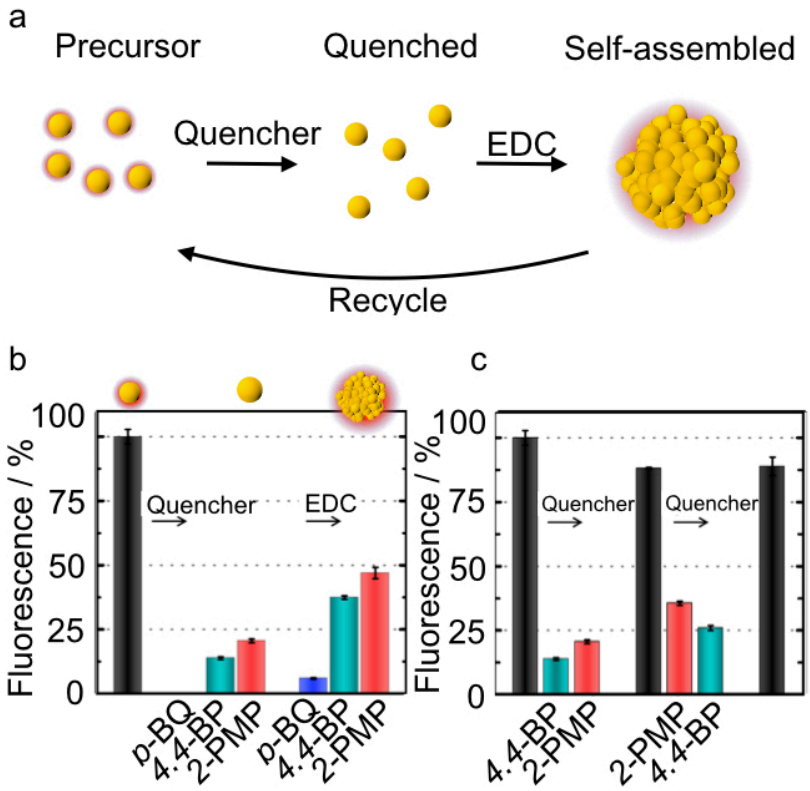

Figure 1: ***Sensing of Aromatic Molecules by Silicon Nanocrystals.*** *a) Scheme of the transient photoluminescence quenching of silicon nanocrystals. The photoluminescence of silicon nanocrystal solution quenched upon the addition of a quencher molecule. After the EDC-fueled assembly of the silicon nanocrystals, the solution regains parts of their PL intensity. Centrifugation, washing, and re-dispersion recycled the silicon nanocrystals. b) PL intensity measured for silicon nanocrystals and in the presence of quencher molecules with a digital camera (See SI). EDC addition partially recovers the fluorescence signal. c) PL intensity measured for silicon nanocrystals in two consecutive quenching cycles with 2-PMP and 4,4-BP.*

6.2. Conclusion

The combined results demonstrate that the dissipative self-assembly of silicon nanocrystals offers a reusable sensor platform of water-soluble aromatic substances. The distinct decrease of the silicon nanocrystals photoluminescence after the addition of aromatic compounds enabled us to detect and differentiate between those compounds. A second beneficial property is the reusability of the silicon nanocrystals. We demonstrated this for two consecutive sensing experiments.

6.3. Supplementary Information

For the experiments, the same nanocrystals than in the aforementioned publication were used and, the same analytics were conducted.[51] The relevant analytics are depicted beneath.

Materials and Methods

5-Hexenoic acid, hydrofluoric acid (HF, 48%) ethanol, N-hydroxysuccinimide (NHS), 1-ethyl-3-(3-dimethylaminopropyl)carbodiimide (EDC), 2-(N-morpholino) ethanesulfonic acid (MES), para-benzoquinone (*p*-BQ), 4,4-bipyridine (4,4-BP) and 2-phenylmethylpyridine (2-PMP) were purchased from Sigma-Aldrich. Azobisisobutyronitrile (AIBN) was bought from Fluka. All chemicals were used without further purification, except for NHS, which was recrystallized twice. Dry toluene was obtained from a MBraun SPS 800 solvent purification system with Argon 5.0 as the operating gas. Water was obtained from a Milli-Q water purifier system.

Synthesis of the SiNC/SiO_2 composite. The SiNCs were prepared via thermolysis of polymeric hydrogen silsesquioxane which was synthesized following a literature procedure.[55] After the synthesis, polymeric hydrogen silsesquioxane (7 g) was weighed in a quartz reaction boat, placed in to a Nabertherm RD 30/200/11 furnace with quartz working tube and heated from room temperature to a peak processing temperature of 1100 °C with 18 °C/min heating rate in a slightly reducing atmosphere (5% H_2 /95% N_2). The sample was kept at 1100 °C for 1 h. A brown solid was obtained and ground into a fine powder using a mortar and pestle. Then the composite was shaken in ethanol for 24h with high-purity silica beads using a WAB Turbula mixer for further grinding. The resulting SiNC/SiO_2 composite was dried in vacuo and stored in glass vials.

Liberation of Hydride-Terminated SiNCs. Free-standing, hydride terminated SiNCs with an average diameter of 3.6 ± 0.5 nm are obtained upon etching this composite with ethanol:water:HF (1:1:1) mixture and final extraction into toluene. 150 mg of the SiNC/SiO_2 composite was weighed into an ethylene-tetrafluoroethylene beaker equipped with a Teflon-coated stir bar. Ethanol (1.5 mL) and water (1.5 mL) were then

added and stirred to form a brown suspension. 1.5 ml 49% HF aqueous solution was added, and the composite is etched for 30 min. Hydride-terminated SiNCs were subsequently extracted from the aqueous layer into ca. 15 mL of toluene by multiple (i.e., 3 × 5 mL) extractions. The SiNC-toluene suspension was centrifuged in an ETFE-centrifuge tube at 9000 rpm for 5 mins. To remove any residual water/ethanol, extracted particles dispersed in 5 ml dry toluene and centrifuged once more.

Surface Functionalization of SiNCs. Freshly etched, hydride-terminated SiNCs were dispersed in 0.5 ml dry toluene and transferred to a Schlenk flask equipped with a stirring bar. 10 mg AIBN was dissolved in 0.5 ml dry toluene and added to the reaction flask. Upon addition of 0.3 ml 5-hexenoic acid, the reaction mixture was degassed 3 times via freeze-thaw cycles. The flask was filled with argon and placed in a 70°C oil bath for 16 hours. At the end of the reaction, functionalized SiNCs were purified by 3 centrifugation/dispersion cycles with ethanol and pentane. Resulting SiNCs were readily dispersible in ethanol.

Determination of the concentration of surface bonded –COOH groups. A fraction of 10% of the obtained SiNCs was dispersed in water and the pH was set to pH 10.5 by addition of concentration NaOH. It was titrated against HCl (0.01 M) to determine the pKa and the number of carboxylates on the SiNC surface in the sample (See Fig. S1l).

Reaction conditions for the dynamic self-assembly. The remaining fraction (90%) of the SiNCs were dispersed in degassed MES Buffer (0.2 M, pH = 6.5) with 100mM NHS to yield a 5 mM solution of carboxylates surface groups. SiNC solution referred from here on has this concentration.
All measurements and reactions were performed with freshly synthesized SiNCs and under stirring with 600 rpm if not stated otherwise.

Photoluminescence spectroscopy (PL). PL spectra were measured with an AVA-Spec 2048 from Avantes using a Prizmatix (LED Current controller) as the light source.

Dynamic light scattering (DLS). DLS measurements were performed using a Zetasizer Nano ZS from Malvern with a laser wavelength of 633 nm. The SiNCs solutions were measured using a disposable cuvette (PS). Each measurement consisted of 6 acquisitions with an acquisition time of 20 s.

Cryogenic-Transmission Electron Microscopy (cryo-TEM). Samples for cryo-TEM were prepared as described above. Shortly before imaging, the samples were diluted a 20-fold to decrease the density of SiNCs in the micrographs. Cryo-TEM imaging was performed on a Tecnai Spirit microscope (FEI/Thermo Fisher) operating at 120 kV. The grids (C-Flat R1.2/1.3, 400 mesh, Cu) were freshly glow-discharged for 90 seconds prior to use. Preparation of the grids was performed in a FEI/Thermo Fisher Vitrobot at 25 °C with the relative humidity set to 100%. The sample was incubated for 30 seconds on the grid, blotted for 2 seconds (blotting force set to -1) and then directly plunged into liquid ethane that was pre-cooled by liquid nitrogen. The cryo-TEM grids were transferred and stored in liquid nitrogen, and when needed, placed into a Gatan cryo-transfer-specimen holder to insert into the microscope. The specimen temperature was maintained at -170 °C during the data collection. The images were recorded in a low-dose mode on a CCD camera.

Supplementary Tables and Figures

Dynamic light scattering

Table SI1. Hydrodynamic diameter and PDI data of SiNCs obtained by dynamic light scattering in MES buffered aqueous solution.

	Hydrodynamic Diameter (nm)	PDI (%)
	5.0	30
	6.2	22
	5.7	24
	4.0	24
	5.9	30
	6.0	29
	4.2	24
	7.7	26
	5.2	28
	5.0	40
Mean	5.5 ± 1.1	28 ± 5

Titration of SiNC

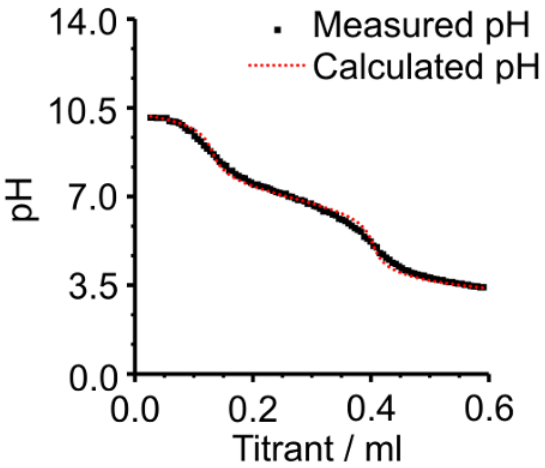

Figure SI1. *Plot of the pH value as a function of the titrant (0.01 M HCl) of a SiNC batch. The black curve indicates the measured values, whereas the red markers the fitted values by HySS 2009. Based on the fit, we calculated a pKa of 6.9 of the surface bound carboxylates. The total amount of acid in the sample was calculated to be 2.6 µmoles.*

Cryogenic-Transmission Electron Microscopy (cryo-TEM)

The analysis of the cryo-TEM pictures and the resulting data depiction followed the guidelines of Murphy and Buriak.[56] We measured 300 particles for the size distribution and applied Scott's rule for the bin width in histograms of a normal distribution.[57]

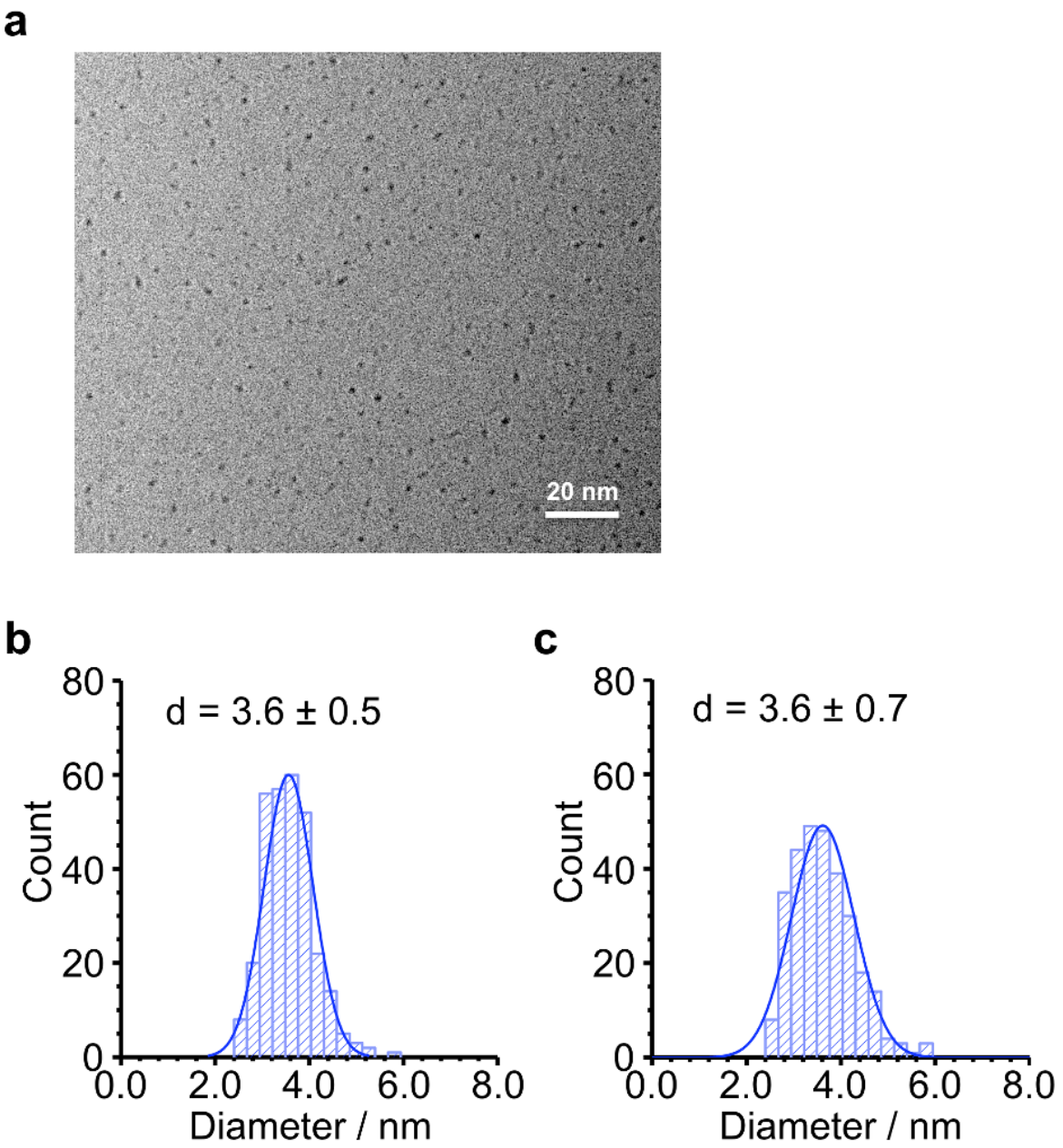

Figure SI2. a) Cryo-TEM micrographs of SiNCs 24 h after EDC addition. **b,c)** Histograms of the distribution of the SiNC diameters before (b) and 24 h after (c) 7 mM EDC addition.

Photoluminescence Spectroscopy

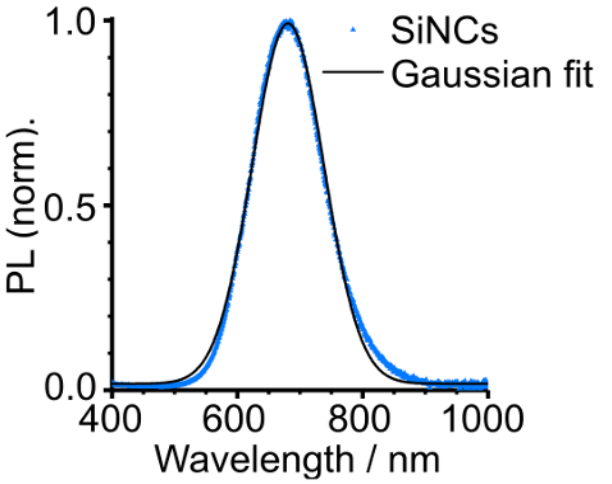

model	Gauss
equation	$y=y_0 + (A/(w*\sqrt{pi/2}))*\exp(-2*((x-xc)/w)^2)$
y_0	0.0179 ± 0.0008
x_c	680.8 ± 0.1
w	114.6 ± 0.3
A	139.9 ± 0.4
R^2(COD)	0.997

Figure SI3. *Photoluminescence (PL) of SiNCs in MES buffered aqueous solution (100 mM NHS, Ex. 365 nm).*

Quenching Efficiency Measurements

Changes in the photoluminescence intensity of silicon nanocrystals solutions excited with a wavelength of 365 nm were recorded with a digital camera (Panasonic Lumix DMC G-70, f/3.5, exposure time 1/20 s, ISO 200) positioned at a 90° angle above a 96 well plate with a fixed distance of 40 centimeters. Each well was stirred with a tiny stir bar and 200 µl of silicon nanocrystal solution. To this solution, 3, 4 or 40 µl of a 222,00, 6,40, or 6,44 mM stock solution of *para*-Benzoquinone, 4,4-Bipyridine, or 2-Phenylmethylpyridine were added. The intensity was measured with ImageJ.

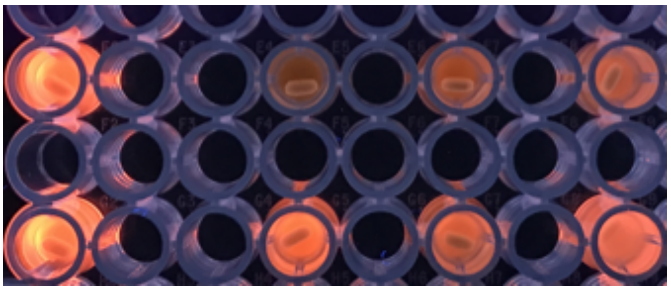

Figure SI4: ***Sensing of Aromatic Molecules in a 96 Well Plate.*** *Addition of a quencher to silicon nanocrystals. First row from left to right: blank; 4,44 mM para-Benzoquinone; 0,13 mM 4,4-Bipyridine; 1,29 mM 2-Phenylmethylpyridine. The wells in the second row have the same conditions as before with an addition of 7 mM of EDC in each well.*

Conclusion and Outlook

The aim of this thesis is to design a new chemical reaction cycle for the dissipative self-assembly of nanoparticles and study the unique material properties of the emerging assemblies. The strategy gives rise to biology-inspired unique properties like adaptivity, recyclability, self-healing, and spatiotemporal control in combination with the unique properties of nanoparticles, like photoluminescence, catalytic activity, electronic conductivity, or magnetism.

The first three chapters of this thesis describe the field of supramolecular chemistry and give three examples of reaction cycles and nanoparticles for dissipative self-assembly relevant for this thesis. The results of those already published examples show the recent development in the field.

In Chapter 4, I demonstrated a new chemical reaction cycle and its use to induce the dissipative self-assembly of gold and iron oxide nanoparticles. These fuel-driven assemblies were prone to pathway complexity, i.e., depending on the initial fuel concentration, I observed three different responses of the material, which were identified as no-assembly, dissipative self-assembly, and kinetically trapped assembly. The complete analyses of the different states concluded with an energy landscape that describes the material in detail and led to pathway complexity experiments. Iron oxide nanoparticles were used as a second nanomaterial to generalize the concept of pathway complexity in fuel-driven assemblies.

If we want to design materials that display complex function like biological materials do, *i.e.,* function like the dynamic instabilities we observe in microtubules or spontaneous self-division like we observe in bacteria, it is crucial that we understand the mechanisms that underlie such complex behavior. The work in Chapter 4 is a small step towards such an understanding. It shows that the complex behavior of assemblies driven by reaction cycle not only depend on the molecular design but also the position in the energy landscape. It also shows that certain position in the energy landscape can only be accessed by the addition of large amounts of fuel. These trapped states can, in some cases, result in unwanted behavior. On the other side, a kinetically trapped material can offer beneficial stability in a system. In general, this well-understood behavior should result in a faster characterization and usability of future designs of dissipative self-assembling nanomaterials.

In Chapter 5, I describe the dissipative self-assembly of silicon nanoparticles driven by the reaction cycle developed in Chapter 4. These assemblies are regulated by the kinetics of the reaction cycle, which we demonstrate by the fact that the lifetime of the assembly can be tuned with the amount of fuel added. The tunable lifetime prompted us to test the material's potential as a drug delivery platform. We demonstrated that these silicon nanoparticles are easily taken up by mammalian cells. We also showed that the time of the uptake can be tuned via the kinetics of the dissipative self-assembly, *i.e.,* the cells ignore the clusters, but take up the disassembled particles.

In order to further pursue the nanoparticles as a drug delivery vehicle, future steps are important. Currently, we only showed the uptake of the particles but no delivery of a bioactive payload. Thus, a cytosol-labile linker should be used to attach a biologically active substance to the nanoparticles. This should lead to the development of a drug delivery platform that has three unique properties: (1) a time-controlled release of bioactive payload (2) in combination with a shuttle for drugs to the relevant spots in a biological system that is (3) intrinsically photoluminescent, which allows the simultaneous observation of the drug distribution in a biological system. Nevertheless, this platform shows already a time-controlled material that is suitable for cell experiments.

In a second application described in Chapter 7, the dissipative self-assembly of the silicon nanocrystals was used as a reusable sensing agent for aromatic compounds. Three different aromatic molecules could be detected by the distinct decrease of the photoluminescence of the nanoparticles. Due to the reusability of the building blocks in a dissipative assembly, the platform could be reused, resulting in a reusable, non-toxic, and easy to use sensor for aromatic compounds.

In conclusion, this work describes a new chemical reaction cycle that can drive the assembly of various nanomaterials under physiological conditions. The emerging supramolecular materials possess properties like spatio-temporal control and reusability. Those properties are also found in biological systems. Thus, I achieved a dynamic system that resembles to some degree biological systems with the additional properties of synthetic nanomaterials. This thesis is a big step towards complex synthetic systems that imitate unique biological material performance.

Further Publications

Besides the two publications reprinted above with the focus on dissipative self-assembly of nanoparticles, I contributed to five more publications. Prof. Job Boekhoven and I wrote a chapter in the book Self-assembling Biomaterials that is included in the second next section. In the following section is a list of all my publications.

8.1. List of Publications

1 R. K. Grötsch, Y. Liu, C. Wanzke, M. Tena-Solsona, J. Gibbs, J. Boekhoven, Dissipative self-assembly of amphiphiles into micelles driven by a chemical fuel. **2019**, Manuscript in preparation.

2 B. Rieß[+], R. K. Grötsch[+], *The design of dissipative molecular assemblies driven by reaction cycles*. **2019**, Submitted.

3 R. K. Grötsch, C. Wanzke, M. Speckbacher, A. Angı, B. Rieger, J. Boekhoven, *Pathway dependence in the fuel-driven dissipative self-assembly of nanoparticles. JACS* **2019,** *141, 25, 9872-9878*.

4 a) M. Weger[+], R. K. Grötsch[+], M. G. Knaus, M. M. Giuman, D. C. Mayer, P. J. Altmann, E. Mossou, B. Dittrich, A. Pöthig, B. Rieger, *Non-Innocent Methylene-Linker in Bridged Lewis Pair Initiators,* Angew. Chem. Int. Ed. **2019**, *58*, 9797-9801.

b) M. Weger[+], R. K. Grötsch[+], M. G. Knaus, M. M. Giuman, D. C. Mayer, P. J. Altmann, E. Mossou, B. Dittrich, A. Pöthig, B. Rieger, *Nicht unschuldige Methylen-Linker in verbrückten Lewis-Paar-Initiatoren.* Angew. Chem. **2019**, 131, 9902- 9906.

5 a) R. K. Grötsch[+], A. Angı[+], Y. G. Mideksa, C. Wanzke, M. Tena-Solsona, M. J. Feige, B. Rieger, J. Boekhoven, Dissipative Self-Assembly of Photoluminescent Silicon Nanocrystals. Angew. Chem. Int. Ed. **2018,** *57* (44), 14608-14612.
b) R. K. Grötsch[+], A. Angı[+], Y. G. Mideksa, C. Wanzke, M. Tena-Solsona, M. J. Feige, B. Rieger, J. Boekhoven, Dissipative Selbstassemblierung photolumineszierender Siliciumnanokristalle. *Angew. Chem.* **2018,** *130*, 14817-14822.

6 B. Rieß[+], C. Wanzke[+], M. Tena-Solsona, R. K. Grötsch, J. Boekhoven, *Dissipative assemblies that inhibit their deactivation*. Soft Matter **2018,** *14*, 4852-4859.

7 R. K. Grötsch, J. Boekhoven, *11 - Unique properties of supramolecular biomaterials through nonequilibrium self-assembly.* In *Self-assembling Biomaterials*, R. M. P. d. Silva, H. S. Azevedo, Eds. Woodhead Publishing: **2018**; pp 235-250.

8 M. Tena-Solsona[+], B. Rieß[+], R. K. Grötsch, F. C. Löhrer, C. Wanzke, B. Käsdorf, A. R. Bausch, P- Müller-Buschbaum, O. Lieleg, J. Boekhoven, *Non-equilibrium dissipative supramolecular materials with a tunable lifetime.* Nat. Commun. **2017**, *8*,15895.

[+] These authors contributed equally to this work.

8.2. Unique Properties of Supramolecular Biomaterials Through Non-Equilibrium Self-Assembly.

In Self-Assembling Biomaterials

Abstract

Self-assembling Biomaterials is a part of chemistry that is very close to biology and biological materials. The idea is to use molecules present in nature or close to natural materials and self-assemble them into man-made supramolecular materials. They resemble biological materials but serve different purposes and can be designed towards those. Building blocks for those materials can be peptides, peptide amphiphiles, lipid amphiphiles sugars, and so on. In the book chapter 11, we focused on biomaterials that are out of equilibrium *via* a constant energy input. In the beginning, we explain the fundamentals of the energy landscape concerning self-assembling materials. Three classes are defined and explained in detail: in-equilibrium, non-dissipative non-equilibrium, i.e., metastable and kinetically trapped states, and dissipative non-equilibrium self-assembly. For the three non-equilibrium states, the underlying mechanisms are explained with an example of man-made material. For those materials time and the preparative pathway place an important parameter, whereas for in-equilibrium assemblies there is be no change over time observed. The same building block can end up in completely different materials and energy states depending on the steps of preparation. Moreover, the input of energy influences the material properties. Those changes are discussed and how two make use of them. Examples conclude each energy state. In the end, a short conclusion is given, and future trends are mentioned.

This work has been published:

Book chapter: 11 - Unique properties of supramolecular biomaterials through nonequilibrium self-assembly
Authors: Raphael K. Grötsch, Job Boekhoven
First published: 27. April 2018, online

Book: Self-Assembling Biomaterials, Helena. S. Azevedo; Ricardo. M. P. da Silva, Editors, **2018**, pages 235-250
Publisher: Woodhead Publishing
DOI: 10.1016/B978-0-08-102015-9.00012-5

This section states the individual work of each author in the publication above. R. K. Grötsch and J. Boekhoven both wrote paragraphs in the book chapter. The figures were primarily designed by R. K. Grötsch.

Unique properties of supramolecular biomaterials through nonequilibrium self-assembly

11

Raphael K. Grötsch, Job Boekhoven
Department of Chemistry and Institute for Advanced Study, Technical University of Munich, Garching, Germany

11.1 Introduction

In this chapter, we focus on nonequilibrium self-assembly of molecules into supramolecular assemblies. In nonequilibrium assemblies, there is a net exchange of energy and matter between the assembly and its environment. We further subdivide these assemblies in kinetically trapped assemblies, metastable assemblies, and dissipative nonequilibrium assemblies. In the first section, we will explain the subdivision in these classes and their relation with their free-energy landscapes. We will then detail each example with state-of-the-art man-made assemblies and highlight the unique material properties for each class of nonequilibrium assemblies, followed by examples of supramolecular biomaterials for each class. We will close this chapter with a perspective on where the field could benefit from a better understanding and especially better design rules for nonequilibrium assemblies.

11.2 The free energy landscapes of self-assembly

In supramolecular materials, molecules are assembled into molecular architectures with function [1]. The assembly process is driven by noncovalent, relatively weak, and thus reversible interactions between the molecules [2]. Self-assembly of molecules has been an active field of research, in part because the increasing understanding of the process has allowed to develop structures with entirely new properties. While most of the attention in the field has gone to supramolecular materials that are formed by self-assembly in equilibrium, recent attention has also focused on supramolecular materials that reside outside of equilibrium. In this section, we will discuss three types of assemblies based on their thermodynamic and kinetic properties and compare those in terms of their energy landscapes (Fig. 11.1).

Most of the attention in the field of supramolecular materials has gone to assemblies that are in equilibrium with their environment. Such assemblies can be observed when the noncovalent interactions between building blocks are relatively weak such

Self-Assembling Biomaterials. https://doi.org/10.1016/B978-0-08-102015-9.00012-5

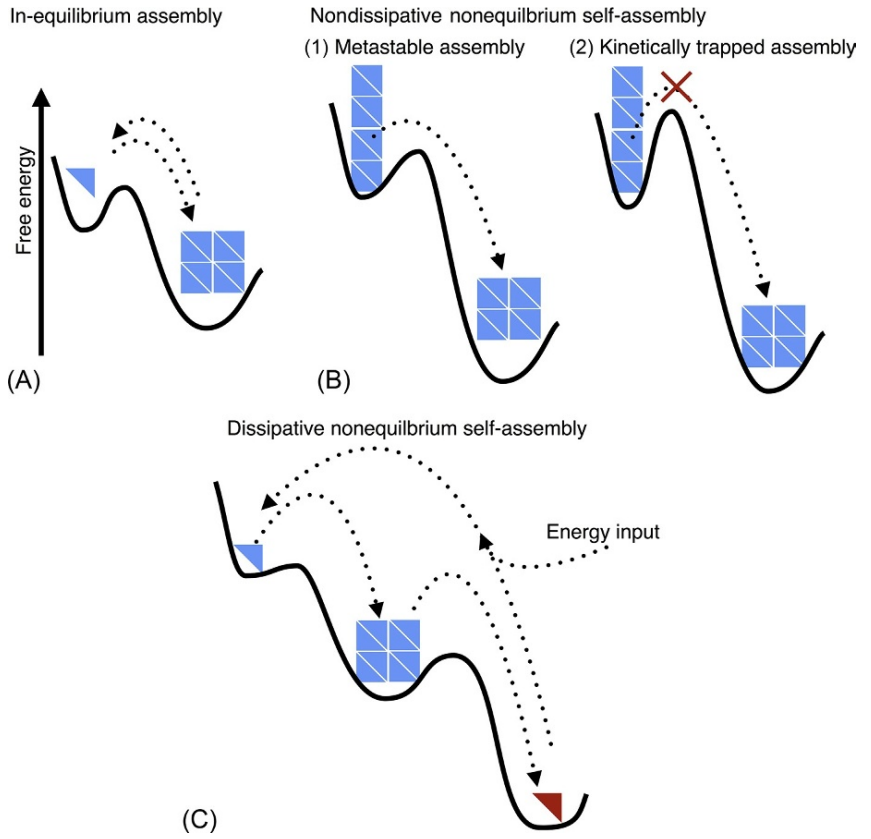

Fig. 11.1 Energy landscapes of self-assembly. Schematic representation of energy landscapes involved in the self-assembly of biomaterials. (A) In-equilibrium assemblies. (B) Out-of-equilibrium assemblies in a kinetic trap. (C) Dissipative nonequilibrium assemblies driven by chemical reaction networks.

that the thermal energy of the molecules allows relatively high exchange dynamics of nonassembled molecules with assembled ones. The rapid exchange with building blocks from the environment result in a system that can optimize its thermodynamically most favored state. Simply put, when a building block miss-assembles, the high exchange dynamics ensure rapid correction to an energetically more favorable state. The favored state corresponds to a state at the global minimum of the energy landscape [3]. In essence, the building blocks can reversibly exchange with the environment to find the most favorable state.

When the noncovalent interactions between building blocks are relatively strong, exchange of building blocks with the environment becomes slower. Consequently, the optimization to find the lowest state in the landscape is slower or sometimes even impossible. As the system is optimizing its configuration to find its thermodynamically most favored state, there is a net exchange of matter and energy between the assembly

and the rest of the system. The assembly is thus not in equilibrium with it environment. The process is referred to as nondissipative nonequilibrium self-assembly [4]. These nonequilibrium assemblies can be further divided into assemblies that do not exchange matter with their environment on any noticeable timescales and are thus "kinetically trapped" and assemblies that do exchange matter with their environment and slowly convert in their thermodynamically favored state, so-called metastable assemblies. In both cases of nonequilibrium self-assembly, the self-assembled state and thus its material properties are strongly dependent on the pathway of preparation as the self-assembled state is lacking the self-correcting mechanism that assemblies in equilibrium are endowed with. This pathway complexity can have great implications on the material properties of the self-assembled architectures [5,6].

A final type of self-assembly that we will discuss is dissipative nonequilibrium self-assembly [7]. In dissipative self-assembly, the self-assembling building blocks and their assemblies are thermodynamically unfavored. In fact, the building blocks constantly degrade to their thermodynamically more favored precursors, typically via a chemical reaction. In order to sustain the assemblies, a second chemical reaction has to constantly form the self-assembling building blocks from precursors. The ensemble results in building blocks that are constantly formed, while others are degraded. Although this mode of self-assembly might seem elaborate and complicated, it comes with unique material properties that are, in the context of supramolecular materials, vastly underexplored [8,9].

11.3 In-equilibrium self-assembly

When the noncovalent interactions between molecular building blocks are relatively weak, that is, comparable with thermal energies, a reversible ensemble is created in which the assembly can exchange building blocks with its environment. The reversibility is crucial for in-equilibrium self-assembly as it allows for a dynamic system that can try multiple modes of assemblies and self-correct to find the thermodynamically most favored state [10]. Most examples of man-made self-assembled structures are equilibrium assemblies. When assemblies are in equilibrium, we understand most of the processes at play. And because we understand, we can control and even design such materials [11–13]. In the past decades, the field of self-assembly and supramolecular materials has slowly evolved out of an era of serendipity into a time where design rules can be applied to develop materials built from the bottom up with nanometer precision. As a result, most supramolecular biomaterials will fit under this category [14,15].

In the context of biomaterials, a particularly successful and well-understood example of equilibrium assembly are the peptide amphiphiles (PAs) [16,17]. These molecules comprise three molecular domains that are important for their assembly. First, a hydrophobic domain, typically an aliphatic tail, drives molecules together by the hydrophobic effect. A second domain consists of amino acids that have a high propensity to form β-sheets. These directional interactions promote the formation of anisotropic fibers. A third domain comprises charged amino acids that ensure the fibers are water soluble [18].

A recent study on these PAs has demonstrated that these structures are in equilibrium with their environment, provided that the β-sheet domain undergoes relatively

weak interactions with neighboring PAs [19]. The elegant study used a PA that consisted of a 16-carbon alkyl tail connected to six alanine and three glutamic acid amino acids. The PAs were coassembled with very similar PAs labeled with either a green (cy3) or a red (cy5) fluorescent group. The resulting green and red fibers were mixed, and the exchange of building blocks between the two fibers was monitored by Förster resonance energy transfer (FRET). The FRET signal between cy3 and cy5 rapidly increased in the first hour and then steadily grew to a plateau value. The rate of increase in FRET signal was independent of the concentration of fibers, pointing to an exchange mechanism that is not diffusion limited. Based on these results, the authors hypothesize that the expulsion of single molecules or their reinsertion was the limiting step, similar to the exchange mechanism found for polymeric micelles [20]. The relatively rapid homogenization of the two mixed populations is a typical sign for in-equilibrium self-assembly.

Understanding the position of assemblers in the energy landscape facilitates the design of their corresponding supramolecular materials. For instance, recent work on very similar PAs has shown that a small alteration in their molecular design can make the difference between supramolecular fibers that can disrupt cell membranes and are thus toxic or supramolecular fibers that promote adhesion of cells [21]. The nontoxic PA consisted of a 16-carbon alkyl tail connected to three valine, three alanine, and three cationic lysine amino acids (PA 2). In contrast, the toxic PA consisted of a 16-carbon alkyl tail connected to three alanine, three glycine, and three cationic lysine amino acids (PA 1) (Fig. 11.2A and B). Both molecules formed seemingly similar cylindrical fibers with a diameter of 20 nm upon dispersion in water (Fig. 11.2C). However, as valine has here a higher propensity to form β-sheets compared with glycine, a difference in the ability to form strong hydrogen bonds was found. This difference was confirmed by FTIR measurements, and a strong Bragg reflection in the X-ray diffraction pattern showed crystalline hydrogen bonding of neighboring β-strands. Moreover, electron parametric resonance (EPR) spectroscopy revealed a decreased mobility of the molecules in the structures with stronger hydrogen bonding.

The subtle difference between the two PA molecules in their molecular structure evolved into the opposite behavior of cell proliferation. The lower β-sheet formation in PA 1 had a lower intermolecular cohesion. The structures were thus more dynamic, and the PAs likely interacted more with the lipid bilayer that induced cell death (Fig. 11.2D). Understanding the formation and the properties of the fibers from the molecular level up to the assembled structures opens up the possibility to design fibers that have the wanted characteristics.

11.4 Nondissipative nonequilibrium self-assembly: Metastable assemblies and kinetic traps

We demonstrated above that assemblies that are in equilibrium with their environment can exchange building blocks that endow them with a certain self-correction mechanism. Independent of the history of the system, including time since preparation or

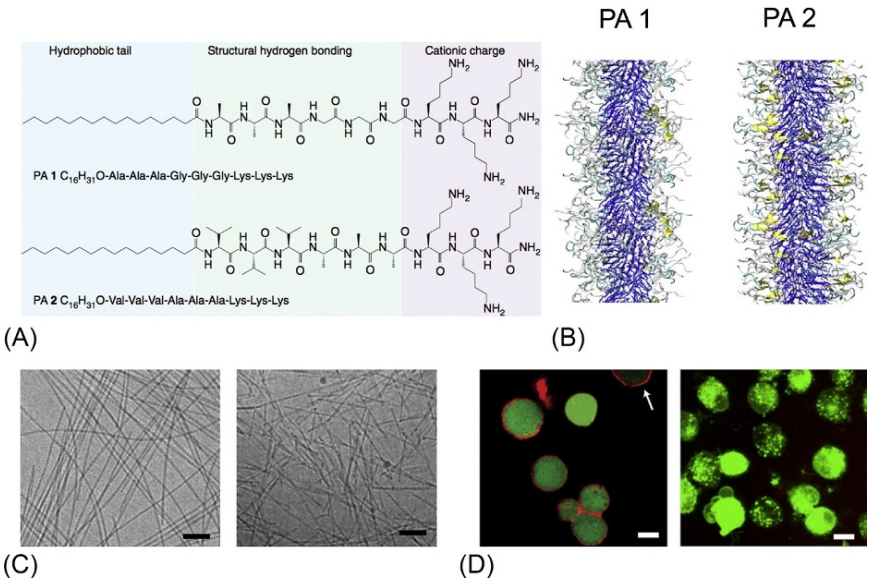

Fig. 11.2 (A) Chemical structures of PA 1 and PA 2 with equal alkyl tail length and equal number of lysine residues (cationic charge) but different propensity to form intermolecular hydrogen bonds. (B) Atomistic modeling reveals the different supramolecular interactions within the assemblies (yellow, cyan, gray, and blue indicate β-sheet hydrogen bonding, β-turn, random coil, and alkyl tail, respectively). (C) Cryo-TEM micrographs of representative assemblies in cell media. The scale bars corresponds to 100 nm. (D) Confocal micrographs of calcein stained cells settled on coatings of fluorescently labelled PA 1 (*left*) and PA 2 (*right*). Scale bars represent 10 μm.
Adapted from Newcomb CJ, Sur S, Ortony JH, Lee OS, Matson JB, et al. Cell death versus cell survival instructed by supramolecular cohesion of nanostructures. Nat Commun 2014;5:3321. Copyright 2014, Nature Publishing Group.

method of preparation, it will evolve to the same state at relatively high rates. When the noncovalent intermolecular interactions are strong, monomer exchange with the environment becomes slow or even unmeasurable [22]. In such cases, assemblies can be found in positions that are not the thermodynamically most favorable configuration and only slowly evolve to their favored configuration. When this is the case, we speak of nonequilibrium assemblies, as the assemblies are not in equilibrium with their surroundings. If the exchange is not observable on experimental timescales, the assemblies are kinetically trapped in the thermodynamically less favored states. If the exchange is observable but slow, the assemblies are metastable and slowly evolving to their favored state. In both cases, the systems lack the rapid self-correction mechanism, and the history of the assemblies plays a predominant role. The history of the assemblies is highly related to the method of sample preparations, which is why it is crucial to have a clear picture of these relations, especially in the context of supramolecular materials. In other words, when it comes to the development of supramolecular

materials that involve multiple, relatively strong interactions, not only the molecular design should be taken into consideration but also the preparative pathway. While this rule is well appreciated in the context of protein folding [23], in supramolecular materials, these relations have only recently been appreciated. In the following section, we will discuss examples of metastable assemblies and kinetically trapped assemblies and supramolecular materials.

11.4.1 Nondissipative nonequilibrium self-assembly: Metastable assemblies

A recent example by Meijer and coworkers [24] elegantly demonstrated the pathway complexity of metastable assemblies for the π-conjugated oligomer S-chiral oligo(*p*-phenylenevinylene) (SOPV, Fig. 11.3A). In methylcyclohexane (MCH) or other apolar solvents, these SOPVs self-assembled into helical structures. The authors used stopped-flow circular dichroism (CD) spectroscopy to analyze the pathway complexity and found the molecules self-assembled into either right- or left-handed helices depending on the preparative pathway (Fig. 11.3B). In earlier work, the left-handed helical aggregates were identified to be the thermodynamically most favored state [22].

Upon dispersion in apolar solvents, the molecules initially dimerized and subsequently formed disordered aggregates that developed into a nucleus. Once a critical number of building blocks in the nucleus was reached, the growth proceeded via further addition of dimers into a stack (Fig. 11.3C). While this mechanism is the same for both helices, the right-handed helix formed more rapidly than the left-handed one, resulting in an initial enrichment of the right-handed helix. Over time however, the metastable right-handed helices slowly disassembled to form the thermodynamically more favored left-handed helix. A kinetic model that was written to analyze protein fibrillization was used to further investigate the behavior of the assemblies. The model confirmed that the left-handed helix forms only under high monomer concentrations and low temperatures. With a SOPV concentration of 15 µM at 293 K, the CD signal at 466 nm showed for the first 100 s a positive signal indicating the formation of right-handed helixes. However, after the initial onset, the signal dropped to negative values, indicative of the right-handed stack, and stabilized after 3000 s. This example clearly demonstrates that the properties of the supramolecular material are dependent on the time since the preparation of the sample. Such knowledge is crucial when working with nonequilibrium supramolecular materials.

In the example above, the change is expressed in the chirality of the structures. Controlling the chirality is crucial for the functioning of supramolecular materials, and as such, a greater understanding of metastable nonequilibrium assemblies is important of the further development of the field of supramolecular (bio)materials. Moreover, such behavior not only is exclusive to SOPVs but also has been observed for other assemblers [25–28]. For example, the impressive work of Sugiyasu and coworkers investigated the self-assembly of a porphyrin molecule with alkyl chains into nanoparticles, nanofibers, or nanosheets [29]. Initially, a metastable product represented by nanoparticles formed. However, these nanoparticles transformed within 8 h to yield the thermodynamic more favored nanosheets.

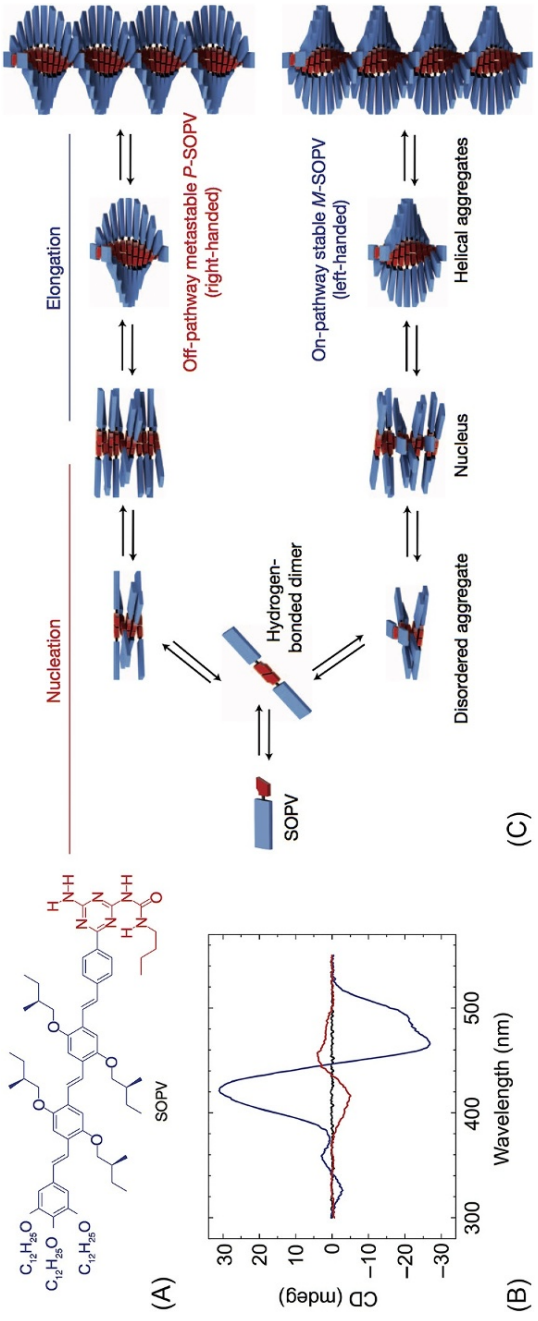

Fig. 11.3 (A) Molecular structure of monomeric SOPV. (B) CD spectra of SOPV in different energy and assembly states. *Black line*: monomeric state; *blue line*: thermodynamic state; *red line*: both M-SOPV and metastable P-SOPV in one sample. (C) Scheme showing two assembly pathways leading to two different helices. After the formation of a hydrogen bonded dimer and the formation of a nucleus, the assemblies continues to form helices. This is achieved by a nucleation elongation mechanism in apolar solvents. The right-handed (P) helix forms quickly but is less stable than the left hand (M) helix.
Adapted from Korevaar PA, de Greef TF, Meijer EW. Pathway complexity in π-conjugated materials. Chem Mater 2013;26:576–86.

11.4.2 Nondissipative nonequilibrium self-assembly: Kinetic traps

In the examples above, metastable supramolecular assemblies relaxed over time to their thermodynamically favored state. In cases where such relaxation is unnoticeable, we speak of kinetically trapped states. In this class of nonequilibrium assembly, the structure is not in the thermodynamically most favored state, and the system does not have sufficient energy to overcome the barrier toward that state [30].

An example of assemblies that are kinetically trapped has been described by Ulijn and coworkers. They used peptides with aromatic groups that could enzymatically be converted into building blocks that assemble into fibers. The fibers entrapped their solvent resulting in the formation of hydrogels [31]. The aromatic peptide consisted of a dipeptide protected on the *N*-terminus with *N*-(fluorenyl-9-methoxycarbonyl) (Fmoc) group and on the C-terminus with a methyl ester (Fig. 11.4A). The methyl ester at the C-terminus of the dipeptide was hydrolyzed to the acid by subtilisin, a hydrolytic enzyme. The difference in molecular structure between the ester and acid was sufficient to induce a morphological transition from a solution state into fibers that entangled and formed a hydrogel (Fig. 11.4B). The aromatic dipeptides were incubated with different concentrations of enzyme for an hour at 55°C, after which the samples were cooled to room temperature. Using HPLC analysis, the authors could conclude that for each concentration of enzyme, full conversion to the carboxylic acid was reached. Moreover, for each concentration of enzyme, the sample had transformed into a hydrogel. However, the strength of the gel was not similar between samples. In fact, the higher the enzyme concentration, the higher the melting point of the gel (Fig. 11.4C). Fourier transformed infrared spectroscopy (FTIR) studies combined with CD spectroscopy confirmed the β-sheet formation between the peptides, while fluorescence emission spectra showed π-π stacking of the Fmoc groups. However, also here, the authors found

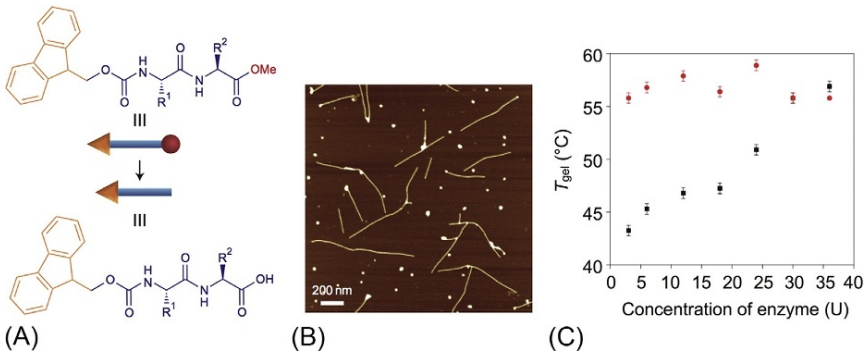

Fig. 11.4 (A) Fmoc-dipeptide methyl esters before and after the Subtilisin catalyzed hydrolysis to the corresponding acids. (B) AFM images showing the beginning of the agglomeration of fibers and clusters. (C) Diagram showing the melting temperature (T_{gel}) of gels. Black markers indicate the T_{gel} of gels with Subtilisin catalysis. Red markers specify the T_{gel} of gels after a heating cooling cycle.
Adapted from Hirst AR, Roy S, Arora M, Das AK, Hodson N, et al. Biocatalytic induction of supramolecular order. Nat Chem 2010;2:1089–94. Copyright 2010, Nature Publishing Group.

that the higher the enzyme concentration, the greater the signal for β-sheet formation. These observations are surprising, since each sample contains the exact same amount of aromatic dipeptide building blocks, under the exact same conditions (pH, temperature, and buffer). The only difference between the samples is a difference in concentration enzyme and thus a difference in rate of formation of the molecular building blocks for the fibers. Such differences in material properties depending on the preparative pathway (fast formation vs. slow formation) are a typical feature of kinetically trapped states. Indeed, the authors showed that the effect was a result of kinetic effects by annealing the samples to induce disassembly. The gels were reformed after gently cooling down these solutions. For these samples, the CD signals after a heating-cooling cycle of the samples with different catalyst concentrations were identical.

From the above example, it is clear that for supramolecular materials in which noncovalent interactions are relatively strong, the properties can depend on the preparative pathway as molecules can remain locked in kinetic traps. A greater understanding of such trapping mechanisms allows the user to tune their material properties simply by changing the preparative pathway and making use of the free-energy landscape. Studies by other groups have shown that this behavior not only is limited to enzymatic conversion of precursors but also can be induced by organocatalytic conversion of well-soluble precursors into hydrogel-forming assemblers [32]. The authors found, in line with the example above, that an increase rate of product formation results in an increased strength of the gels.

A recent study found that also the formation of fibers by PAs can be strongly dependent on the preparative pathway [32a]. This result might sound counterintuitive as we mentioned in Section 11.2 PA fibers that were in-equilibrium structures. We have to point out that this difference has to do with the noncovalent interactions between the PAs. The main difference between the two PAs is their ability to form β-sheets. While the PAs mentioned above with six alanine amino acids formed relatively weak β-sheets, the PAs that can be kinetically trapped into fibers comprise three valine and three alanine amino acids. Valine is known to have a higher propensity to form β-sheets compared with alanine [33]. The balance between forces that drive self-assembly can change the behavior of otherwise relatively similar molecules. The PA used in this study consisted of a 16-carbon chain, followed by three valine, three alanine, and three lysine amino acids. After the dissolution of the PA in water, preparation of the different supramolecular materials was achieved in two steps: annealing (heating to 80°C and gently cooling to room temperature) and dilution. It is important to note that annealing typically gives molecules sufficient energy to navigate the energy landscape and position themselves in the thermodynamically most favored configuration. Dilution on the other hand changes the environment of the assemblies and can thus bring the assemblies from one energy landscape to another.

The authors showed that freshly dissolved PA at a relatively high concentration (4.4 mM) was characterized by short fibers. These short fibers represented a metastable state in the energy landscape and slowly grew to long fibers driven by β-sheet formation as evidenced by cryo-TEM and CD spectroscopy. The long fibers were thus the thermodynamically favored state, and the transition to this state could be accelerated by an annealing step. When the fibers were diluted to a relatively low concentration (0.44 mM), the ionic repulsion between the lysine groups disfavored the

formation of β-sheets. As these β-sheets were the driving force for fiber elongation, the thermodynamically favored states under these conditions were short fibers as evidenced by cryo-TEM. The authors confirmed this by first diluting the metastable fibers at 4.4 to a concentration of 0.44 mM and then annealing the sample. This pathway resulted in the short thermodynamically favored fibers. In contrast, when the exact same sample was first annealed at a high concentration, giving long fibers, and then diluted to 0.44 mM, the long fibers were still found. The kinetically trapped long fibers were stable for months. In essence, the molecules in the long fibers did not have sufficient energy to disassemble and form the thermodynamically favored short fibers. Only upon reannealing the samples were the short fibers found (Fig. 11.5A).

The finding implies that two different morphologies can be found, for the exact same molecule under the exact same conditions. The only difference between the two samples is their history. Unsurprisingly, the difference in supramolecular structure resulted in different material properties. For instance, when immobilized on a surface, the interaction between cells and fibers was different. Fibroblast cells on surfaces that comprise the short fibers were unable to sufficiently adhere and remained relatively round (Fig. 11.5B). In contrast, the same cells on surfaces of the long fibers were able to adhere and elongate. Cells on the latter surface also survived for longer times. Using atomic force microscopy (AFM) studies, the authors found that the surface comprising long fibers was drastically better at sustaining pulling force compared with the surface of short fibers. It is thus hypothesized that the short fibers are not able to sustain the forces exerted by the fibroblasts, while the long fibers are. To further confirm the difference in material properties, the authors exposed cells to the fibers in solutions. It was found that the short fibers were significantly more toxic compared to the long fibers (Fig. 11.5C). The mechanism for the latter observation remains unclear, but the authors hypothesize that the increased number of endcaps on short fibers compared with long fibers might increase the ability of fibers to lethally penetrate the cells.

11.5 Dissipative nonequilibrium assembly

In dissipative nonequilibrium self-assembly, both the building blocks and its assemblies are thermodynamically unfavored. In fact, the thermodynamically favored state is a precursor state that does not assemble at all [9]. Only by the consumption of an external source of energy can the precursor be "pushed" out of equilibrium into a building block state that can assemble. Since the assemblies are not thermodynamically favored, they disassemble and revert to the precursor state. The energy source can be provided by means of chemical reactions. In the first reaction, the precursor is converted into the building block that can then assemble. As the activation pushes the precursor higher in the energy landscape, it is not a spontaneous reaction, but it is driven by the consumption of a sacrificial high-energy species. This high-energy species can be a photon in photochemical activation reaction or a small molecule such as the ubiquitous adenosine triphosphate (ATP) or guanosine triphosphate (GTP) in biology [34]. Upon activation, the building block can self-assemble. Crucially, the building

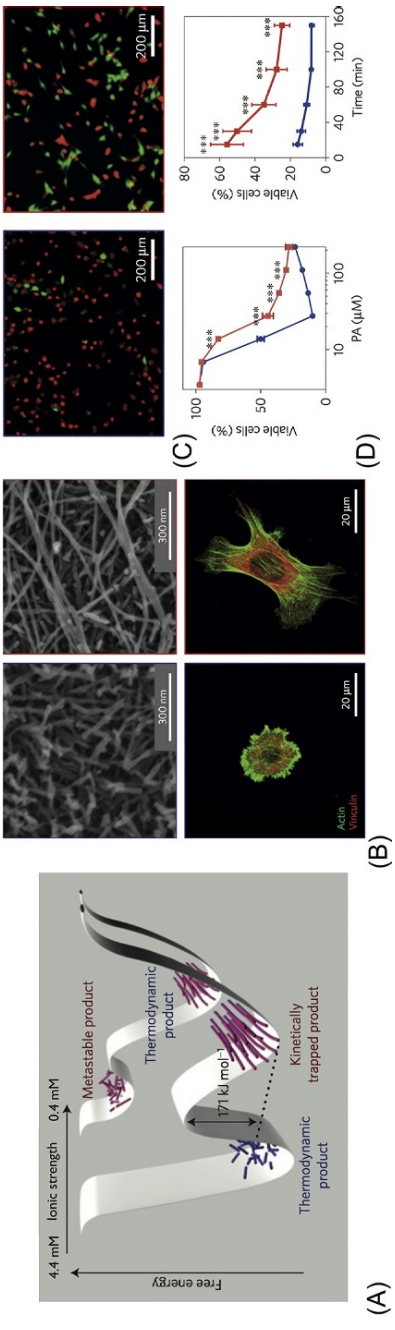

Fig. 11.5 (A) Illustration of the free energy landscapes of PA assemblies with the free energy on the *y*-axis and the ionic strength from 4.4 to 0.4 mM on the *x*-axis. The ionic strength influences the β-sheet formation, so that low concentration leads to short fibers in a metastable state and long fibers in a thermodynamic state. For a high concentration of 4.4 mM the stable product is short fibers and a kinetically trapped long fiber product appears with an energy barrier of 171 kJ mol^{-1}. (B) SEM showing the same PA with short or long fibers. Cells observed with immunofluorescent staining showing relatively rounds cells as a sign of bad attachment to the short fibers and a spread cell as a sign for successful attachment to surface of long fibers. (C) C2C12 premyoblasts in cell media with short (*left*) and long (*right*) PA fibers after 3 h. Green indicates living cells and red shows dead cells (*upper left and right*). (D) Viable cells in relation to PA concentration after 3 h (*lower left*). Viable cells with 110 μM PA monitored over time (*lower right*).
Adapted from Tantakitti F, Boekhoven J, Wang X, Kazantsev RV, Yu T, Li J, et al. Energy landscapes and functions of supramolecular systems. Nat Mater 2016;15(4):469–76. Copyright 2016, Nature Publishing Group.

block spontaneously deactivates into the thermodynamically favored precursor. After deactivation, the precursor can undergo another cycle.

A pioneering example of molecular dissipative self-assembly driven by chemical reaction networks has been described by van Esch and coworkers [35]. That work used *N*,*N*′-dibenzoyl-L-cystine (DBC), a dicarboxylate that was well soluble in water, as a precursor (Fig. 11.6A and B) [36]. It was found that the carboxylates of DBC could be methylated into the corresponding methyl ester by methylating agents such as methyl iodide (MeI) and dimethyl sulfate (DMS) to yield DBC-OMe_2. For instance, the authors described that addition of a batch of 100 mM of MeI to 100 mM DBC resulted in the formation of the mono- and diesters of it corresponding dicarboxylate. Crucially, in the aqueous environment, the ester was an unstable molecule, and it slowly hydrolyzed back to the original precursor (DBC) state. After about 100 h, a maximum in ester concentrations was found, whereas after 350 h, all ester had been hydrolyzed, and thus, all DBC had been recovered. At 400 h, a second batch of methyl iodide was added and the cycle repeated.

Lacking the two anionic dicarboxylates, the diester building block was much less soluble than its corresponding precursor. In fact, the ester was found to self-assemble into fibers by electron microscopy studies. By means of dynamic light scattering, the turbidity of the samples was measured in response to the addition of the fuel. The signal transiently increased with a similar lifetime as the esters, pointing to the formation of large assemblies when the esters are present. Finally, electron microscopy revealed the presence of fibers in samples that had been exposed to the methyl iodide (Fig. 11.6C and D).

Coupling the assembly of building blocks to energy dissipating chemical reaction networks is cumbersome and elaborate, but it comes with unique properties that remain largely unexplored. The authors showed in follow-up work [37] that the lifetime of the corresponding fibrillar materials can be controlled by kinetic parameters, such as the initial amount of methylating agent added or the pH of the system, resulting in gels that are present for hours or weeks. Such temporal control over material properties opens the door to unique supramolecular materials that disintegrate at predefined times. Moreover, it was demonstrated that the corresponding materials were self-healing, provided that the system contained sufficient amounts of methylating agent.

Clearly, the use of toxic methylating agents to drive the assembly makes them unsuitable as applicable biomaterials. However, more recent work has shown that dissipative nonequilibrium self-assembly is not limited to dicarboxylate ester conversion. For instance, Ulijn and coworkers showed that transient and dynamic fiber formation could be induced by a chemical reaction network that uses α-chymotrypsin to condense a well-soluble amine with a methyl ester into an amide that self-assembled into hydrogel-forming fibers [38]. The authors chose the conditions such that the enzyme also hydrolyzes the amide product to the original amine and a carboxylate waste product. In this system, the cycle time was tunable in the range of 200–1000 min with the amount of enzyme. As a result, the authors could develop transient hydrogels with lifetimes in the order of roughly 100–600 min.

In recent work, our group introduced a chemical reaction network based on the condensation of a dicarboxylate into its corresponding anhydride at the expense of a

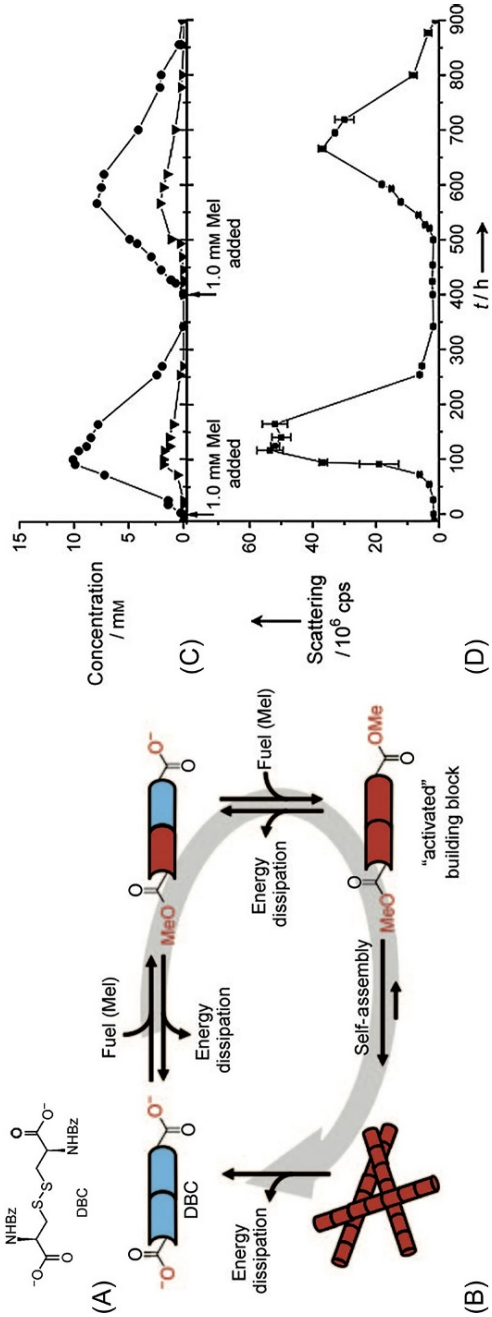

Fig. 11.6 (A) Molecular structure of *N,N'*-dibenzoyl-L-cystine (DBC) is the precursor in this study. (B) Chemical reaction network that drives the dissipative self-assembly formation of fibers. The precursor (DBC, *blue*) can react twice with high-energy methylating agent MeI resulting in the formation of the activated building block (diester, *red*). The activated building block self-assembles into fibers but is intrinsically unstable and slowly hydrolyzes back to the original DBC precursor. (C) Concentration profiles of mono- *(circle)* and diester *(triangle)* and (D) scattering profiles in response to an addition of 1 mmol of MeI to 100 mM DBC. After 400 h, a second 1 mmol batch is added in order to start a second cycle.
Adapted from Boekhoven J, Brizard AM, Kowlgi KN, Koper GJ, Eelkema R, et al. Dissipative self-assembly of a molecular gelator by using a chemical fuel. Angew Chem Int Ed Eng 2010;49:4825–8. Copyright 2010, John Wiley & Sons.

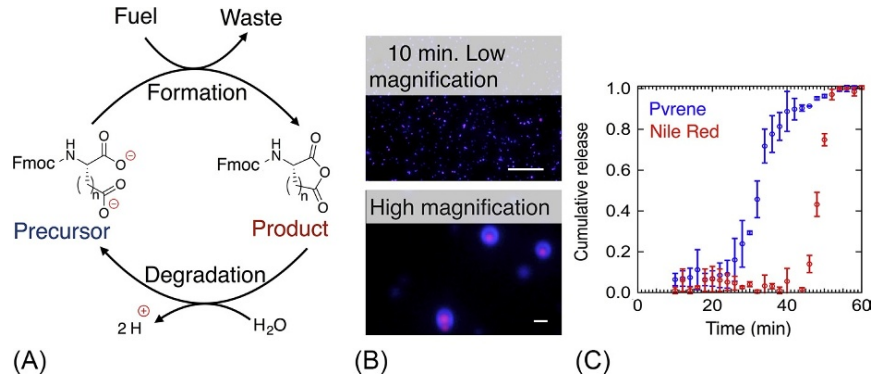

Fig. 11.7 (A) Chemical reaction network that drives the dissipative nonequilibrium self-assembly formation of fibers. The precursor can react with high-energy carbodiimide fuels resulting in the formation of the activated anhydride product. The activated building block is intrinsically unstable and rapidly hydrolyzes back to the original precursor. (B) Fluorescence microscopy of the transient colloids formed by Fmoc-E in response to EDC as a fuel. EDC was added to 10 mM Fmoc-E with 2.5 μM Nile red *(red)*. After 5 min, 25 μM pyrene *(blue)* was added. The sequential addition of the dyes resulted in incorporation of the Nile red in the core of the particles, while the pyrene was mostly found in the outer layers. (C) Release profiles of pyrene and Nile red of the particles described in (B). Adapted from Tena-Solsona M, et al. Non-equilibrium dissipative supramolecular materials with a tunable lifetime. Nat Commun 2017;8:15895. https://doi.org/10.1038/ncomms15895. Copyright 2017, Nature Publishing Group.

high-energy carbodiimide fuel [39]. While the dicarboxylate precursor had two negative charges, the anhydride product was uncharged (Fig. 11.7A). This hydrophobization was used to induce the self-assembly of the product. In the aqueous environment, the anhydride product was extremely labile and rapidly reacted back to the original precursor. For instance, while the Fmoc-glutamic acid precursor was well soluble, addition of 1-ethyl-3-(3-dimethylaminopropyl)carbodiimide (EDC) as a source of carbodiimide converted part of the acid into the anhydride that in turn self-assembled in colloids. The lifetime of the colloids could be tuned by the amount of EDC from minutes to hours. Moreover, the colloids could be loaded with various hydrophobic molecules in a sequential manner, resulting in particles with several layers of hydrophobic molecules (Fig. 11.7B). As the particles degraded, these hydrophobic molecules were released in a sequential manner, opening the door to drug delivery vehicles that can release hydrophobic agents in a sequential manner at predefined times (Fig. 11.7C).

11.6 Conclusion and future trends

In this chapter, we have illustrated the differences between in and out of equilibrium self-assembly. Because assemblies in equilibrium assemblies do not change over time, their material properties are constant and independent of history. In contrast, the properties of nondissipative nonequilibrium materials, which include metastable and

kinetically trapped assemblies, depend highly on their preparative pathway. Finally, in dissipative nonequilibrium self-assembly, the formation of materials is coupled to chemical reaction networks that result in materials that are dynamic and of which the lifetime can be tuned by kinetics. In the context of biomaterials, the latter has been ill-explored.

References

[1] Amabilino DB, Smith DK, Steed JW. Supramolecular materials. Chem Soc Rev 2017;46:2404.
[2] Whitesides GM, Grzybowski B. Self-assembly at all scales. Science 2002;295:2418–21.
[3] Whitesides GM, Boncheva M. Beyond molecules: self-assembly of mesoscopic and macroscopic components. Proc Natl Acad Sci U S A 2002;99:4769–74.
[4] Sorrenti A, Leira-Iglesias J, Markvoort AJ, de Greef TF, Hermans TM. Non-equilibrium supramolecular polymerization. Chem Soc Rev 2017;46:5476–90.
[5] Ogi S, Fukui T, Jue ML, Takeuchi M, Sugiyasu K. Kinetic control over pathway complexity in supramolecular polymerization through modulating the energy landscape by rational molecular design. Angew Chem Int Ed Eng 2014;53:14363–7.
[6] Fukui T, Kawai S, Fujinuma S, Matsushita Y, et al. Control over differentiation of a metastable supramolecular assembly in one and two dimensions. Nat Chem 2016;9:493–9.
[7] Grzybowski BA, Wilmer CE, Kim J, Browne KP, Bishop KJM. Self-assembly: from crystals to cells. Soft Matter 2009;5:1110–28.
[8] Fialkowski M, Bishop KJ, Klajn R, Smoukov SK, Campbell CJ, et al. Principles and implementations of dissipative (dynamic) self-assembly. J Phys Chem B 2006;110:2482–96.
[9] van Rossum SAP, Tena-Solsona M, van Esch JH, Eelkema R, Boekhoven J. Dissipative out-of-equilibrium assembly of man-made supramolecular materials. Chem Soc Rev 2017;46:5519–35.
[10] Whitesides GM, Boncheva M. Beyond molecules: self-assembly of mesoscopic and macroscopic components. Proc Natl Acad Sci U S A 2002;99:4769–74.
[11] Ulijn RV, Smith AM. Designing peptide based nanomaterials. Chem Soc Rev 2008;37:664–75.
[12] Van Esch JH. We can design molecular gelators, but do we understand them? Langmuir 2009;25:8392–4.
[13] Cui H, Webber MJ, Stupp SI. Self-assembly of peptide amphiphiles: from molecules to nanostructures to biomaterials. Biopolymers 2010;94:1–18.
[14] Webber MJ, Appel EA, Meijer EW, Langer R. Supramolecular biomaterials. Nat Mater 2016;15:13–26.
[15] Boekhoven J, Stupp SI. 25th anniversary article: supramolecular materials for regenerative medicine. Adv Mater 2014;26:1642–59.
[16] Hartgerink JD, Beniash E, Stupp SI. Self-assembly and mineralization of peptide-amphiphile nanofibers. Science 2001;294:1684–8.
[17] Hartgerink JD, Beniash E, Stupp SI. Peptide-amphiphile nanofibers: a versatile scaffold for the preparation of self-assembling materials. Proc Natl Acad Sci U S A 2002;99:5133–8.
[18] Cui H, Webber MJ, Stupp SI. Self-assembly of peptide amphiphiles: from molecules to nanostructures to biomaterials. Biopolymers 2010;94:1–18.
[19] Da Silva RM, Van Der Zwaag D, Albertazzi L, Lee SS, Meijer EW, et al. Super-resolution microscopy reveals structural diversity in molecular exchange among peptide amphiphile nanofibres. Nat Commun 2016;7:11561.

Acknowledgments

First of all, I want to thank *Prof. Job Boekhoven* for the possibility to work in his lab and for the interesting topic of my thesis. We started together in Munich in Januar 2016 and found empty labs and offices. Now it almost seems surreal after what we achieved in the last three years. From the beginning, it was always possible to just walk in the office and brainstorm about science and solve all kinds of problems related to my thesis. Thank you for your direct, scientific and very helpful attitude!

I want to thank *Dr. Marta Tena-Solsona*. The three of us started together and the first duties were to set up the necessary equipment to be able to conduct experiments. As a postdoc, *Marta* helped with scientific discussion and with her role model of how to do research and make good progress. She was the person you need to start with an empty lab.

Together, *Benedikt Rieß* and *Caren Wanzke* we were the first generation of the BoekhovenLab Ph.D. students. The teamwork in such a small group is special and was very harmonic. We started our relationship as working colleagues, and it evolved into a friendship.

Thanks to *Arzu Angi* and *Tobias Helbich* for their help and friendship during my Ph.D. Having a breakfast at 6:30 in the morning and working for hours in a dark room definitely influenced the outcome of my Ph.D. And maybe also blinded our eyesight.

I also want to thank the whole group that developed from three members in the beginning to quiet a bunch of people: *Fabian Schnitter, Jun Sawada, Patrick Schwarz, Carsten Donau, Kun Dai, Michaela Würbser, Laura Tebacharani, Alexander Bergmann* and *Sebastian Auffarth*. *Alexander* worked with me on the Gold nanoparticles during his internship and *Sebastian* was doing his master thesis on the next generation of silicon nanocrystals.

I want to thank *Maximillian Speckbacher* for our time in Edmonton and also for his work on the gold nanoparticles.

I want to give a special thanks to *Prof. Bernhard Rieger, Carsten Troll and, Sergei Vagin*. They helped me and the whole group especially in the beginning with support in administrative and technical questions. It felt like being still part of the Wacker-chair and helped a lot in building up the own group. Thank you, *Sergei,* for all your work in the ATUMS project.

Being a part of the ATUMS group here in Munich and also in Edmonton was a very enjoyable experience. For all kinds of challenges, there was always a person to go to and to receive help.

Am Ende möchte ich mich bei meinen Eltern *Marita* und *Georg* bedanken, die mir erst die Möglichkeit hierzu gegeben haben. Auch meinen Geschwistern *Florian* und *Teresa* möchte ich Danken. Sie haben mich immer unterstützt und für den nötigen Ausgleich gesorgt.

Auch dir, *Sophia*, möchte ich Danken. Du hast mich die letzten Jahre am engsten begleitet und unterstützt. So auch wenn ich mal wieder länger gearbeitet habe oder nur noch schnell, eine Stunde oder spontan Übernacht, etwas fertig machen musste.

References

1 F. Wöhler, Ueber künstliche Bildung des Harnstoffs. *Annalen der Physik* **1828,** *88* (2), 253-256.

2 E. M. Suh, Y. Kishi, Synthesis of Palytoxin from Palytoxin Carboxylic Acid. *Journal of the American Chemical Society* **1994,** *116* (24), 11205-11206.

3 M. C. T. Fyfe, J. F. Stoddart, Synthetic Supramolecular Chemistry. *Accounts of Chemical Research* **1997,** *30* (10), 393-401.

4 J.-M. Lehn. Nobel Lecture, NobelPrize.org, Nobel Media AB 2019. https://www.nobelprize.org/prizes/chemistry/1987/lehn/lecture/. Accessed 14.04.2019.

5 H. M. Powell, 15. The structure of molecular compounds. Part IV. Clathrate compounds. *Journal of the Chemical Society (Resumed)* **1948,** (0), 61-73.

6 H. M. Powell, Structure of Clathrate Compounds. *Nature* **1951,** *168* (4262), 11-14.

7 C. J. Pedersen, Cyclic polyethers and their complexes with metal salts. *Journal of the American Chemical Society* **1967,** *89* (10), 2495-2496.

8 C. J. Pedersen, Cyclic polyethers and their complexes with metal salts. *Journal of the American Chemical Society* **1967,** *89* (26), 7017-7036.

9 B. Dietrich, J. M. Lehn, J. P. Sauvage, Diaza-polyoxa-macrocycles et macrobicycles. *Tetrahedron Lett.* **1969,** *10* (34), 2885-2888.

10 G. R. Desiraju, Chemistry beyond the molecule. *Nature* **2001,** *412* (6845), 397-400.

11 B. A. Grzybowski, K. Fitzner, J. Paczesny, S. Granick, From dynamic self-assembly to networked chemical systems. *Chemical Society Reviews* **2017,** *46* (18), 5647-5678.

12 J. Borges, J. F. Mano, Molecular Interactions Driving the Layer-by-Layer Assembly of Multilayers. *Chemical Reviews* **2014,** *114* (18), 8883-8942.

13 J. Wang, K. Liu, R. Xing, X. Yan, Peptide self-assembly: thermodynamics and kinetics. *Chemical Society Reviews* **2016,** *45* (20), 5589-5604.

14 M. R. Jones, N. C. Seeman, C. A. Mirkin, Programmable materials and the nature of the DNA bond. *Science* **2015,** *347* (6224), 1260901.

15 E. Barry, Z. Dogic, Entropy driven self-assembly of nonamphiphilic colloidal membranes. *PNAS* **2010,** *107* (23), 10348.

16 Y. Min, M. Akbulut, K. Kristiansen, Y. Golan, J. Israelachvili, The role of interparticle and external forces in nanoparticle assembly. *Nature Materials* **2008,** *7*, 527.

17 The Nobel Prize in Chemistry 2016, NobelPrize.org, Nobel Media AB 2019. https://www.nobelprize.org/prizes/chemistry/2016/press-release/. Accessed 15.04.2019.

18 T. Kudernac, N. Ruangsupapichat, M. Parschau, B. Maciá, N. Katsonis, S. R. Harutyunyan, K.-H. Ernst, B. L. Feringa, Electrically driven directional motion of a four-wheeled molecule on a metal surface. *Nature* **2011,** *479*, 208.

19 N. Koumura, R. W. J. Zijlstra, R. A. van Delden, N. Harada, B. L. Feringa, Light-driven monodirectional molecular rotor. *Nature* **1999,** *401* (6749), 152-155.

20 D. Roke, S. J. Wezenberg, B. L. Feringa, Molecular rotary motors: Unidirectional motion around double bonds. *PNAS* **2018,** *115* (38), 9423.

21 C. J. Bruns, J. F. Stoddart, Rotaxane-Based Molecular Muscles. *Accounts of Chemical Research* **2014,** *47* (7), 2186-2199.

22 C. O. Dietrich-Buchecker, J.-P. Sauvage, A Synthetic Molecular Trefoil Knot. *Angewandte Chemie International Edition in English* **1989,** *28* (2), 189-192.

23 R. K. Grötsch, J. Boekhoven, 11 - Unique properties of supramolecular biomaterials through nonequilibrium self-assembly. In *Self-assembling Biomaterials*, R. M. P. d. Silva, H. S. Azevedo, Eds. Woodhead Publishing: 2018; pp 235-250.

24 A. Sorrenti, J. Leira-Iglesias, A. J. Markvoort, T. F. A. de Greef, T. M. Hermans, Non-equilibrium supramolecular polymerization. *Chem. Soc. Rev.* **2017,** *46* (18), 5476-5490.

25 S. A. P. van Rossum, M. Tena-Solsona, J. H. van Esch, R. Eelkema, J. Boekhoven, Dissipative out-of-equilibrium assembly of man-made supramolecular materials. *Chem. Soc. Rev.* **2017,** *46* (18), 5519-5535.

26 G. M. Whitesides, M. Boncheva, Beyond molecules: self-assembly of mesoscopic and macroscopic components. *Proc Natl Acad Sci U S A* **2002,** *99* (8), 4769-74.

27 A. Patist, S. G. Oh, R. Leung, D. O. Shah, Kinetics of micellization: its significance to technological processes. *Colloids and Surfaces A: Physicochemical and Engineering Aspects* **2001,** *176* (1), 3-16.

28 G. Karp, The Cytoskeleton and Cell Motility. In *Cell biology*, 7. ed.; Wiley: Hoboken, NJ, 2014; Vol. internat. student version, pp 324-353.

29 J. Al-Bassam, F. Chang, Regulation of microtubule dynamics by TOG-domain proteins XMAP215/Dis1 and CLASP. *Trends in Cell Biology* **2011,** *21* (10), 604-614.

30 L. Schaedel, K. John, J. Gaillard, M. V. Nachury, L. Blanchoin, M. Théry, Microtubules self-repair in response to mechanical stress. *Nature Materials* **2015,** *14*, 1156.

31 M. Tena-Solsona, J. Boekhoven, Dissipative Self-Assembly of Peptides. *Israel Journal of Chemistry* **2019,** *0* (0).

32 B. Rieß, J. Boekhoven, Applications of Dissipative Supramolecular Materials with a Tunable Lifetime. *ChemNanoMat* **2018,** *4* (8), 710-719.

33 J. Boekhoven, W. E. Hendriksen, G. J. Koper, R. Eelkema, J. H. van Esch, Transient assembly of active materials fueled by a chemical reaction. *Science* **2015,** *349* (6252), 1075-9.

34 S. Debnath, S. Roy, R. V. Ulijn, Peptide nanofibers with dynamic instability through nonequilibrium biocatalytic assembly. *J. Am. Chem. Soc.* **2013,** *135* (45), 16789-92.

35 C. G. Pappas, I. R. Sasselli, R. V. Ulijn, Biocatalytic Pathway Selection in Transient Tripeptide Nanostructures. *Angew. Chem. Int. Ed.* **2015,** *54* (28), 8119-8123.

36 G. Kumar, L. Tibbitts, J. Newell, B. Panthi, A. Mukhopadhyay, R. M. Rioux, C. J. Pursell, M. Janik, B. D. Chandler, Evaluating differences in the active-site electronics of supported Au nanoparticle catalysts using Hammett and DFT studies. *Nature Chemistry* **2018,** *10*, 268.

37 O. Wolf, M. Dasog, Z. Yang, I. Balberg, J. G. C. Veinot, O. Millo, Doping and Quantum Confinement Effects in Single Si Nanocrystals Observed by Scanning Tunneling Spectroscopy. *Nano Letters* **2013,** *13* (6), 2516-2521.

38 M. Haase, H. Schäfer, Upconverting Nanoparticles. *Angew. Chem. Int. Ed.* **2011,** *50* (26), 5808-5829.

39 A.-H. Lu, E. L. Salabas, F. Schüth, Magnetic Nanoparticles: Synthesis, Protection, Functionalization, and Application. *Angew. Chem. Int. Ed.* **2007,** *46* (8), 1222-1244.

40 Y. Guan, Z. Wang, P. Gu, Y. Wang, W. Zhang, G. Zhang, In situ SERS Study of Plasmonic Nanochemistry Based on Bifunctional “Hedgehog-like” Arrays. *Nanoscale* **2019**.

41 D. Yu, C. Wang, P. Guyot-Sionnest, n-Type Conducting CdSe Nanocrystal Solids. *Science* **2003,** *300* (5623), 1277.

42 G. Reiss, A. Huntten, Magnetic Nanoparticles. In *Handbook of Nanophysics: Nanoparticles and Quantum Dots*, K. D. Sattler, Ed. CRC Press: Boca Raton, 2010.

43 The Nobel Prize in Chemistry 1925, NobelPrize.org, Nobel Media AB 2019. https://www.nobelprize.org/prizes/chemistry/1925/summary/. Accessed 28.04.2019.

44 C. Kinnear, T. L. Moore, L. Rodriguez-Lorenzo, B. Rothen-Rutishauser, A. Petri-Fink, Form Follows Function: Nanoparticle Shape and Its Implications for Nanomedicine. *Chemical Reviews* **2017,** *117* (17), 11476-11521.

45 P. K. Kundu, S. Das, J. Ahrens, R. Klajn, Controlling the lifetimes of dynamic nanoparticle aggregates by spiropyran functionalization. *Nanoscale* **2016,** *8* (46), 19280-19286.

46 A. Angı, R. Sinelnikov, H. H. Heenen, A. Meldrum, J. G. C. Veinot, C. Scheurer, K. Reuter, O. Ashkenazy, D. Azulay, I. Balberg, O. Millo, B. Rieger, The influence of conjugated alkynyl(aryl) surface groups on the optical properties of silicon nanocrystals: photoluminescence through in-gap states. *Nanotechnology* **2018,** *29* (35), 355705.

47 A. Angı, R. Sinelnikov, A. Meldrum, J. G. C. Veinot, I. Balberg, D. Azulay, O. Millo, B. Rieger, Photoluminescence through in-gap states in phenylacetylene functionalized silicon nanocrystals. *Nanoscale* **2016,** *8* (15), 7849-7853.

48 B. G. P. van Ravensteijn, W. E. Hendriksen, R. Eelkema, J. H. van Esch, W. K. Kegel, Fuel-Mediated Transient Clustering of Colloidal Building Blocks. *J. Am. Chem. Soc.* **2017,** *139* (29), 9763-9766.

49 R. Klajn, P. J. Wesson, K. J. Bishop, B. A. Grzybowski, Writing self-erasing images using metastable nanoparticle "inks". *Angew Chem Int Ed Engl* **2009,** *48* (38), 7035-9.

50 L. Heinen, A. Walther, Temporal control of i-motif switch lifetimes for autonomous operation of transient DNA nanostructures. *Chemical Science* **2017,** *8* (5), 4100-4107.

51 R. K. Grötsch, A. Angi, Y. G. Mideksa, C. Wanzke, M. Tena-Solsona, M. J. Feige, B. Rieger, J. Boekhoven, Dissipative Self-Assembly of Photoluminescent Silicon Nanocrystals. *Angew. Chem. Int. Ed.* **2018,** *57* (44), 14608-14612.

52 A. Arrigo, R. Mazzaro, F. Romano, G. Bergamini, P. Ceroni, Photoinduced Electron-Transfer Quenching of Luminescent Silicon Nanocrystals as a Way To Estimate the Position of the Conduction and Valence Bands by Marcus Theory. *Chemistry of Materials* **2016,** *28* (18), 6664-6671.

53 S. Li, I. N. Germanenko, M. S. El-Shall, Semiconductor Nanoparticles in Contact: Quenching of the Photoluminescence from Silicon Nanocrystals by WO3 Nanoparticles Suspended in Solution. *The Journal of Physical Chemistry B* **1998,** *102* (38), 7319-7322.

54 C. M. Gonzalez, M. Iqbal, M. Dasog, D. G. Piercey, R. Lockwood, T. M. Klapötke, J. G. C. Veinot, Detection of high-energy compounds using photoluminescent silicon nanocrystal paper based sensors. *Nanoscale* **2014,** *6* (5), 2608-2612.

55 H. M. Bank, E. M. Cifuentes, E. M. Theresa, Process for the synthesis of soluble, condensed hydridosilicon resins containing low levels of silanol. U. S. Pat, 5.010.159, 1991.

56 S. L. Anderson, E. J. Luber, B. C. Olsen, J. M. Buriak, Substance over Subjectivity: Moving beyond the Histogram. *Chemistry of Materials* **2016,** *28* (17), 5973-5975.

57 C. J. Murphy, J. M. Buriak, Best Practices for the Reporting of Colloidal Inorganic Nanomaterials. *Chemistry of Materials* **2015,** *27* (14), 4911-4913.